ABSTRACT

Title of Thesis: A GENERALIZED MODEL FOR WALL FLAME HEAT FLUX DURING UPWARD FLAME SPREAD ON POLYMERS

Kevin T. Korver, Master of Science, 2015

Thesis Directed By: Professor Stanislav Stoliarov
Department of Fire Protection Engineering

A current model accurately predicts flame to surface heat flux during upward flame spread on PMMA based on a single input parameter, the mass loss rate. In this study, the model was generalized to predict the heat flux for a broad range of polymers by adding the heat of combustion as a second input parameter. Experimental measurements were conducted to determine mass loss rate during upward flame spread and heat of combustion for seven different polymers. Four types of heat of combustion values were compared to determine which generated the most accurate model predictions. The complete heat of combustion yielded the most accurate predictions (± 4 kW/m^2 on average) in the generalized model when compared to experimental heat flux measurements collected in this study. Flame heat flux predictions from FDS direct numerical simulations were also compared to the generalized model predictions in an exploratory manner and found to be similar.

A GENERALIZED MODEL FOR WALL FLAME HEAT FLUX DURING UPWARD FLAME SPREAD ON POLYMERS

By

Kevin T. Korver

Thesis submitted to the Faculty of the Graduate School of the
University of Maryland, College Park in partial fulfillment
of the requirements for the degree of
Master of Science
2015

Advisory Committee:

Professor Stanislav Stoliarov, Ph.D., Chair
Professor Arnaud Trouvé, Ph.D.
Professor Michael Gollner, Ph.D.

ACKNOWLEDGEMENTS

First and foremost I would like to thank Dr. Rich Lyon and the FAA for funding this research. Without this support I would not have been provided such an amazing opportunity to conduct this research and earn my degree with the University of Maryland. A sincere thank you. Dr. Stas, thank you for seeing something in a west coast chemical engineer and allowing me the opportunity to conduct this research. Thank you for dispensing your tremendous amount of wisdom and knowledge and for repeating yourself so I could attempt to absorb as much as possible. I have learned so much from you.

Isaac, without your insight, guidance, and brilliance, completing this research project would not have been possible. You have gone out of your way to share your knowledge and experience with me and I truly appreciate it. I know you will go far and when you make it out west you'll have to pay us a visit. Mark, Xuan, Yan, and Geri, thank you for making the trip in from D.C. worth it every day. For all the times I have bounced ideas off you or just needed a mental break, you were there for me. I will look back on my days spent at the cubicle in the dragon corner with fondness. Olga, you were an invaluable asset in the lab. Thank you for being patient with all my questions and helping me master the fine art of running cone calorimeter tests. I am also grateful to Chris, Randy, Dr. Trouvé, and Simon for their help with the FDS simulations.

Lastly, to my amazing wife, who has supported and encouraged me from day one, I am so thankful for you. There really are no words to describe how much your support has meant to me. It might sound cliché but it has never been truer, I could not have done this without you.

TABLE OF CONTENTS

LIST OF TABLES.

LIST OF FIGURES.

1. INTRODUCTION

1.1. UPWARD FLAME SPREAD

1.1.1. Hazards/Significance

Upward flame spread is largely regarded as the most hazardous mode of flame spread because of the speed with which it can grow [1] and because it is often present during the initial stages of fire growth [2]. The rapid spread of flame along a combustible vertical surface is due to buoyancy-induced flow, the natural tendency of the flame and hot plume to flow upwards in close proximity to the vertical surface [3]. The flame and hot plume transfer heat to the combustible surface downstream of the burning region causing more combustible vapors to be produced at the surface and ignited by the flame. This continuous heat feedback loop can result in an exponential growth of the burning region and flame length such that, if left uninhibited, the flame and thus the amount of heat produced will grow rapidly. This process can be extremely hazardous in any compartment that contains other combustible materials that would contribute to the growth of the fire.

The importance of upward flame spread, also referred to as concurrent or gravity-opposed flame spread, is underscored by the significant amount of theoretical and experimental research performed to better understand its behavior. Additionally, its importance is highlighted by the quantity of standard tests and regulations aimed at characterizing the flammability requirements for materials ranging in use from everyday household items to aircraft cabin paneling and other wall lining materials [4] [5] [6]. Understanding the physical processes that control the rate of upward flame spread over a

material is vital to developing new materials, test methods, and regulations that minimize this hazard.

2. BACKGROUND

2.1. BRIEF HISTORY

The problem of upward flame spread has garnered significant attention from researchers, engineers, and regulatory agencies. For over 40 years, researchers and scientists have worked to develop theoretical and numerical models that describe and predict upward flame spread behavior on different materials [1] [3] [7]. Numerous experimental studies have also been performed to better understand the physical phenomena that control upward flame spread.

The works by Emmons [8] and de Ris [7] provide some of the first in-depth analyses of the general flame spread process, valid for any orientation. In it they describe how the flame transfers heat to the unburned fuel which in turn produces gaseous fuel (pyrolyzes) once it reaches a certain temperature. This newly produced gaseous fuel then reacts with air to produce more heat, a portion of which gets transferred back into the surface to complete the "heat feedback" cycle that advances the flame spread process [7] [8]. From this analysis, de Ris also developed two theoretical flame spread formulas; one for thermally thin fuels and one for thermally thick fuels [7].

Later, Kim et al. developed a theoretical model to predict the laminar burning rates of fuels in different orientations [9]. Orloff et al., Fernandez-Pello, and Ahmad and Faeth developed theoretical models for upward flame spread [10] [11] [12].

These works have formed the foundation for several further attempts at modeling upward flame spread. Early on, it was recognized that the heat transfer from the flame to the surface [3] and the length of the region heated by the flame [13] are the controlling mechanisms in upward flame spread. A simplified model for the rate of flame spread, v_p, over a thermally thick fuel is shown in Equation (1) [14].

$$v_p \approx \frac{4\left(q_f''\right)^2 \delta_f}{\pi(k\rho c)\left(T_{ig} - T_s\right)^2} \tag{1}$$

In the numerator, q_f'' is the net flame to surface heat flux and δ_f is the length of the unburnt region above the pyrolysis front that gets preheated by the flame. In the denominator k, ρ, and c are the thermal conductivity, density, and heat capacity of the fuel, respectively, and T_{ig} and T_s are the ignition and initial surface temperatures of the fuel, respectively. This equation emphasizes the importance of understanding the two parameters deemed critical by early researchers [13], the length of the preheating region and the net flame to surface heat flux. A basic diagram of the physics of upward flame spread is given in Figure 1 where y_f represents the flame height, q_f the flame heat flux, δ_f the preheat region, x_p the pyrolysis region, and m_F'' the mass flux of fuel in the pyrolysis region.

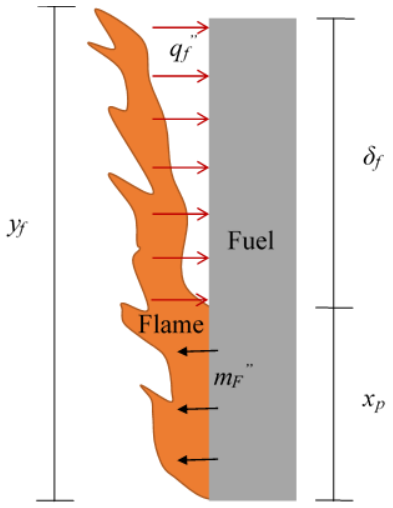

Figure 1. Basic diagram of the physics of upward flame spread.

The treatment of the flame heat flux over the preheating region varies between studies. The preheating region can be divided into two zones: the region directly under the flame, $y/y_f < 1$, where y is the height along the surface, and the region further downstream into the thermal plume, $y/y_f > 1$. In the region under the flame, flame heat flux is frequently reported as steady but then some studies use a value of 0 for $y/y_f > 1$ [14] while others use an exponentially decaying heat flux above y_f [15] [16]. Numerous experimental studies have been performed on the flame heat flux to a vertical wall during upward flame spread. The research done in these studies focused on quantifying q_f'' for both the region under the flame and the plume region beyond the flame for several different materials over a range of fuel widths and heights. The measurement techniques include the use of water-cooled gauges, fine thermocouples placed within the thermal boundary layer flow [17], and holographic interferometry [18]. Lattimer reviewed the results of several experiments measuring flame heat flux to the wall during upward flame spread and reported steady state heat flux values between 20 and 30 kW/m^2 with an exponential decay in the region above the flame on the order of $\left(y/y_f\right)^{-2.5}$ [19]. The

other important parameter to define for the models is flame length, y_f. This is generally accepted to be a function of the material mass loss rate or heat release rate. Delichatsios and Saito give the dependence of the flame length on the width-normalized heat release rate for turbulent wall fires as $y_f \propto \dot{Q}'^{2/3}$ [20].

The foundation of this study involves using a model for flame heat feedback that has already been developed using PMMA and extending it to other materials using standard material properties. Similar attempts at predicting upward flame spread for various materials have also been attempted in previous works. Delichatsios and Saito developed an upward flame spread and growth model for turbulent wall fires that uses "key flammability properties" of charring and non-charring materials as inputs [20]. Their model uses the heat of combustion (ΔH_c) and combustion efficiency (χ_e) to determine flame height and the distribution of the flame heat flux to the wall. Additionally, the radiative fraction (χ_r), flame temperature T_{fl}, and stoichiometric fuel to air ratio, r, are used to calculate the magnitude of the convective and radiative heat fluxes to the wall. Quintiere and Cleary developed a model for predicting upward flame spread on wall linings that can use material properties measured directly from the cone calorimeter and Lateral Ignition and Flame Spread Test (LIFT) apparatus [21]. Beyler et al. have also designed a computer model that predicts upward flame spread using the material's heat of combustion and heat of gasification in flame length calculations and an experimentally determined flame heat flux profile for flame to wall heat transfer calculations. [22]. Brehob et al. have more recently developed a one-dimensional upward flame spread numerical model for use on practical wall materials [15]. The model utilizes measured material mass loss rate, heat of combustion, and measured peak flame heat flux

along with material thermophysical properties to predict upward flame spread with some success.

2.2. PMMA MODEL

The upward flame spread models reviewed up until now have focused primarily on larger fires with test samples ranging from 0.2 m to >1 m in height. In this scale, flames are no longer laminar and the heat transfer to the unburned fuel surface becomes dominated by radiation as the fire size increases. While these models work well in this regime, they are limited in their ability to predict the flame to surface heat flux for smaller-scale flames (< 20 cm). Since upward flame spread is often the dominant mode of heat transfer to adjacent, unburned fuel in the early stages of a fire, when the flames are small, it would be useful to have a model that can predict flame spread in smaller configurations. To address this deficiency, an analytical model that accurately predicts flame to surface heat feedback for small-scale, upward flame spread based solely on mass loss rate has been developed by Leventon and Stoliarov from finely resolved heat flux and mass loss measurements for PMMA [23]. To further enhance this model, additional, flame heat flux and mass loss measurements have been collected at 9 heights from 3 cm < y < 20 cm for 5 cm wide thermally thick PMMA samples. This enhancement provided more accurate predictions of flame to surface heat flux shortly after ignition and included adjustments for dripping behavior. 5 cm wide samples were chosen because, as reported by Pizzo et al. [2], this is the minimum width where the width-normalized burning rate, measured as $\dot{Q}'$ in their study, remains the same as wider samples. It should also be clarified that heat flux measurements performed for this model were done using a water-

cooled heat flux gauge. There is significant variation in heat flux values reported in literature and it is not always clear which values are being presented. Thus, unless otherwise noted, any reference to flame heat flux when discussing this model should be taken as the heat flux to a water-cooled gauge and will be written as q''_{HFg}. This is equivalent to the incident heat flux to the surface, which does not consider reradiative or convective losses from the surface, rather than the net heat flux, which takes surface temperature and heat fluxes from the surface into account.

In Leventon et al's model, flame height, y_f, was carefully related to the width-normalized mass loss rate, $\frac{dm'}{dt}$. Here, y_f is defined by a quantitative threshold value of the steady state heat flux to the surface rather than a qualitative measurement based on visual observations of the flame. Consalvi et al. emphasized the importance of using a quantifiable criterion when defining y_f for use in numerical and theoretical models [24]. The steady-state heat flux, q''_{steady}, was measured to be highest near the base of the flame, decreasing to an asymptotic value further downstream. This result is in agreement with the findings of Brehob et al., who measured an approximately constant steady-state heat flux for sample heights up to y = 1.2 m [15]. The measured value of q''_{steady} is given by the following piece-wise function [23]:

$$q''_{steady} = \begin{cases} 40 \quad \text{kW/m}^2 & ; y \leq 5 \text{ cm} \\ 34 \quad \text{kW/m}^2 & ; y > 5 \text{ cm} \end{cases} \tag{2}$$

Using the definition of y_f as a threshold value of q''_{steady} and mass loss rate measurements, a relationship between y_f and $\frac{dm'}{dt}$ was determined to be accurately described by a single power law function with the following form:

$$y_f = a\left(\frac{dm'}{dt}\right)^b + c \tag{3}$$

where a = 189.2, b = 0.4592, and c = -6.905 and the units of y_f and $\frac{dm'}{dt}$ are cm and g/(cm-s), respectively. The form of this expression is similar to the previous model [23] but the empirical constants a, b, and c are adjusted to account for material dripping at the base of the sample. Accounting for this provides a more accurate prediction of y_f for materials that exhibit a flame base that does not remain fixed to the bottom of the sample as will be described in more detail in section 5.3.

By plotting the normalized heat flux measurements, $q^* = \frac{q''_{HFg}}{q''_{steady}}$, against a normalized length scale, y^*, a unified heat flux profile becomes readily apparent. The previous model [23] has recently been refined using new q''_{HFg} measurements and a slightly different length scale as expressed in Equation (4).

$$y^* = \frac{y + y_0 - y_b}{y_f + y_0} \tag{4}$$

where y is the height with respect to the base of the sample where q''_{HFg} was measured, y_0 = 3.75 is an empirical constant, and y_b represents the location of the base of the flame with respect to its starting location at y_b = 0. Using this normalized length scale along with measurements of q''_{steady}, the flame heat feedback to the surface can be expressed as

$$q''_{HFg} = \begin{cases} q''_{steady} & ; y \le y_f \\ \left(\alpha \times q''_{steady}\right)\left(e^{-\ln(\alpha)\times(y^*)^2}\right) & ; y > y_f \end{cases} \tag{5}$$

where α = 1.794 is an empirically derived constant. This is similar to the model presented previously [23] except the heat flux profile in the region above the flame has a slightly different shape to more closely match the measured profile. This improved model

provides highly accurate predictions of small-scale flame to surface heat feedback both under the flame and in the region above the flame for PMMA, as shown in Figure 2. More details about this model and its coupling with a condensed phase pyrolysis model will be presented in a soon to be published paper.

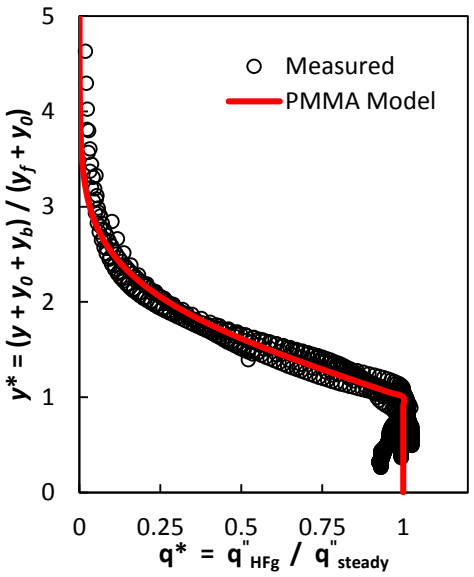

Figure 2. PMMA flame heat feedback model compared to measurements.

3. PURPOSE OF THIS WORK

The model described in the previous section is capable of predicting flame to surface heat flux during small-scale upward flame spread on PMMA with great accuracy. However, the significant shortcoming to this model is that it is material specific. This study aims to substantially improve the model by generalizing it so that it can be used for a broad range of polymers. This improved model, referred to in this study as the generalized flame heat flux model, uses material properties and burning behavior that can

be easily measured or referenced in literature as input parameters to scale the PMMA model.

An in depth study of four potential input parameters is performed in this study to determine which parameter provides the most accurate prediction of flame heat flux when used to scale the PMMA model to a different material. The four input parameters studied in this work are four different types of heat of combustion. A material's heat of combustion is a fundamental property for fire safety and is often used as a point of reference when comparing the relative hazard of a material. As a result of its importance in the fire research industry, multiple methods exist for obtaining heats of combustion and it is commonly tabulated for many materials. Thus, it would be ideal to utilize this property when generalizing the existing PMMA model to new materials.

To analyze the accuracy of the generalized flame heat flux model, several experiments were performed to gather the values necessary for analysis. First, mass loss rate measurements during small-scale upward flame spread tests, similar to those done to develop the PMMA model, were performed for seven different polymers. Next, heat of combustion measurements were performed in a cone calorimeter in different orientations to determine which heat of combustion value generates the most accurate predictions in the generalized model. Lastly, flame heat flux measurements were obtained for all seven materials at heights ranging from 5 cm to 15 cm so that predicted values of flame heat flux from the generalized model could be compared to experimental values.

Additionally, two-dimensional (2D) direct numerical simulations (DNS) of the experimental setup used to develop the PMMA model have been performed in Fire Dynamics Simulator (FDS), a computational fluid dynamics (CFD) solver developed by

the National Institute of Standards and Technology (NIST) specifically for low-speed, fire-driven fluid flow [25]. An analysis of flame to surface heat flux measurements has been done using FDS and is compared to predictions from the generalized flame heat flux model. This analysis is exploratory in nature and sets the initial framework for future, more thorough analysis.

4. EXPERIMENTAL DESIGN AND PROCEDURE

4.1. MATERIAL SELECTION

Materials selected in this study are widely used in industry and present a broad range of chemical and physical structures and diverse burning behavior. The materials chosen for this study were cast PMMA, polypropylene (PP), polyoxymethylene (POM), acrylonitrile butadiene styrene (ABS), high impact polystyrene (HIPS), fiberglass reinforced polyester resin (FRP), and glass filled polybutylene terephthalate (PBT). FRP and PBT are unique in this study in that they are both composite materials. The FRP was assembled in-house, using approximately 50% woven fiberglass and 50% unsaturated polyester thermosetting resin. PBT samples were supplied by BASF and have a 25% concentration of chopped glass fibers by weight.

4.2. EXPERIMENTAL SETUP

4.2.1. Sample Preparation

All samples come in 6.0 mm +/- 0.5 mm thick sheets which are then cut to the appropriate width and length (+/- 1 mm). Once cut to the desired dimensions, samples are mounted in 6 mm thick, rigid ceramic fiber board insulation (Kaowool PM) such that

only the front surface of the sample is exposed. Thermal and physical properties of Kaowool PM are available online through the manufacturer's website and have been validated in a previous study [26]. The Kaowool PM strips that surround all four sides of the test sample are 2.5 cm wide. The test sample and Kaowool PM pieces are secured together using a thin, < 0.3 mm, layer of 3M Locktite high temperature epoxy such that the front surface of the test sample and insulation are flush and no gaps exist between the insulation and test sample. Once set in place, the prepared test sample is secured firmly in a clamp for at least one hour to allow the epoxy to cure. The final step is to place the sample in a desiccator for a minimum of 24 hours.

4.2.2. Sample Holder

In order to obtain reproducible measurements, a previously designed sample holder apparatus was utilized for these experiments [27]. The design of this apparatus was chosen for durability, to create a controlled flow field around the sample, and to allow for both heat flux and mass loss measurements to be easily performed.

Once ready for testing, prepared test samples are placed within a custom-made steel holder. Proper alignment of the test sample within the holder involves exposing 0.5 cm of insulation on either side of the sample, 2 cm below the sample, and at least 0.5 cm above the sample. The steel holder is designed so that the test sample is pressed up against the front of the holder. With the steel only 1.4 mm thick, the holder creates a nearly uniform vertical surface of at least 3.5 cm in every direction from the sample. This promotes a laminar flow field around the test sample's front surface. Figure 3 depicts the steel sample holder.

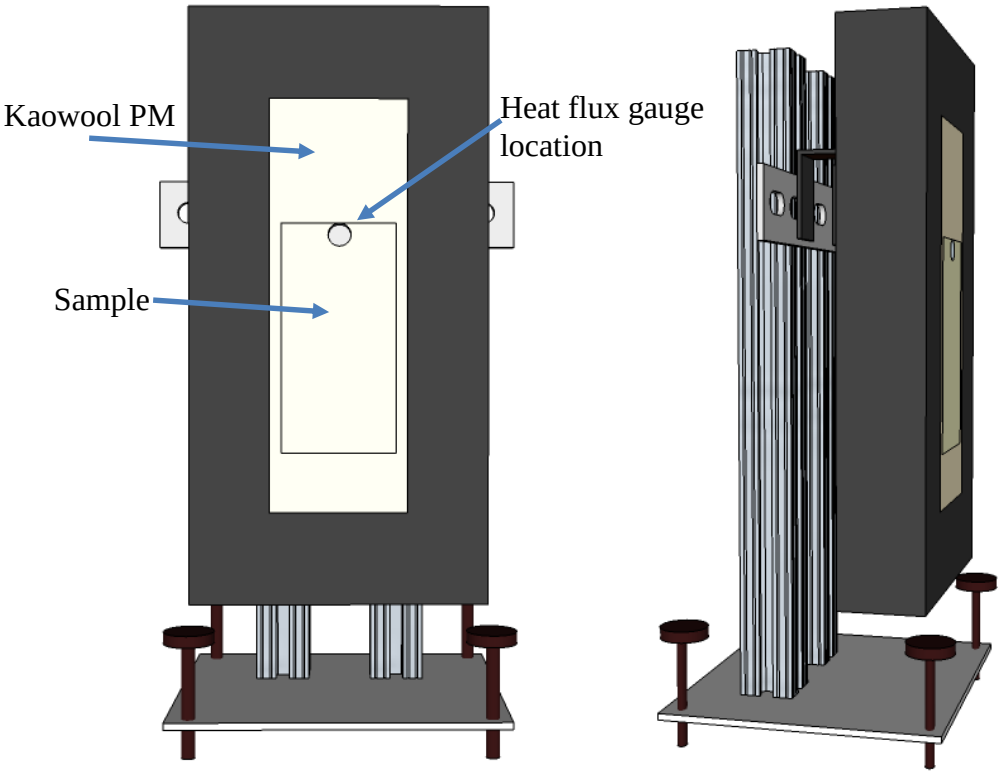

Figure 3. Front and side views of sample holder apparatus. For reference, sample within holder is 10.5 cm tall.

The entire sample holder is placed on a mass balance in order to obtain mass loss measurements. The mass balance sits within heavy duty fire retardant blankets to minimize interferences from cross-flow or air movement within the laboratory. Approximately 20 cm above the top of the sample holder, an exhaust hood continuously extracts combustion products at a rate of 100 cfm. This is enough to capture the byproducts from burning even the largest samples while still maintaining a quiescent (<~3-5 cm/s vertical flow) environment around the test sample.

4.2.3. Sample Igniter

The apparatus used to ignite the lower 2 cm to initiate flame spread tests is depicted in Figure 4. It was important to have a consistent preheating and ignition source

for each test. The sample igniter developed for this study uses a small propane diffusion flame and a steel shield to create a reproducible heat flux profile to the lower 2.5 cm of the sample.

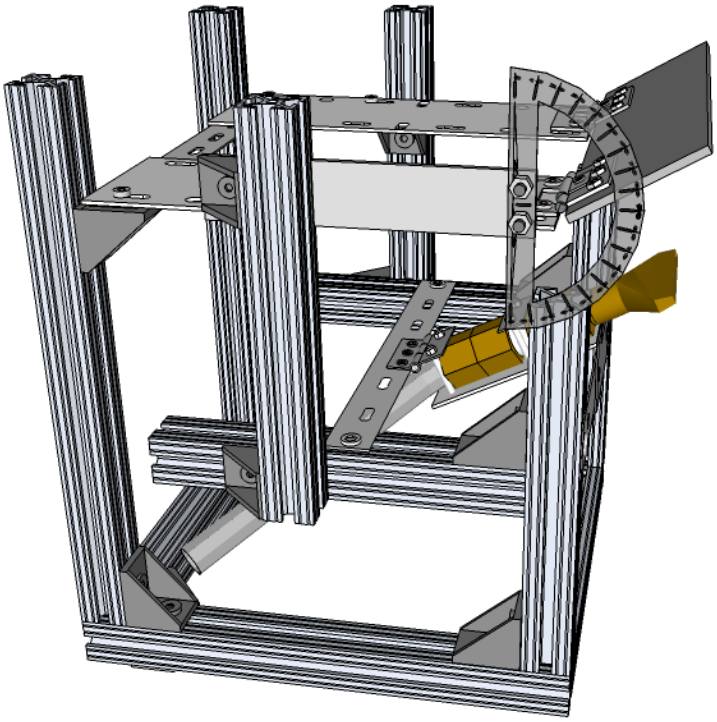

Figure 4. Detailed depiction of the sample igniter.

The propane is fed at 0.1502 +/- 0.1% L/min through a 0.2 cm opening in a 5 cm wide brass nozzle that is positioned at a 45° from the sample surface, 1.8 cm below the bottom of the sample, and < 1 mm from the surface of the Kaowool PM. A single-stage regulator is used to maintain a constant flow rate and a Bios Defender 530 volumetric flow meter is used to measure the flow rate. The 0.3 cm thick steel shield is kept at an 18° angle above horizontal and the front end of the shield is 2.25 cm above the bottom of the sample. A thin, 6 cm wide strip of aluminum is wrapped around the center of the shield to

block the gap between the shield and the sample created by the 1.4 mm thick steel sample holder and to help align the propane nozzle.

The small (< 4 cm) size of the sample igniter flame, its proximity to the surface of the sample, and its laminar flow result in a primarily convective heat flux being applied to the bottom of the test sample. The igniter is applied to the bottom of the sample just long enough for a small, 1 – 2 cm tall, self-sustaining flame to be present across the entire width of the sample after the igniter is removed. Depending on the material being ignited, this ignition time ranges from 110 – 205 seconds for the materials tested in this work. Figure 5 shows the heat flux profile created by the sample igniter.

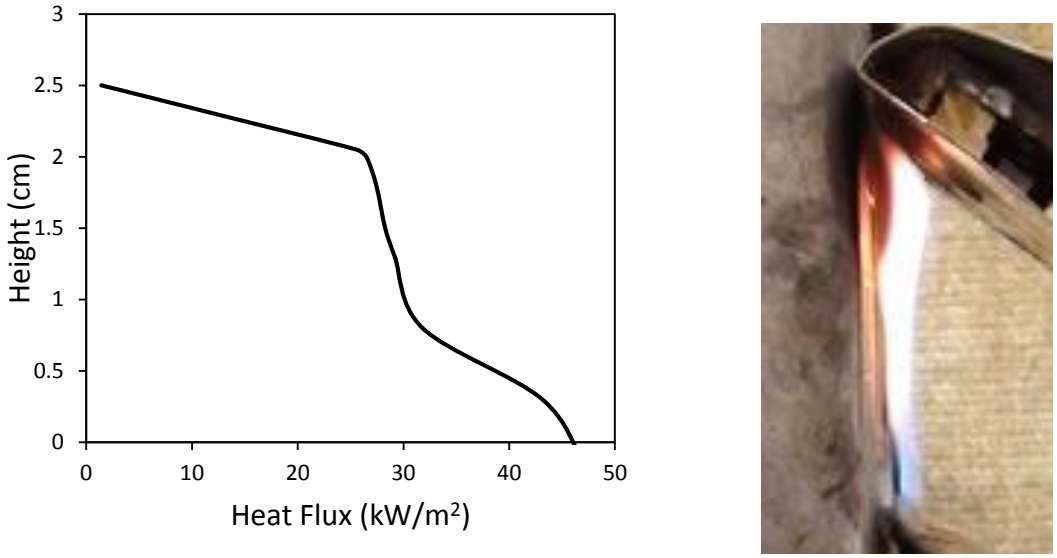

Figure 5. Heat flux profile from sample igniter to lower 2.5 cm of sample.

4.3. EXPERIMENTAL PROCEDURES

4.3.1. Mass Loss Tests

Mass loss measurements are obtained using a Mettler Toledo XS4002S mass balance at a rate of 1 Hz and a readability of 0.01 g. The values are transmitted to a

laptop through a USB cable and saved to a text file for processing. The measured mass loss then converted to a width-normalized mass loss rate using Equation (6).

$$\frac{dm'}{dt} = \frac{1}{w}\frac{m_{t_1} - m_{t_2}}{t_2 - t_1} \tag{6}$$

where w is the width of the sample, in cm, and m_{t_i} is the measured mass, in grams, at t_i

During each test, a camera records video of the test and written notes on burning behavior and flame spread are taken for reference. Time t = 0 s for the measurements is taken as the time when the sample igniter is removed. The timing of when to end the test is material specific. Generally, the test is ended whenever non-ideal burning behavior occurs, such as heavy build-up of surface deposits, melt flow, or if the sample has been completely consumed at the base such that the epoxy begins to contribute to the flame. At this point recording is stopped and the flame is extinguished.

Due to the significant build-up of surface deposits during upward flame spread on ABS, flame spread was limited unless an external heat flux of q_e'' = 10 kW/m^2 was applied throughout the tests using a radiant heating panel. The heater would be moved into position, approximately 16.5 cm in front of the sample, within 10 seconds after the removal of the sample igniter. The time at which the heater was in position was used as the start time, t = 0 s, for ABS mass loss measurements.

4.3.2. Heat of Combustion Tests

Heats of combustion were measured in a Govmark CC1 cone calorimeter. In addition to the seven materials studied thoroughly for this report, high-density polyethylene (HDPE) was also tested in the cone calorimeter as further testing may be done on this material in the future. The cone calorimeter can be used to calculate heat

release rate of a burning sample by measuring oxygen consumption and applying the generalization that most combustible materials produce approximately 13.1 kJ of energy per gram of oxygen consumed [28]. Burning a flow of methane that will produce a known heat release rate, typically 5 kW, allows a constant to be obtained, known as the C-factor, which accounts for the specific arrangement of the exhaust duct and gas sampling system. Combining the heat release rate measurements with a built-in Sartorius mass balance, heats of combustion can be calculated. For further details on the theory and operation of the cone calorimeter, see ASTM E1354 *Standard Test Method for Heat and Visible Smoke Release Rates for Materials and Products Using an Oxygen Consumption Calorimeter* or one of several sources in the literature [29] [30]. In addition to oxygen consumption and mass loss measurements, carbon monoxide (CO) and carbon dioxide (CO_2) concentrations, in percent by volume, were also measured for analysis of burning efficiency.

Each material was tested in at least two different configurations, with some materials tested in as many as four different configurations, and each material was tested at least three times in each configuration, with a few exceptions. The configurations, depicted in Figure 6, included a) a horizontal orientation with q_e'' ($\Delta H_{eff,H}$), b) a horizontal orientation without q_e'' (ΔH_0), c) a vertical orientation with q_e'' ($\Delta H_{eff,V}$), and d) a vertical orientation without q_e'' (ΔH_{vert}). The heats of combustion for the horizontal and vertical orientations with q_e'' are referred to as the effective heat of combustion in this paper to be consistent with the nomenclature used in other sources[1]. These configurations, $\Delta H_{eff,H}$ and $\Delta H_{eff,V}$, are typically used as the standard configuration when reporting effective heat of combustion values for a material [31]. The peak heat release

[1] This value is also referred to as the chemical heat of combustion (ΔH_{ch}) in some sources.

rate from tests done in the horizontal orientation without q_e'' has been referred to as the intrinsic heat release rate [32], HRR_0, hence the heat of combustion value measured in the same configuration is labeled here as ΔH_0.

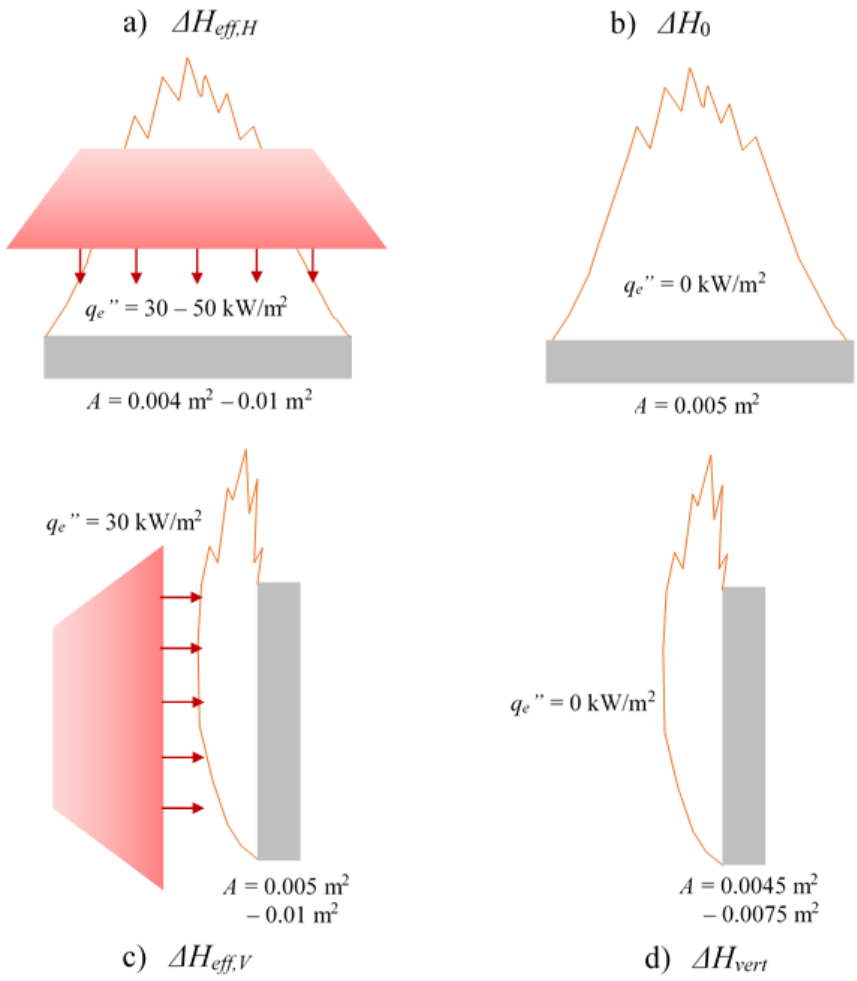

Figure 6. The four different configurations tested in the cone calorimeter for heat of combustion measurements: a) horizontal with q_e'', $\Delta H_{eff,H}$, b) horizontal without q_e'', ΔH_0, c) vertical with q_e'', $\Delta H_{eff,V}$, and d) vertical without q_e'', ΔH_{vert}.

Figure 6 also includes the level of external heat flux applied and sample sizes tested in each configuration. The motivation behind measuring heats of combustion in several different configurations stemmed from wanting to determine whether heat of combustion values measured in the same configuration as the mass loss and heat flux experiments (vertical with no external heat flux, ΔH_{vert}) showed any difference from

those measured in the standard configuration, $\Delta H_{eff,H}$. When initial measurements in the two configurations showed a noticeable difference, further testing in different configurations was performed to explore potential sources for this difference. The results from these tests and subsequent speculations regarding this difference are summarized in Section 5.4. Table 1 below gives the number of tests performed for each material in the four test configurations.

Table 1. Number of tests performed in each configuration for each material.

Material	Horizontal		Vertical	
	$\Delta H_{eff,H}$	ΔH_0	$\Delta H_{eff,V}$	ΔH_{vert}
POM	4	---	3	4
FRP	3	---	4	1
PBT	3	---	2	---
Extruded PMMA	3	---	3	4
Cast PMMA	3	2	3	3
ABS	5	---	2	6
HIPS	4	---	3	3
PP	3	2	4	4
HDPE	4	2	1	4
TOTAL	**32**	**6**	**25**	**29**

At the beginning of each day of testing, the oxygen, carbon monoxide (CO), and carbon dioxide (CO_2) analyzers and mass balance were calibrated, drierite and ascarite replaced, sample ring, stack thermocouple and pressure ports cleaned, and a C-factor calibration performed. Prior to performing any tests, a calibration check using a standard, 10 × 10 × 1.2 cm black cast PMMA sample in the horizontal orientation under the cone heater was completed to ensure the accuracy of the measurements. This test was also performed at the end of each day of testing to check for any drift in measurements. For results of the daily $\Delta H_{eff,H}$ measurements for black cast PMMA calibration tests, see the

Appendix. Great care was taken to perform any cleaning or calibrations necessary in between tests in order to maintain consistent results..

Samples for $\Delta H_{eff,H}$ tests were first cut to the desired size and then conditioned in a desiccator for a minimum of 12 hours. The majority of horizontal tests were performed on 10 × 5 cm samples but a few tests were also done on 10 × 10 cm samples and 5 cm wide samples between 7.5 cm and 9.5 cm long. Once conditioned in the desiccator, samples were weighed, wrapped in a 0.05 mm layer of aluminum foil around the bottom and sides, weighed again, and placed on top of four 6 mm thick Kaowool PM sheets that rest in a steel sample holder. For materials that were likely to swell and flow over the aluminum foil, a secondary containment of aluminum foil at least 0.5 – 1 cm wider than the sample was placed under the sample so any overflow would not absorb into the insulation.

With the cone heater set to a specified temperature that produced the desired heat flux at the surface of the sample, an insulated shield was put into place to temporarily block the heater. Most tests were performed with an incident heat flux of 30 kW/m^2, measured with a Schmidt-Boelter water-cooled heat flux gauge, but some tests were also done at 40 and 50 kW/m^2 of incident heat flux. The sample holder was then positioned under the cone heater such that the surface of the sample was 2.5 cm below the base of the cone heater. At the moment the heater shield was removed, measurement recordings were initiated and the spark igniter was positioned over the center of the sample to begin the test. Time of ignition and extinction were noted and measurements were recorded for at least two minutes after extinction. The aluminum foil and any remaining residue were then weighed as a reference for total mass loss measurements.

ΔH_0 tests were only performed for three materials as part of the investigation into differences between $\Delta H_{eff,H}$ and ΔH_{vert} results. Each sample was 10 × 5 cm and prepared in the same way as tests with an external heat flux. The cone heater was removed from its normal position so it would not heat up during the test and provide an unwanted additional heat flux to the sample. Measurement recording was initiated prior to placing the sample within the exhaust hood. At this time, the sample was heated and ignited using a premixed propane torch outside of the exhaust hood. Depending on the material, this process took approximately 45-90 seconds. Once a steady and uniform flame remained present on the sample without the torch, the sample was placed under the exhaust hood and this time was noted as the ignition time. Samples were allowed to burn to completion, measurements were recorded for at least two minutes after extinction, and the bfinal mass of aluminum foil and any residue was recorded.

$\Delta H_{eff,V}$ tests were conducted for 10 × 5 cm and 10 × 10 cm samples. Both sample sizes were surrounded by and affixed to Kaowool PM insulation sheets in the same manner as mass loss tests. The 10 × 5 cm samples could be placed within the steel sample holder but the 10 × 10 cm samples were too wide to fit in the holder. Instead, a simple apparatus was fabricated from 80/20 aluminum T-framing and two small clamps to hold the sample upright in front of the cone heater. With the cone heater arranged in the vertical orientation the 10 × 5 cm sample was placed in the sample holder apparatus and positioned in front of the heater such that the front surface received 30 kW/m^2 of incident heat flux. This marked the start of the test. A spark igniter was positioned over the center of the sample within 0.5 cm of the sample surface in order to ignite the volatiles being produced within the narrow boundary layer in front of the sample. Once a sustained

flame was present on the surface, this time was recorded as the ignition time and the spark igniter was removed. During the test, burning behavior was monitored closely to determine the time at which behavior was no longer ideal and the test would be stopped at this point. Non-ideal behavior primarily consisted of significant dripping or collapse of the sample but for materials that did not drip significantly or collapse, the test was stopped before the sample burned through to the epoxy holding it in place.

Samples for ΔH_{vert} tests were 5 cm wide and 9 – 11 cm tall except PBT tests which used 15 cm tall samples. Samples were surrounded by and affixed to Kaowool PM insulation sheets similarly to mass loss tests and secured within the steel sample holder. With the sample holder resting on the mass balance and the sample igniter positioned in front of the sample as in the mass loss and heat flux tests, the propane was ignited to start the test. The sample igniter was removed after the required ignition time for each material. Flame spread observations were recorded as the test progressed until the burning behavior became non-ideal. At this point the test was stopped and the material extinguished.

There were slight differences in how the heat of combustion was calculated for each configuration. Due to the varying natures of ignition and measurements being stopped in the middle of burning for vertical tests rather than allowing to burn to completion like horizontal tests, a consistent method for calculating the heat combustion was utilized to permit meaningful comparison between configurations. For horizontal tests ($\Delta H_{eff,H}$ and ΔH_0), only measurements between the first 5% and last 20% of sample mass were used in calculations. Calculating the effective heat of combustion at each time

step using Equation (7) and plotting it against time gives a visualization of why measurements from the middle 75% of the horizontal tests were used.

$$\Delta H_{\text{eff},t_2} = \frac{Q_{t_1 \to t_2}}{m_{t_2} - m_{t_1}} \tag{7}$$

$Q_{t_1 \to t_2}$ is the total heat released between t_1 and t_2 and m_{t_i} is the measured mass at time t_i. Figure 7 plots a time history of the effective heat of combustion at each time step, $\Delta H_{\text{eff,t}}$, to show how quasi steady-state behavior (heat release and mass loss rates may still be increasing but they are both increasing at the same rate) occurs just after the initial 5% of mass is consumed to just before the final 20% of mass remains. 75% of sample mass after the first 5%, shown by the effective heat of combustion values between the two red lines, is used to calculate the effective heat of combustion. It is clear from the plot that only using measurements from the middle 75% of the test removes any influences from burning near ignition and extinction. By removing these influences, results from horizontal and vertical orientations can be compared in a more meaningful manner.

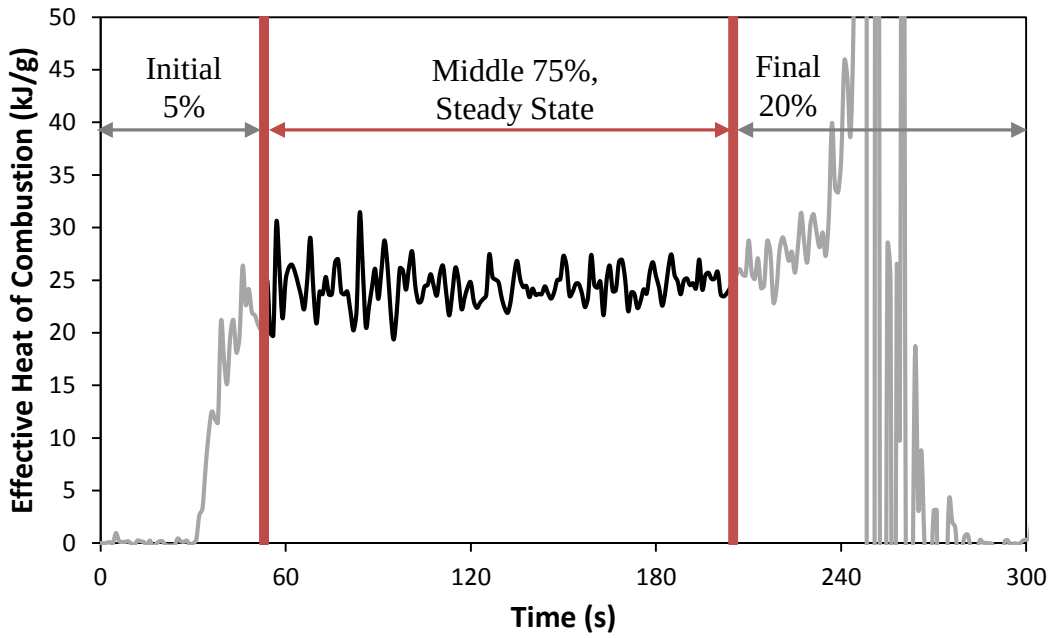

Figure 7. Effective heat of combustion vs time for a horizontal test of cast PMMA showing the portion of time where measurements are used to calculate overall effective heat of combustion.

A slightly different method was used to calculate the effective heats of combustion for vertical tests with external heat flux. The first 5% of sample mass is disregarded again, but the end of measurements is based on when material burning behavior becomes non-ideal, as described earlier in this section. In order to be conservative but still utilize as much data as possible, measurements up to 20 seconds before the time at which burning behavior became non-ideal were used for effective heat of combustion calculations.

For vertical tests with no external radiation, there was an additional complication that arose from the sample igniter. Instead of trying to subtract the heat released by the sample igniter from the total heat released, measurements were started 20 seconds after the sample igniter was removed to provide sufficient time for propane combustion products to pass through the measurement system. Similar to vertical tests with an

external heat flux, measurements used for heat of combustion calculations were stopped 20 seconds prior to the onset of non-ideal burning behavior or extinguishing of the sample.

$\Delta H_{eff,H}$ values were compared to the heat of complete combustion, ΔH_T, measured in a microscale combustion calorimeter (MCC) to obtain combustion efficiencies, χ_e, for each material. The MCC measures complete heat of combustion using small, ~2 – 5 mg, samples undergoing controlled thermal decomposition in anaerobic conditions. The pyrolysis gases released from the sample are then mixed with excess oxygen in a high temperature combustion furnace to force complete oxidation. The resulting flow rate and oxygen concentration in the exit stream and total mass loss are used to calculate what is referred to in ASTM D7309 *Standard Test Method for Determining Flammability Characteristics of Plastics and Other Solid Materials Using Microscale Combustion Calorimetry* as the "specific heat of combustion of specimen gases" ($h_{c,gas}$) [33]. For all materials except FRP and PBT, ΔH_T was obtained from the MCC with values reported by Lyon et al. [34]. The ΔH_T for PBT was obtained from a colleague's recent publication [35] and ΔH_T for FRP was calculated from tests performed by a colleague within our research group. The calculation of combustion efficiency is simply the ratio of the effective heat of combustion and the complete heat of combustion as shown in Equation (8).

$$\chi_e = \frac{\Delta H_{eff,H}}{\Delta H_T} \tag{8}$$

4.3.3. Heat Flux Tests

Heat flux measurements are obtained with the use of a 0.95 cm diameter, water-cooled Schmidt-Boelter heat flux gauge manufactured by Medtherm. On average, the water temperature in the gauge was measured to by 291 K. Measurements from the heat flux gauge are recorded in LabView through a NI USB-9211 Data Acquisition (DAQ) device at a rate of 2 Hz.

The face of the heat flux gauge is first coated with a thin layer of optical black coating, provided by Medtherm that has an average emissivity of 0.95. After allowing the paint to cure, the gauge is calibrated under the radiant cone heater in a cone calorimeter using a reference gauge. Placing the gauges side-by-side under the heater, the mV response of the freshly painted gauge to radiant heat fluxes of approximately 20, 35, and 50 kW/m^2 is compared to the heat flux measured by the reference gauge. These three points are plotted and a calibration constant is obtained for the gauge by finding the slope of the line of best fit assuming a response of 0 mV when no heat flux is present. A new calibration constant is obtained between each test and, unless no residue or combustion products deposit onto the face of the gauge, a new coating of paint is applied between each test.

Prior to placing the test sample in the steel holder, a 1 cm diameter hole, just large enough for the heat flux gauge, is drilled in the top of the sample such that the top of the gauge is even with the interface of the sample and insulation. See Figure 3 for heat flux gauge location within the sample. Samples used for heat flux tests are cut 0.5 cm longer so the center of the heat flux gauge lines up with measurement height. For example, if a heat flux test were to be performed at 10 cm, the sample would be cut to 10.5 cm. As

discussed by Leventon, using one heat flux gauge at the top of the sample is superior to using multiple gauges along the centerline of a sample because of interferences to both the thermal conditions within the condensed-phase and the boundary layer flow along the surface of the sample [27].

When the drilled sample is secured in the steel holder, the heat flux gauge is positioned in the prepared hole so the painted face of the gauge is flush with the surface of the sample. The gauge is supported from behind using clips attached to the steel holder in order to keep the gauge horizontal. With the heat flux gauge securely in place, the sample igniter is set into position, recordings started, and propane ignited to start the test. Video recordings and written notes are taken during the test and the end of the test is determined in the same manner as moss loss tests.

For two materials, HIPS and ABS, it was desired to measure heat flux at a specified time after ignition without the impact of surface deposits building up on the gauge's surface. In order to obtain these measurements, a strip of Kaowool PM insulation was placed on top of the gauge as shown in Figure 8 to shield the gauge from the surface deposits. The tests were initiated in the same manner as normal tests, then, at the desired time after ignition, the shield is removed and the gauge is exposed to the flame and/or thermal plume to collect measurements.

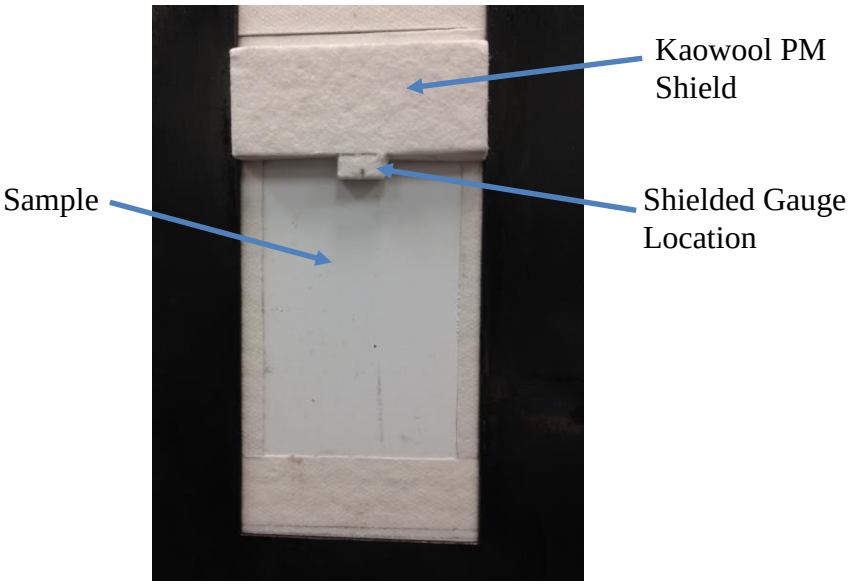

Figure 8. Kaowool PM shield used to protect gauge from surface deposits for a specified period of time.

Similar to mass loss tests for ABS, a radiant heater applying 10 kW/m^2 of external heat flux at the surface of the sample was utilized for ABS heat flux tests. The start time for ABS heat flux measurements, t=0, was the point when the heater was in position in front of the sample. In order to account for this additional heat flux, 10 kW/m^2 was subtracted from the measurements obtained during these tests.

4.4. FDS DNS SIMULATION

Two-dimensional (2D) direct numerical simulations (DNS) of upward flame spread over 5 cm PMMA samples were attempted using version 6.1.2 of Fire Dynamics Simulator (FDS). FDS is a computational fluid dynamics (CFD) solver developed by the National Institute of Standards and Technology that computes the Navier-Stokes equations for low-Mach flow scenarios [25]. The purpose of attempting to simulate the upward flame spread setup described in this work using FDS is to build a framework for comparing the results of the simulations to experimental results. Specifically, it is desired

to compare measured values of flame heat flux to those predicted by FDS. This is done in an exploratory manner to develop an initial understanding of the intricacies involved with comparing DNS calculations to experimental measurements.

Five different simulations were designed in order to begin to analyze the effects of numerical grid resolution, radiation heat transfer, and combustion model on the results. PMMA was chosen because its material properties, condensed-phase decomposition reaction kinetics, and heat flux from the flame have been well defined [36] [23]. The condensed phase material properties and reaction kinetics used in the FDS simulations are shown in Table 2.

Table 2. PMMA condensed phase material properties and decomposition reaction kinetics **[36]**.

Property	Value	Units
Absorption Coefficient, κ	2240	m^{-1}
Emissivity, ε	0.95	
Specific Heat Capacity, c_p	$0.6014 + (3.63 \times 10^{-4})T$	kJ/(kg-K)
Thermal Conductivity, k	(T<378K) $0.45 - (3.8 \times 10^{-4})T$	W/(m-K)
	(T>378K) $0.27 - (2.4 \times 10^{-4})T$	
Density, ρ	1155	kg/m^3
Pre Exponential Factor, A	8.6×10^{12}	s^{-1}
Activation Energy, E_a	1.881×10^5	J/mol

The change in thermal conductivity at 378 K is a consequence of PMMA's glass transition temperature being reached at this point. All other material properties were assumed to be the same for PMMA in both its glass and solid states. During the condensed phase reaction, 1.5% residue was assumed to form, with the remainder of the decomposition products assumed to be gaseous PMMA pyrolysates. The solid residue

and gaseous pyrolysates were assumed to have the same material properties as the condensed phase PMMA.

It has been well documented that the primary product of PMMA pyrolysis is its monomer, methyl methacrylate (MMA) [37] [38]. As a result of this, gas phase thermophysical properties and single-step combustion reaction kinetics are available in literature. Temperature dependent correlations for the thermal conductivity and dynamic viscosity of gaseous MMA were obtained from material property handbooks compiled by Yaws [39] [40]. The binary diffusion coefficient for air and MMA gas was calculated using the method of Fuller et al. [41].

$$\mathcal{D}_{AB} = \frac{0.00143T^{1.75}}{PM_{AB}^{\frac{1}{2}}\left[(\Sigma_v)_A^{\frac{1}{3}} + (\Sigma_v)_B^{\frac{1}{3}}\right]^2} \tag{9}$$

where $\mathcal{D}_{AB}$ = binary diffusion coefficient, cm^2/s
T = temperature, K
M_{AB} = $2[(1/M_A) + (1/M_B)]^{-1}$
M_A,M_B = molecular weights of *A* and *B*, g/mol
P = pressure, bar

Σ_v is found for each component by summing atomic diffusion volumes from lookup tables [41]. In this case, *A* and *B*, represent air and MMA gas with $\Sigma_{v,air}$ = 19.7 and $\Sigma_{v,MMA}$ = 110.2. The temperature-dependent heat capacity was calculated using the Joback method [41], a group contribution method which assumes each chemical group (i.e. $–CH_3$, $=CH_2$, etc.) within the molecule contributes a specific amount to the overall heat capacity of the molecule. Single-step gas-phase kinetic parameters were estimated by Seshardi and Williams for MMA using extinction measurements in oxygen-enriched air in a combustion tunnel [42]. Table 3 presents the values used in the FDS simulations

for the properties described above and the temperature ranges over which the correlations are valid.

Table 3. Gas phase thermophysical properties and reaction kinetics for methyl methacrylate (MMA).

Property	Value	Temp Range (K)	Units
Specific Heat Capacity, c	$(2.76 \times 10^{-6})T^2 + (1.02 \times 10^{-3})T + 0.34$	$T < 1000$	kJ/(kg-K)
	4.15	$T > 1000$	
Thermal Conductivity, k	0.015	$T < 373$	W/(m-K)
	$(1.85 \times 10^{-8})T$^2 + (5.64×10^{-5}) - 0.0086	$373 < T < 1000$	
	0.066	T >1000	
Dynamic Viscosity, μ	9.44 x 10^{-6}	$T < 373$	kg/(m-s)
	$(5.09 \times 10^{12})T$^2 + $(3.11 \times 10^{-8})T$ - 1.45 × 10^{-6}	$373 < T < 1000$	
	2.45 x 10^-5	T >1000	
Diffusivity,	$(4.54 \times 10^{-11})T^2 + (2.50 \times 10^{-8})T$ - 3.89 × 10^{-6}	---	m^2/s
Pre Exponential Factor, A	6.6 × 10^{12}	---	s^{-1}
Activation Energy, E_a	1.44 × 10^5	---	J/mol

Due to the computational cost of performing DNS simulations, it was desired to reduce the time required to reach ignition within the simulation. In order to accomplish this, a comprehensive 2D numerical pyrolysis solver, Thermakin2D [43], was utilized to obtain temperature profiles within the solid prior to ignition. Thermakin2D has shown excellent agreement with measured mass loss rates for PMMA in small-scale (< 20 cm) upward flame spread experiments as shown in Figure 9.

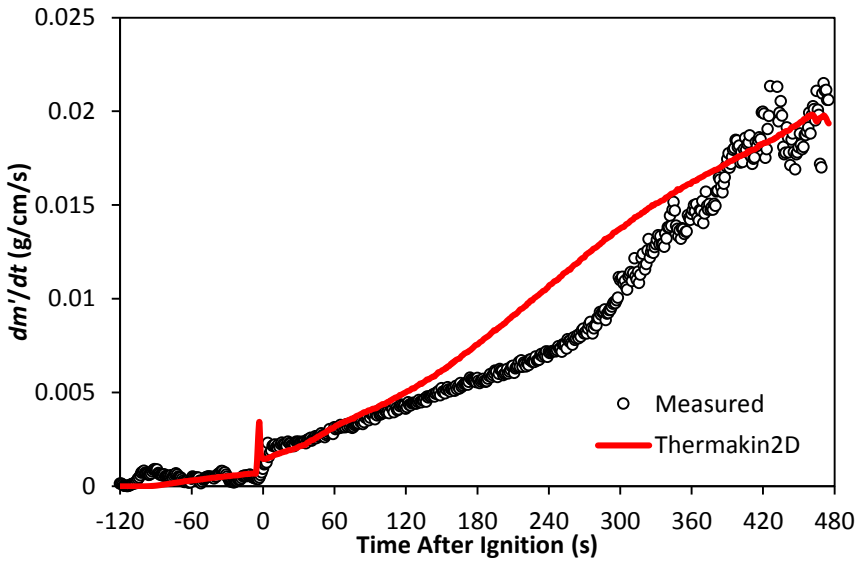

Figure 9. Predicted values from Thermakin2D compared to measured values of mass loss rate for 17.5 cm × 5 cm PMMA sample

The 125 second pre-heating period prior to ignition was simulated in Thermakin2D using a piecewise linear representation of the heat flux profile from the sample igniter as shown in Figure 10.

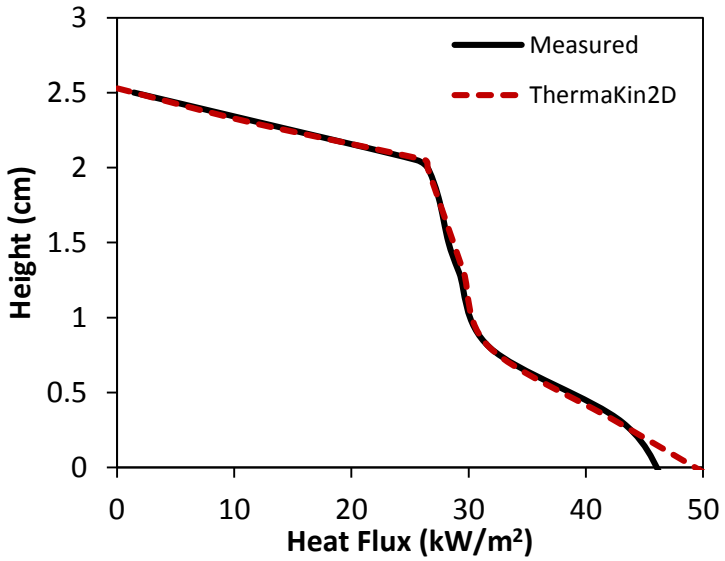

Figure 10. Comparison of simulated heat flux profile used in Thermakin2D to measured heat flux profile from sample igniter.

Since prescribing temperature profiles in the FDS simulation would be a lengthy and tedious process given the dependence of the temperature profile on the height within the sample, temperature profiles within the solid were averaged over 0.5 cm sections after 80 seconds of exposure to the sample igniter. Figure 11 shows the temperature profiles predicted after 80 seconds and the averaged temperature values used in the FDS simulation. The goal with this process was to limit the amount of time needed for pre-heating of the sample while still providing enough time for temperature profiles to develop within the material that were similar to those measured in Thermakin2D.

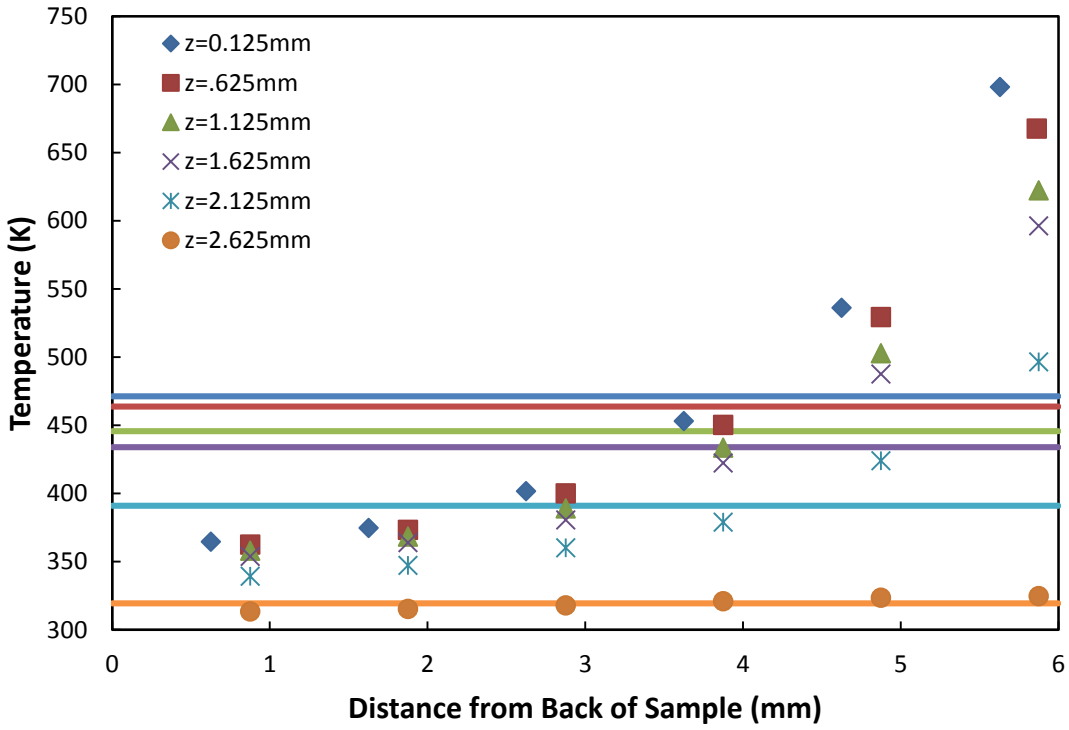

Figure 11. Plot comparing measured temperature profiles within PMMA sample (points) after 80 seconds of exposure to heat flux from sample igniter and the averaged temperature values (lines) used to minimize pre-heating time in the FDS simulation.

To ensure that this averaged temperature profile produced a similar temperature profile just before ignition, an FDS simulation with no gas-phase calculations was run. An important consideration when comparing the results from these simulations was the

type of heat flux applied to the surface to simulate the experimental sample igniter. The small size of the propane flame and its proximity to the surface of the sample indicates that, in the experiment, the heat flux to the bottom 2.5 cm of the sample during pre-heating is almost entirely convective. In FDS, it is not possible to specify a convective heat flux to a surface in simulations with gas-phase calculations turned off. Thus, a radiative heat flux with the same heat flux profile as shown in Figure 10 was applied in FDS to simulate the sample igniter. In Thermakin2D, a radiative or convective heat flux can be applied to the surface of the sample.

There was one more important comparison to make before moving forward with gas-phase simulations. Mass loss rates and ignition times were compared in FDS and Thermakin2D with only the radiative heat flux applied for 90 seconds to ensure that the pyrolysis models were consistent between FDS and Thermakin2D. Figure 12 shows how the two mass loss rate curves compare. It is clear from the plot that there is excellent agreement between the pyrolysis models with ignition times only differing by two seconds. This minor difference is likely due to how the two solvers treat radiation absorption in the condensed phase.

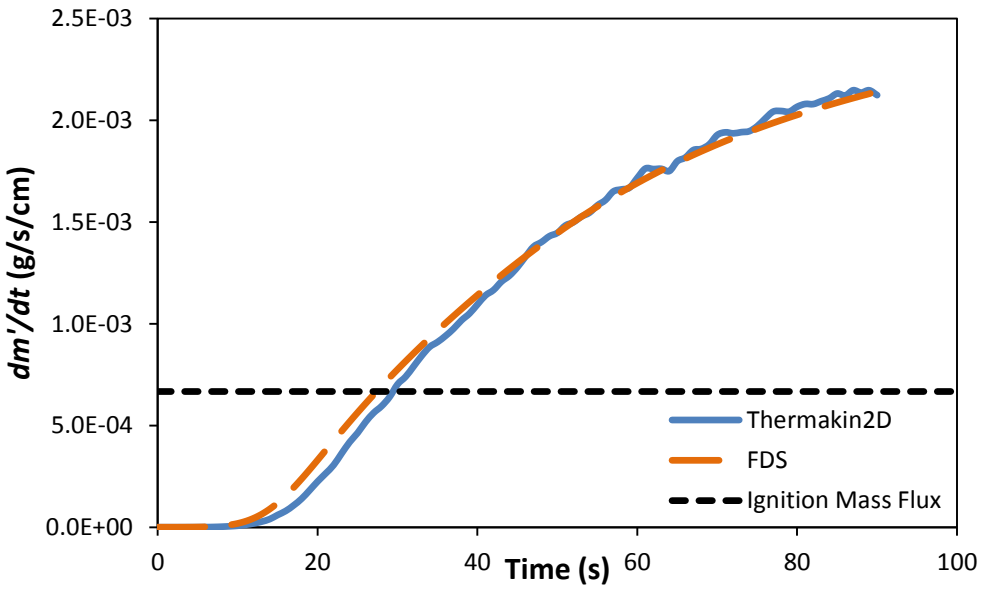

Figure 12. Compares mass loss curves produces by FDS and Thermakin2D for PMMA under the same radiative heat flux profile over a 90 second period.

For all five simulations, the domain dimensions and sample size remained the same. The sample was 5 cm tall and 5.9 mm thick and was surrounded behind, below, and above by 6 mm thick Kaowool PM insulation. There was 4 cm of 1.6 mm thick steel at the base of the domain to replicate the steel holder, followed by 2 cm of Kaowool PM, then the 5 cm sample, and lastly 5 cm of Kaowool PM above the sample. Figure 13 shows how the sample arrangement was represented in Smokeview, the visualization program for FDS. A distance of 6 cm in front of and below the sample to the edge of the domain was chosen in order to accurately capture the entrainment flow patterns and avoid errors from boundary conditions. A length of 5 cm between the top of the sample and the top boundary of the domain was chosen to limit the loss of radiation heat transfer back to the sample and prevent flow instabilities potentially created at the top boundary of the domain from traveling back to the sample. Since the simulation was only 2D the width

was not important other than how results are expressed. For simplicity and to highlight the fact that the calculations are 2D, a width of 1 cm was chosen.

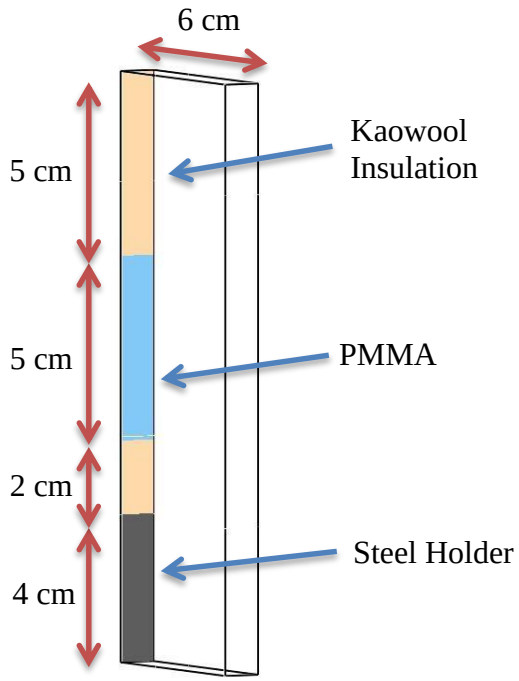

Figure 13. Smokeview representation of setup in FDS simulation with dimensions and labels added.

Three of the five simulations only varied the grid resolution between case runs. The characteristic length that needed to be resolved in these simulations was the thermal boundary layer. Ideally, the flame sheet, where the temperatures will be highest, would be resolved as well. The thermal boundary layer for these experiments was on the order of 1 – 1.5 cm, with the narrowest region at the base of the sample, and the flame sheet was on the order of 1 mm. For the simulation with the coarsest grid resolution, only a single mesh was used and the grid spacing was 0.4 mm, which produced 60,000 cells within the mesh. At this resolution, the thermal boundary layer has at least 20 – 25 cells across its width, which was sufficient to resolve the boundary layer but likely not enough to resolve the flame sheet.

The second simulation utilizes multiple meshes in order to achieve a finer resolution near the surface of the sample while limiting the total number of cells within the domain. For this simulation, the finest mesh was 2 cm wide, 9 cm tall, centered over the sample, and had 0.2 mm grid spacing for a total of 45,000 cells. The rest of the domain (above, below, and in front of the finest mesh) was comprised of three meshes with 0.4 mm grid spacing and a combined total of 35,250 cells. The boundary layer was now 40-50 cells wide but the flame sheet was only 4-5 cells wide, still not ideal for full resolution.

The last simulation had a mesh with 0.1 mm grid spacing that was 1.5 cm wide, 8 cm tall, and was centered over the sample, which resulted in 120,000 cells within the mesh. Surrounding this mesh above, below, and in front was three 1.5 cm wide meshes with 0.2 mm grid spacing and a combined total of 75,000 cells. This layer of meshes was surrounded by another layer of meshes that extended to the domain boundaries with 0.4 mm grid spacing and a combined total of 20,250 cells. With the flame sheet residing in the finest mesh in this domain, there were 8 – 10 cells spanning the width of the flame sheet, closer to the minimum number needed to be resolved.

FDS uses a gray gas model as the default setting for radiative transport calculations. This model works well for large-scale fires where soot is the predominant product controlling radiation from the fire because it assumes that the absorption coefficient of the gas is constant over all radiation spectrum. This is a reasonable approximation for soot, which has a continuous radiation spectrum, but for smaller fires with lower soot yields the gray gas model might over predict the radiation from the flame [44]. To check this, an additional case was run using the wide band model option in FDS

and specifying a soot yield for PMMA of 0.022 g/g [31]. This model uses six spectrum bands to characterize the spectral dependence of the radiative properties for the fuel gas and products of combustion. Band limits for these six bands have been measured from FTIR measurements and are tabulated within FDS for a select number of fuels, including MMA, as well as CO_2, H_2O, and soot [44].

The final simulation explores the effect of using a finite-rate combustion model rather than the mixing controlled model that is default within FDS. The mixing controlled combustion model assumes infinitely fast chemistry and makes use of the eddy dissipation concept to calculate the mass consumption rate of fuel within each cell [44]. On the other hand, the finite-rate combustion model calculates reaction rates using an Arrhenius model [44]. The complication that arises from using the finite-rate model is that an ignition or heat source must be included within the domain to initiate the combustion reaction. For this study, a small, 0.2 mm x 0.2 mm square ignition source kept at 1073 K was positioned 1.0 mm above the base of the sample and 0.8 mm in front of the sample. Since the ignition source projects a radiative heat flux onto the surface of the sample, the heat flux from the simulated sample igniter was modified so that, with the ignition source, the combined heat flux profile to the sample still resembled Figure 10. Additionally, a preliminary small-scale simulation was performed to determine the time at which the MMA vapors would ignite so the ignition source could be removed just after flame development in the full-scale simulation. The grid resolution for this model was the same as that used for the 0.2 mm grid default model.

Devices were positioned within all five simulations to measure net convective and radiative heat flux and surface temperature along the front face of the sample spaced 0.8

mm apart. Local mass loss rate measurements were also measured every 0.8 mm and internal temperature profiles were measured at three discrete locations in the sample. Lastly, temperature, velocity, MMA mass fraction, and heat release rate per unit volume (HRRPUV) slice files were measured in the gas phase.

5. EXPERIMENTAL RESULTS

5.1. MATERIAL OBSERVATIONS

5.1.1. Polymethyl Methacrylate (PMMA)

Upward flame spread progression on cast PMMA is depicted in Figure 14. Cast PMMA is ignited after 125 seconds of exposure to the sample igniter. Within 10 seconds of ignition the flame quickly grows to an approximate height of 4 – 5 cm. Within 30 seconds of ignition, a very thin layer of surface deposits begins to adhere to the surface downstream of the pyrolysis zone. This layer of deposits does not appear to impede the progression of flame spread but acts to increase the opacity of the surface. After two minutes of burning, the flickering flame tips have reached 20 cm above the base of the sample and the flame has transitioned from purely laminar behavior to transient laminar. Towards the end of the test (~500 – 600 seconds after ignition) burnout at the base of the sample begins to occur which ignites the epoxy behind the sample, as shown in the far right picture within Figure 14.

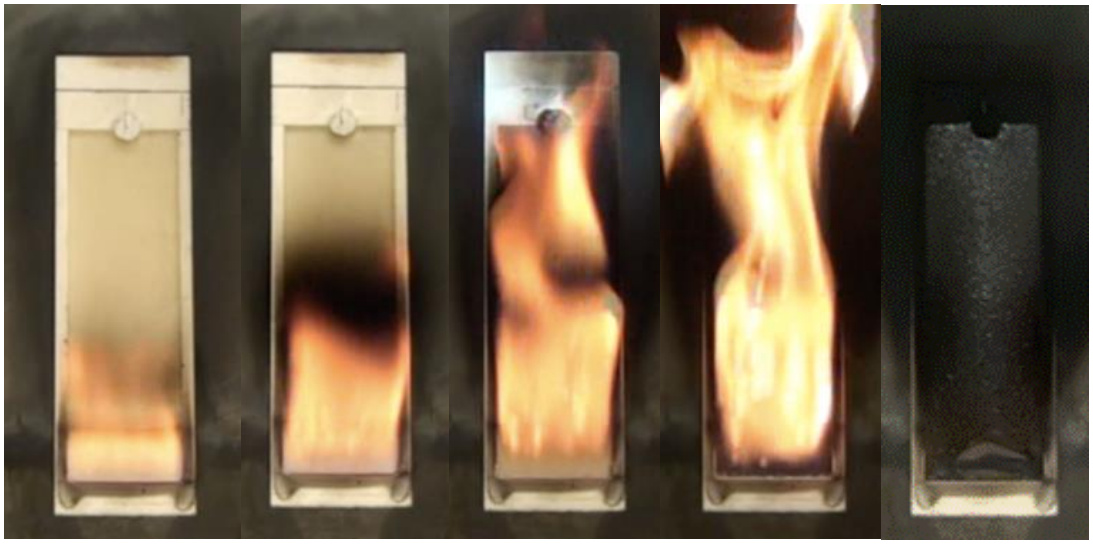

Figure 14. Upward flame spread progression on cast PMMA

For reference, pictures of the upward flame progression on extruded PMMA are also included as shown in Figure 15. The key difference in burning behavior between cast and extruded PMMA is the dripping behavior exhibited by extruded PMMA. During the first ~180 seconds after ignition extruded PMMA samples show little to no melt flow, with only small, narrow drips of melted polymer beginning to extend 1 cm below the sample's base. Around 240 seconds after ignition, drips of polymer melt begin intermittently falling from the sample to the base of the holder below. While the dripping behavior of extruded PMMA makes it difficult to study, the fact that dripping behavior is found in many other polymers and extruded PMMA is more common in industry than cast PMMA make it a worthwhile endeavor.

15 s 60 s 105 s 150 s 200 s

Figure 15. Progression of upward flame spread on extruded PMMA.

5.1.2. Polypropylene (PP)

Figure 16 gives a side-by-side comparison of the different stages of flame spread on polypropylene. PP is the easiest to ignite of the seven materials, requiring the lowest ignition time with the sample igniter at only 110 seconds. However, the flame height at ignition is relatively small, only 1-2 cm tall, and the rate of spread is noticeably slower than PMMA.

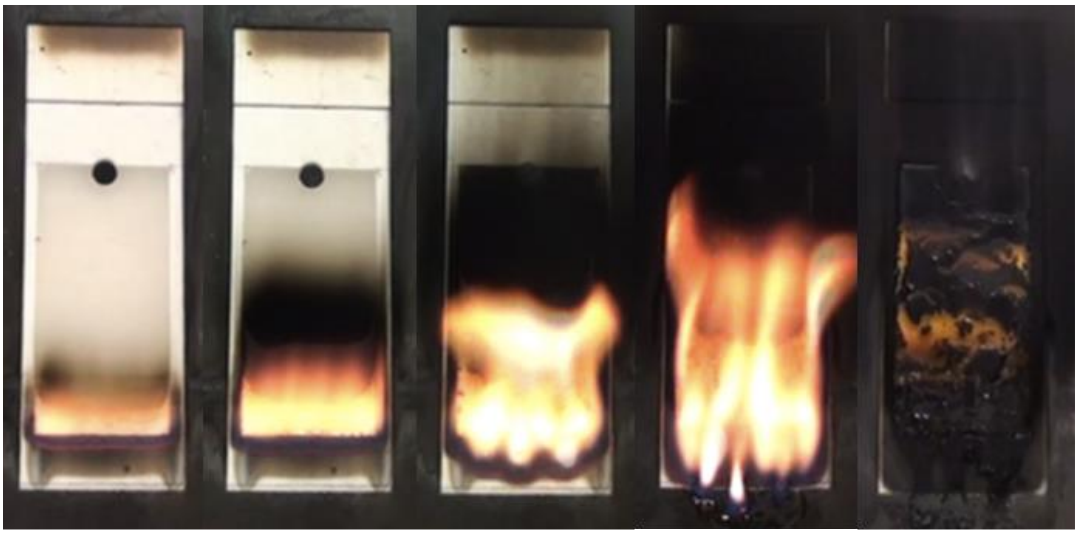

10s 60s 180s 300s Extinguish

Figure 16. Upward flame spread progression on 10 cm PP sample.

As the flame spreads upward, there are two layers of deposits that adhere onto the downstream surface, each with a different appearance. The first layer, which forms on the surface 2 – 3 cm ahead of the flame front, is very thin and matte in appearance while the second layer stays level with the flame height, is slightly thicker and denser, and is glossy in appearance. The glossy layer starts forming about 1 cm above the base of the sample within 15 – 20 seconds after the sample igniter is removed and spreads upward from there. Around 40 – 50 seconds after ignition, the glossy surface layer begins breaking apart into small pieces and sliding down the sample surface. As the surface layer breaks apart, more virgin sample is exposed and the pyrolysis front spreads upward. The pieces that break off become progressively larger until eventually, large, 2 – 4 cm chunks break off and slowly slide down the surface.

Polypropylene exhibits a tendency to melt and flow fairly quickly. This behavior leads to the sample flowing into and along the front surface of the bottom strip of Kaowool PM as the test progresses. Already by the time of ignition, the sample and thus

the base of the flame has extended down 0.5 cm below the bottom of the sample. For the most part, the burning rate is able to keep up with the amount of material that flows down the surface of the sample. However, the pieces of surface layer deposits that slide down the surface eventually reach the bottom of the sample and act as vessels to carry burning melt flow further below the base of the sample. On average, it takes five minutes after ignition for the melt flow to travel 2 cm below the bottom of the sample and reach the metal of the steel sample holder. The progression of melt flow is noticeable in Figure 16. Roughly seven minutes after ignition, the sample has been completely consumed at the base of the sample and the epoxy begins to contribute to the flame. The point at which this occurs is easy to detect because the epoxy produces large flamelets that disrupt the smooth flame sheet produced by polypropylene.

5.1.3. Polyoxymethylene (POM)

The progression of upward flame spread of polyoxymethylene is shown in Figure 17. POM takes longer to ignite, 135 seconds, and produces a completely blue flame. The blue flame is indicative of the fact that oxygen makes up 53% of POM's molecular weight. Similarly to polypropylene, the flame starts out 1 – 2 cm tall right after ignition and the spread rate is relatively slow. Unlike other materials studied in this work, POM does not produce soot and no deposits accumulate on the surface of the sample throughout the duration of the test.

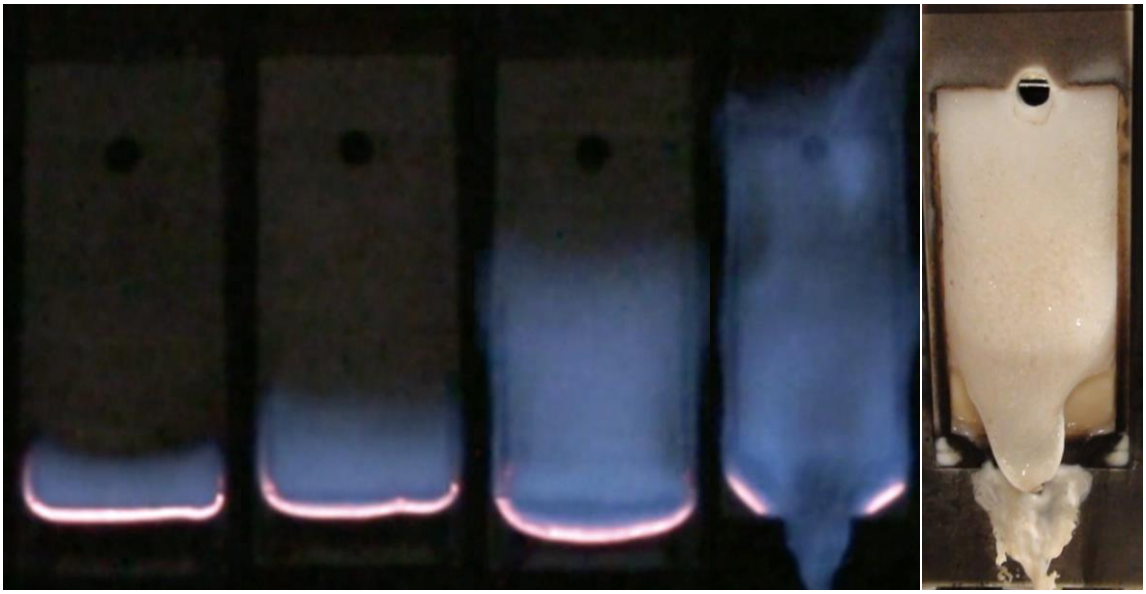

10 s 60 s 180 s 340 s Extinguish

Figure 17. Progression of flame over 10 cm POM sample.

POM exhibits melt flow but it is difficult to perceive until later in the test. Very little material spills over onto the front surface of the bottom insulation piece, instead the melted POM absorbs into the Kaowool PM and continues burning through the densely porous insulation. As the melt flow travels down into the insulation, the base of the flame also steadily lowers until it becomes seated 2 cm below the bottom of the sample where the insulation meets the metal of the steel sample holder. The base of the flame would typically reach the metal sample holder 5.5 minutes after ignition. Beginning around 5.5-6 minutes after ignition, the base of the sample beings to bulge out and by 6.5 – 7 minutes significant melt flow involving almost the entire 3 cm of the sample begins to spill over the bottom of the sample and onto the steel sample holder. The last two images in Figure 17 show an example of the onset of melt flow while burning and after extinguishing.

5.1.4. High Impact Polystyrene (HIPS)

The progression of upward flame spread on high impact polystyrene is depicted in Figure 18. HIPS ignites within 120 seconds of applying the sample igniter and initially spreads quickly but is slowed immediately by the significant accumulated of surface layer deposits. A 2 cm tall flame right at ignition grows to 4 cm within the first 5 seconds. In the same time span, the entire surface 4 cm above the flame has already been covered by a thin layer of surface deposits. Within 20 seconds of ignition the flame is 5 cm tall and is being fed by a narrow, 0.5 – 1 cm, pyrolysis zone at the base of the sample. One minute after ignition the flame is 7 – 8 cm tall but the pyrolysis front has not spread past 1 cm and the surface layer continues to thicken both downstream on virgin surface and on the surface layer already present. At this point the flame height no longer increases and the surface layer begins to develop new characteristics. Instead of the surface layer just getting thicker, small branches start to form that stick out from the surface and grow in size as more deposits adhere to them. Three minutes into burning the branches are up to 1 cm long in the vertical direction and stick out 2 – 3 mm from the surface. These branches can be seen in the two pictures on the right of Figure 18.

Figure 18. Flame spread progression over 10 cm HIPS sample.

Four minutes after ignition the branches continue to increase in size and are noticeably interfering with the boundary layer flow and the flame height begins to decrease. Meanwhile, the pyrolysis zone has shifted downward because of melt flow so that the base of the flame is rooted 0.5 – 1 cm below the bottom of the sample. The flame now has two distinct behaviors; a portion that continues to flow upward but must fight through the maze of branches that now cover over two-thirds of the surface and a portion that consists of flamelet bursts that project directly down or outward up to 2 cm from the base of the flame. If left to continue burning the branches increase in size and flame height decreases until the surface layer cools the flame so much that it can no longer be sustained. This point of self-extinction typically occurs 20 – 30 minutes after ignition.

5.1.5. Fiberglass Reinforced Polyester Resin (FRP)

A side-by-side comparison of upward flame spread progression on fiberglass reinforced polyester resin is given in Figure 19. FRP can be ignited in 135 seconds but is a very weak flame at first so the sample igniter must be removed slowly or the flame can be extinguished. The initial flame is approximately 2 cm tall and spreads at a constant rate to a height of 4 cm within the first minute all while a thin layer of deposits begins adhering to the surface. After the first minute of burning, the spread becomes more sporadic and is controlled by small pockets of fuel vapors that surge out of the layers of woven fiberglass to preheat the sample downstream. Also at this time the base of the flame at the corners of the sample begins to travel upwards as the fuel vapors are no longer able to reach the surface in sufficient quantities to sustain a flame.

Figure 19. Flame spread progression of 10 cm FRP sample.

The first minute of burning also marks the point at which the surface deposits have fully covered the surface of the sample 4 cm above the top of the flame, approximately twice the height of the flame. This results in limited further flame spread, with the pyrolysis zone not extending beyond the initial 4 cm that was preheated by the first minute of burning. The flame height becomes difficult to gauge at this point because flames frequently travel up the sides of the sample ahead of the rest of the flame and either extinguish or burnout at the top of the sample, leaving a narrow 3 cm wide flame in the middle of the sample. The remaining flame either slowly advances up the middle of the sample at a constant flame height until it burns out at the top or it flickers in place until extinction.

5.1.6. Glass Filled Polybutylene Terephthalate (PBT)

The progression of upward flame spread on glass filled polybutylene terephthalate is displayed in Figure 20. PBT is easily ignited after a 120 second exposure from the sample igniter. The initial 2 cm flame spreads to 5 cm tall within 90 seconds of ignition and a thin layer of deposits adheres to the surface 5 – 6 cm above the top of the flame.

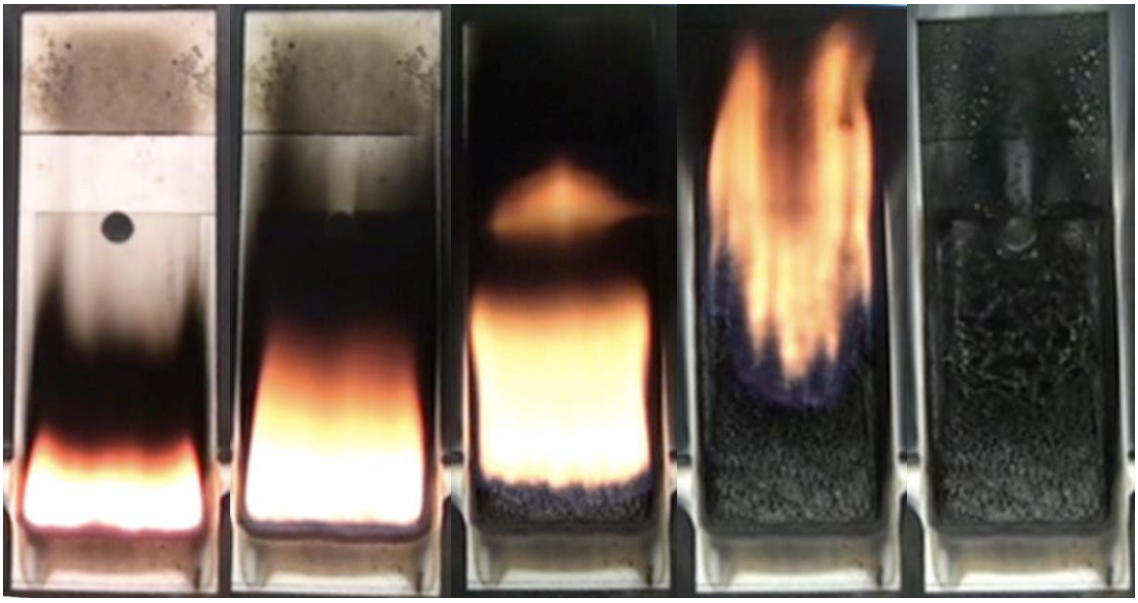

10 s 60 s 180 s 600 s Extinguish

Figure 20. Flame spread progression over 9 cm PBT sample.

The base of the flame, bright yellow just after ignition, begins to turn blue after two minutes of burning and then begins advancing upwards after 2.5 minutes of burning, starting at the corners first. Due to the presence of 25% glass, the sample does not burn through to the epoxy but, instead, leaves behind a glass and residue structure as the base of the flame travels upwards. Despite the surface layer deposits above the flame, the pyrolysis front continues travelling up the sample, as demonstrated by the flamelets that occasionally protrude from the flame sheet well above the base of the flame. Unlike PMMA, which exhibits a pulsing behavior, the flame sheet produced by PBT stays smooth and steady for a majority of the flame length, as shown in Figure 20. As the base of the flame travels up the surface the edges advance faster than the middle so the base of the flame becomes U-shaped the further it travels up the sample. The flame continues this way until the edges burnout at the top of the sample and a narrow flame in the middle is

all that remains, which continues burning for 1 – 2 minutes until it flickers and self-extinguishes.

5.1.7. Acrylonitrile Butadiene Styrene (ABS)

At 205 seconds, acrylonitrile butadiene styrene (ABS) takes the longest to ignite of the seven materials analyzed in this study. Within 10 seconds of ignition, a thin layer of deposits adheres to the entire surface of the sample. Without the external radiative heater, flame spread would be limited, but with the help of the additional 10 kW/m^2 of external radiation, the pyrolysis front is able to spread upwards. The spread of the pyrolysis front is indicated by cracks that form in the surface layer. As the flame spreads upwards, the surface layer gets progressively thicker but the cracks in the surface layer also widen and travel upwards, which allows for continued flame spread. For a detailed description of ABS burning behavior during upward flame spread, see the work by Leventon and Stoliarov [45].

5.2. MASS LOSS RATE

For each test, mass loss measurements were used to calculate a mass loss rate at each time step using Equation (6). These calculated mass loss rates at each time step were noisy so the mass loss rate for each test was smoothed using a seven second moving average. At least three tests were performed for each material at a height determined by how high the pyrolysis front would travel during a test. The tallest sample height able to be tested in the sample holder was 15 cm. 15 cm mass loss rate tests were performed for materials that exhibited flame spread such that the pyrolysis front reached a height of 15

cm prior to the onset of non-ideal burning behavior. This included cast PMMA, PP, ABS, and glass filled PBT. Materials whose pyrolysis front did not reach 15 cm before non-ideal burning behavior began were tested using smaller sample heights, $10 \leq y < 15$ cm. The smoothed mass loss rates for each test were averaged at each time step to give an averaged mass loss rate for each material. This smoothed average mass loss rate was smoothed a second time using an additional seven second moving average and then normalized by the width of the sample, 5 cm.

All materials burned with a constant width of 5 cm except FRP, which exhibited an increasingly narrow burning region as the test progressed, as shown in Figure 19. In order to account for this, videos of FRP tests were post-processed to determine if there was a consistent time-dependent nature to the decreasing width of the burning region. As shown in Figure 21, the data can be represented by a line of fit reasonably well. The line of fit shown in Figure 21 is a piecewise linear function with one linear curve between 5 and 4.5 cm and a separate linear curve for widths less than 4.5 cm.

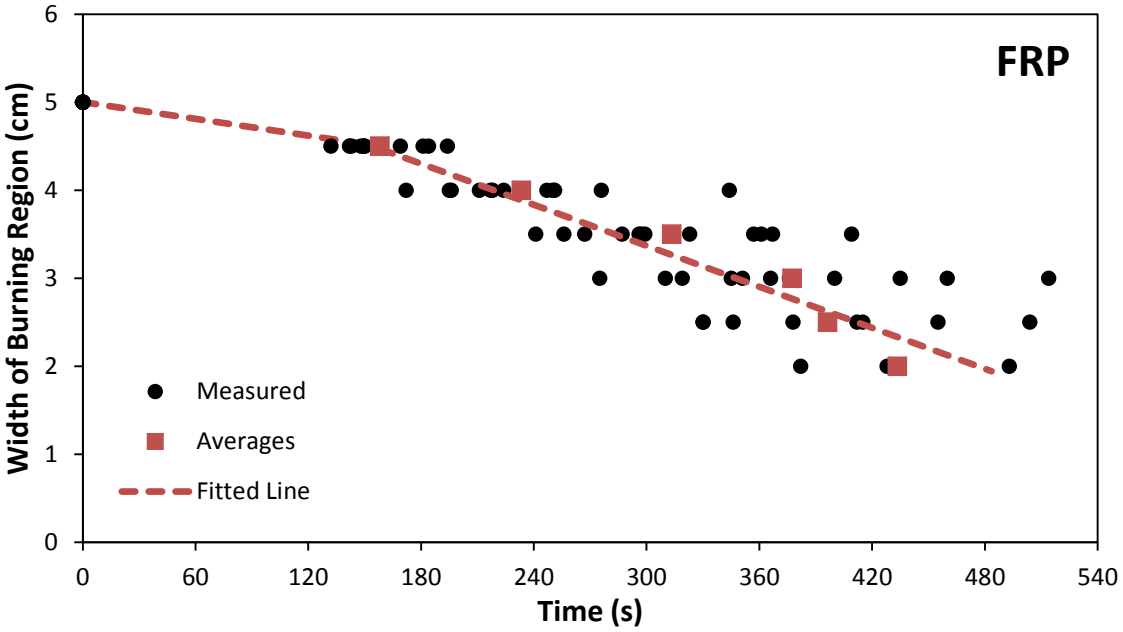

Figure 21. Shows decreasing trend in width of burning region with respect to time for FRP tests. Red squares represent average time values at each 0.5 cm. A piecewise linear function is used to represent the measurements.

When normalizing by the time-dependent width obtained from Figure 21 instead of a constant 5 cm, the width normalized mass loss rate is adjusted to account for the decreasing width of the burning region. Figure 22 shows how the width normalized mass loss rate is impacted when this adjustment is made. As a note, for the purposes of predicting heat flux to the surface, this adjustment can only be applied when the narrowed burning region remains in the center of sample since this is where heat flux measurements were acquired.

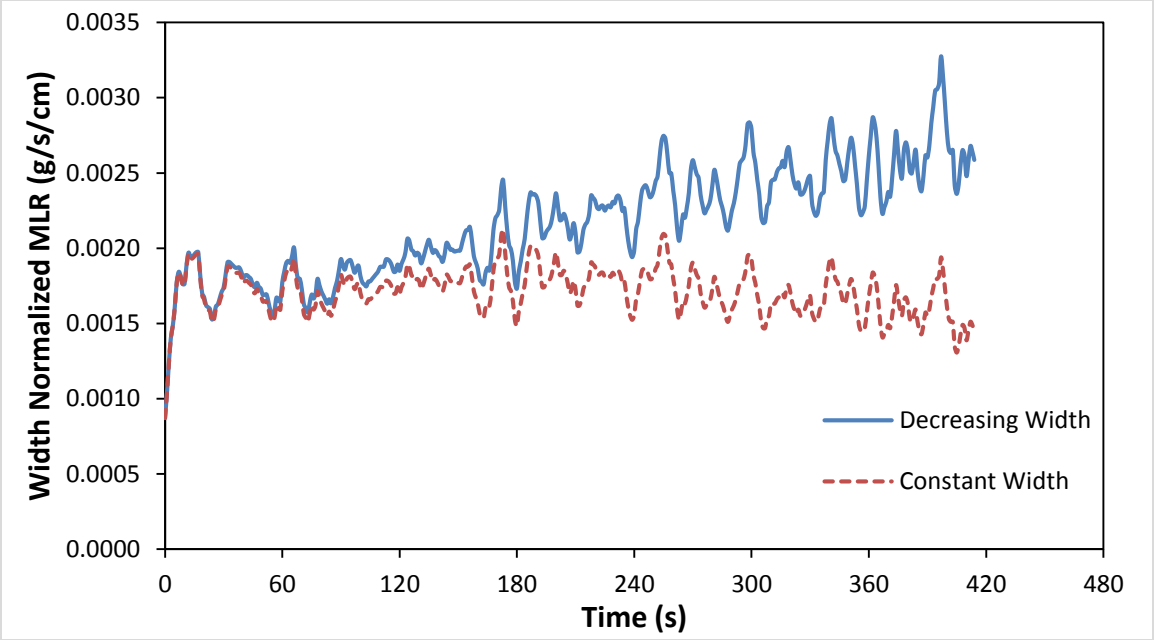

Figure 22. Shows effect of accounting for decreasing width of burning region during FRP tests when using a width normalized mass loss rate.

$\frac{dm'}{dt}$ curves for each material were fit with a polynomial curve to remove noise from the prediction. Fitted polynomial curves for each material ranged from 2nd to 5th order. Figure 23 shows the smoothed average $\frac{dm'}{dt}$ and fitted polynomial curves for each material and the sample height, *y*, used to collect the measurements for each material. Equation (10) gives the basic form of the polynomial equation with the polynomial coefficients *a* – *f* listed for each material in Table 4. Table 4 also provides the time range after ignition over which the fitted polynomial is valid.

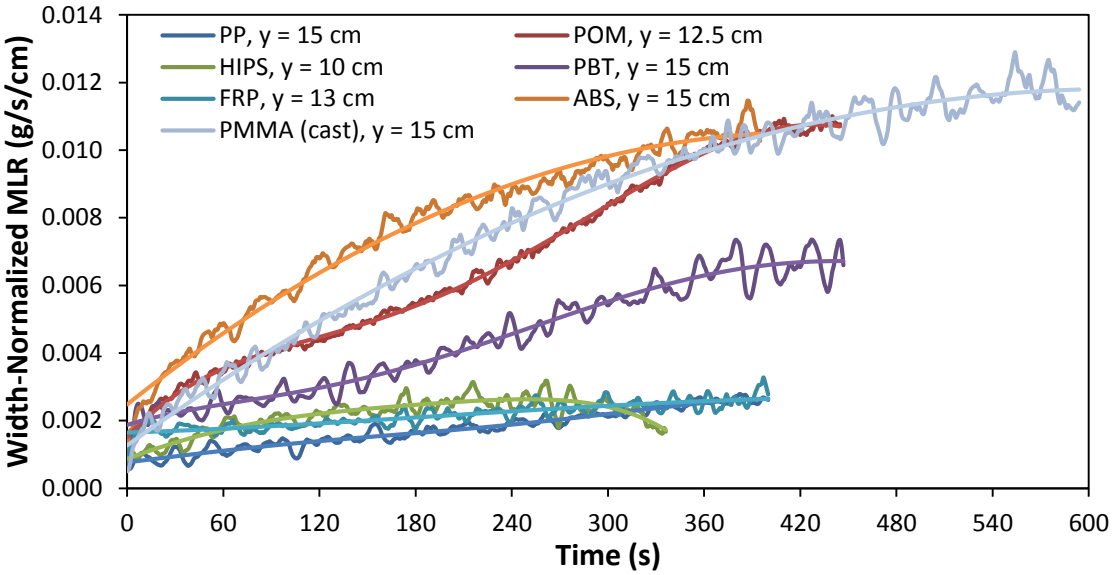

Figure 23. Averaged $\frac{dm'}{dt}$ curves for each material with corresponding fitted polynomial curves.

$$\frac{dm'}{dt} = a(t - t_{ign})^5 + b(t - t_{ign})^4 + c(t - t_{ign})^3 + d(t - t_{ign})^2 + e(t - t_{ign}) + f \quad (10)$$

Table 4. Polynomial coefficients for fitted $\frac{dm'}{dt}$ curves used in Equation (10) and shown in Figure 23 along with the time ranges after ignition for which they are valid.

Material	Time Range (s)	Fitted *dm'/dt* Polynomial Coefficients					
		a	***b***	***c***	***d***	***e***	***f***
POM	0 - 445	1.64E-15	-3.07E-12	1.78E-09	-3.98E-07	5.18E-05	1.51E-03
FRP	0 - 415	---	---	-1.35E-11	7.87E-09	1.49E-06	1.65E-03
PBT	0 - 450	1.24E-15	-1.72E-12	7.58E-10	-1.14E-07	1.47E-05	1.87E-03
PMMA (ext.)	0 - 460	-5.40E-15	4.35E-12	-8.13E-10	4.75E-09	2.79E-05	1.45E-03
PMMA (cast)	0 - 600	---	---	---	-2.74E-8	3.40E-5	1.27E-3
ABS*	0 - 50	---	---	---	-6.84E-07	9.13E-05	1.56E-03
	50 - 395	-1.20E-14	1.36E-11	-5.55E-09	9.58E-07	-4.12E-05	4.74E-03
	395 - 480	---	---	---	---	---	1.08E-02
HIPS	0 - 330	-3.38E-15	1.82E-12	-2.20E-10	-4.85E-08	1.77E-05	8.67E-04
PP	0 - 400	-8.11E-16	6.66E-13	-1.59E-10	6.36E-09	5.79E-06	7.65E-04

* Measured with q_e" = 10 kW/m^2

5.3. BASE OF FLAME LOCATION

As described earlier, the predicted heat flux is dependent on the distance from the base of the flame to the height at which measurements are taken, y. At the beginning of the test, y is simply the sample height, but as the sample begins burning the base of the flame may not remain fixed at the bottom of the sample. The location of the base of the flame with respect to the bottom of the sample, y_b, is used in the calculation of the normalized length scale, y^*, in Equation (4). Thus it is important to have an accurate quantitative representation of y_b over the entire testing period.

For materials that drip, the base of the flame moves downward as the sample melts and continues burning while absorbing into the insulation below and/or sliding down the face of the insulation. In this study, the materials that exhibited a downward moving flame base were PP, POM, and HIPS. On the other hand, PBT and FRP had a flame base that travelled up the sample as the test progressed. Not coincidentally, these are the only materials in this study that are reinforced with an inert substance. The location of the flame base on ABS samples remained fixed to the base of the sample throughout the test. The movement of the flame base for each material can be seen in the images of flame spread in Section 5.1.

For each test, the location of the flame base was carefully tracked with respect to its starting position using video recordings and a reference scale. The location of y_b was defined as the average location of the base of the flame (blue or yellow) across the width of the flame and was tracked in 0.5 cm increments. Using this data, a piecewise linear function could be formulated that described the time-dependent nature of the flame base.

Figure 24 through Figure 28 show the results of this analysis for each material along with the fitted line that was used to represent the flame base movement for heat flux predictions in the next section.

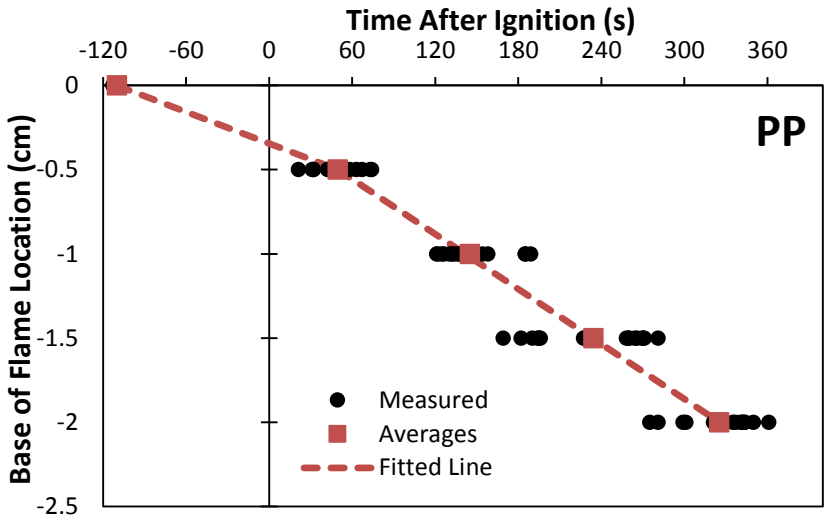

Figure 24. Shows downward movement of flame base over time with respect to the bottom of the sample for PP.

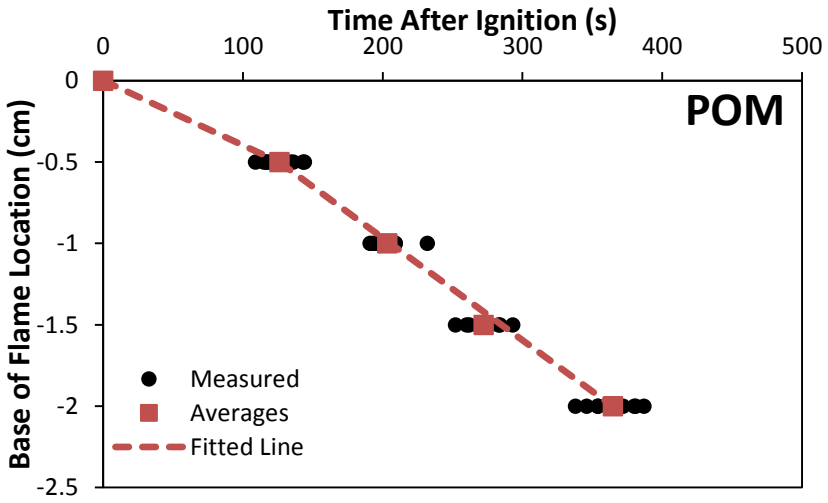

Figure 25. Shows downward movement of flame base over time with respect to the bottom of the sample for POM.

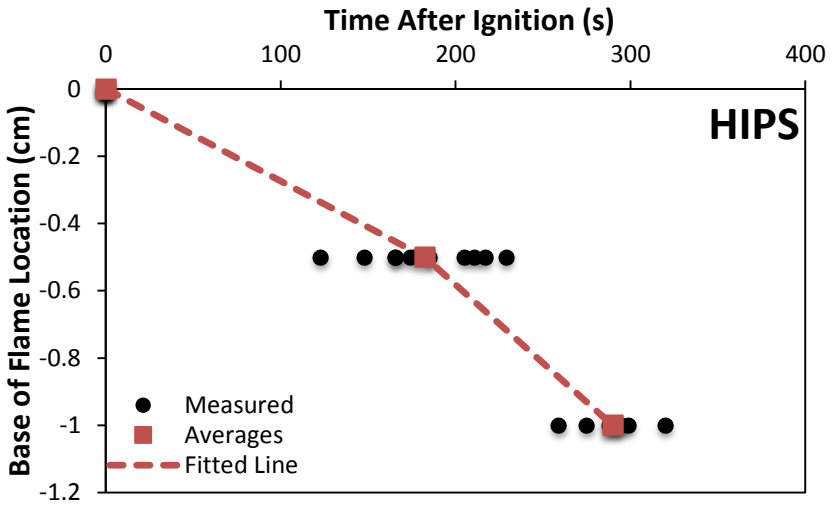

Figure 26. Shows downward movement of flame base over time with respect to the bottom of the sample for HIPS.

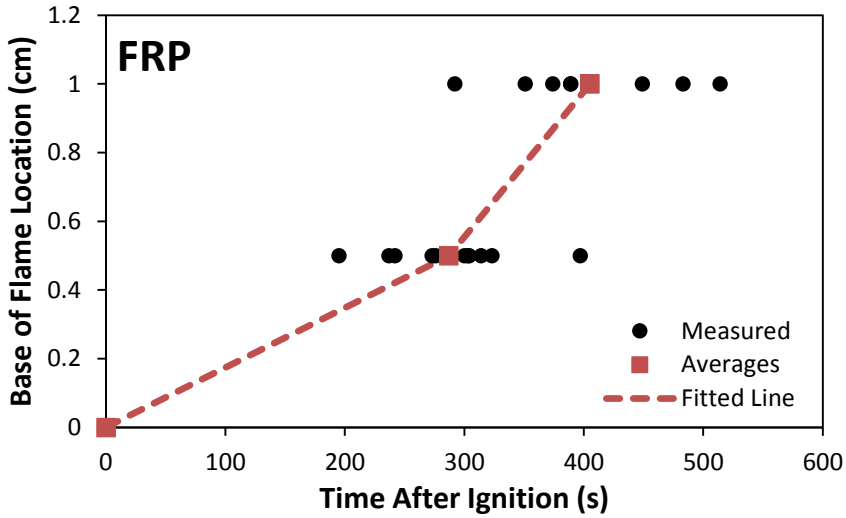

Figure 27. Shows upward movement of flame base over time with respect to the bottom of the sample for FRP.

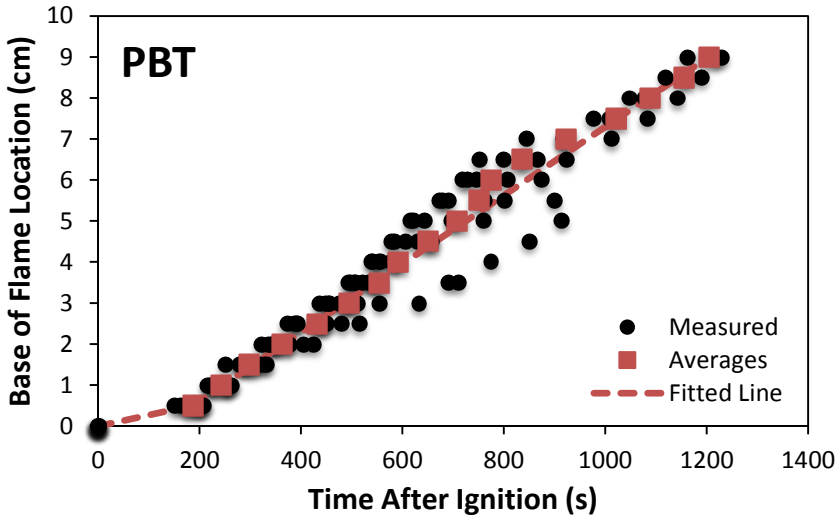

Figure 28. Shows upward movement of flame base over time with respect to the bottom of the sample for PBT.

The equations that represent the fitted lines were added to the original height of the sample in the calculation of the normalized length scale, y^* (Equation (4)), so materials that dripped would have an increasing distance between the base of the flame and the measurement location and for materials that exhibited an upward moving flame base this distance would decrease over time. Table 5 gives the equations for y_b for each material.

Table 5. y_b equation parameters for each material and the ranges of y_b over which they apply.

Material	y_b Range (cm)	Slope	Intercept
PP	0 - 0.5	-3.13E-03	-0.34
	0.5 - 2.0	-5.44E-03	-0.23
POM	0 - 0.5	-3.97E-03	0
	0.5 - 2	-6.28E-03	0.29
HIPS	0 - 0.5	-2.74E-03	0
	0.5 - 1.0	-4.66E-03	0.35
PBT	0 - 0.5	2.66E-03	0
	0.5 - 9	8.36E-03	-1.07
FRP	0 - 0.5	1.74E-03	0
	0.5 - 1	4.24E-03	-0.72

5.4. HEAT OF COMBUSTION

The heats of combustion of all seven materials are listed in Table 6 for each orientation that they were tested in. Combustion efficiencies are also listed in Table 6 as calculated from Equation (8). Heats of combustion values for the horizontal orientation and combustion efficiencies are compared to values from literature and show good agreement. Values from MCC tests are also included as a reference for complete heat of combustion as described in Section 4.3.2 [34]. In addition, Figure 29 shows a plot with the measured heats of combustion for each material to better compare the results from each orientation. The error bars in Figure 29 represent two times the standard deviation of the mean and, for every combination of material and test orientation except FRP vertical with external heat flux (one test), and ABS and PBT vertical with no external heat flux (two tests), the mean was calculated using at least three and up to five test results. It is important to note that these values represent the heat of combustion per volatilized mass.

Table 6. Heat of combustion results compared to literature and MCC (ΔH_T) values.

Material	Heat of Combustion of Volatiles (kJ/g)					Combustion Efficiency (χ_e)	
	$\Delta H_{eff,H}$		$\Delta H_{eff,V}$	ΔH_{vert}	ΔH_T [34]		
	This Study	Lit.[a]				This Study	Lit. [46]
POM	14.9	14.4	14.6	11.8	14.0	1.06	0.94
FRP	20.5	23.4[b]	20.4	23.9	22.7[c]	0.90	0.94
PBT	21.6	21.7	---	20.2	23.2[c]	0.93	0.91
PMMA (ext.)	23.8	24.2	24.2	20.0	24.5	0.97	0.99
PMMA (cast)	24.4		24.0	21.3		1.00	0.99
ABS	28.4	30.0	29.3	31.0	36.5	0.78	0.79
HIPS	27.8	27.0	30.2	30.1	39.2	0.71	0.76
PP	37.9	38.6	37.7	31.7	41.0	0.92	0.97
HDPE	39.1	38.4	37.9	32.8	42.2	0.93	0.97

a) POM, PMMA, ABS, HIPS (as PS), PP, and HDPE from [31]. FRP and PBT from [46].

b) Value is for an unsaturated polyester thermosetting resin, similar to our material, but due to proprietary limitations, it is not known if this is the exact chemical match as our polyester

c) PBT from [35], FRP from our research group

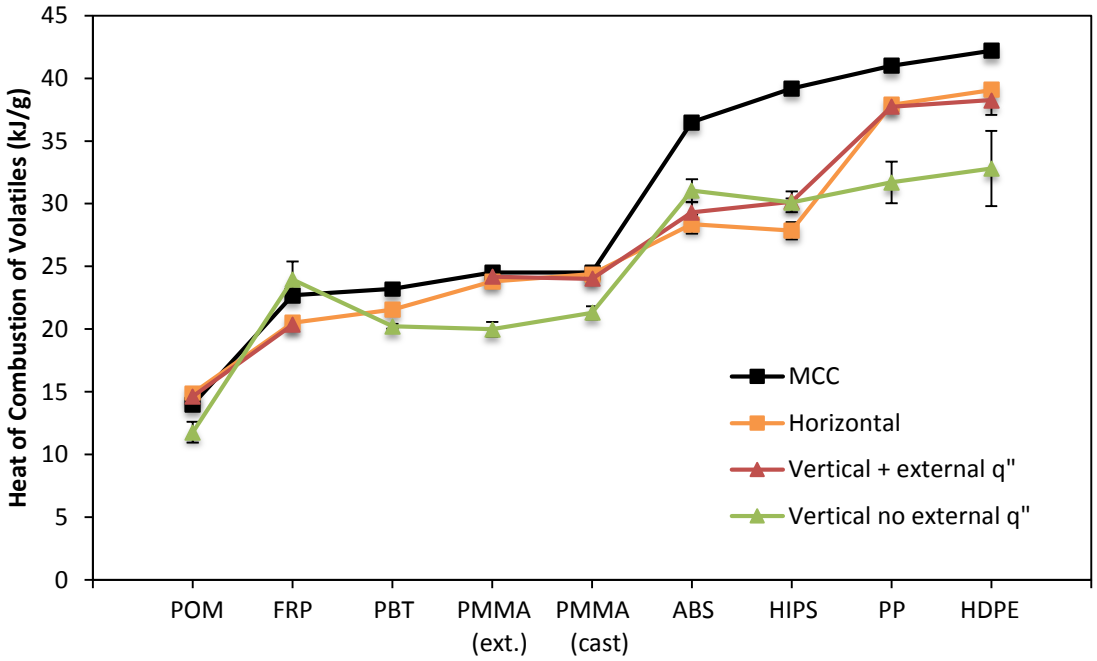

Figure 29. Heat of combustion results where each line represents a different orientation.

As expected, the materials with lower combustion efficiencies like HIPS and ABS have greater discrepancies between their horizontal heat of combustion values and MCC values. Perhaps not as expected, the vertical heat of combustion results with no external heat flux were noticeably lower than horizontal values for some materials, specifically, POM, PMMA, PP, and HDPE. Several factors were considered as potential causes for this difference including sample width, external heat flux, and surface temperature.

The width of the sample could be a factor if pyrolyzed fuel was escaping from the sides of the sample without being burned, thus increasing the mass loss rate without increasing the heat release rate. To test this hypothesis, 10 cm wide samples were burned within the cone calorimeter. Since the sample igniter is designed for 5 cm wide samples, the 10 cm wide samples were ignited instead using the cone heater and a spark igniter. In order to test the width hypothesis while only changing one variable (just the width instead of both the width and the external heat flux), 5 cm wide samples were also tested using the cone heater and a spark igniter. Measured $\Delta H_{eff,V}$ values from the 5 cm wide and 10 cm wide tests with the same external heat flux were nearly identical, as shown in Table 7.

Table 7. Heat of combustion results from 5 cm and 10 cm wide samples with external heat flux, q_e'' = 30 kW/m^2

Material	Width (cm)	Measurement Time (s)	Avg. HRR (kW)	$\Delta H_{eff,V}$ (kJ/g)
POM	10	144	2.7	14.8
	10	123	2.7	15.0
	5	148	1.3	14.1
FRP	5	332	0.9	20.4
PMMA (ext.)	10	139	4.8	24.1
	10	51	4.3	24.3
	5	65	2.2	24.1
PMMA (cast)	10	211	4.7	24.1
	10	203	4.9	24.2
	5	197	2.3	23.6
ABS	10	56	5.4	28.5
	10	168	5.2	29.5
	5	169	2.8	29.9
HIPS	10	111	4.9	29.5
	10	134	5.0	30.0
	5	133	2.9	30.9
PP	10	61	4.9	37.5
	10	45	5.0	38.3
	10	66	4.6	37.7
	5	67	1.6	37.5
HDPE	10	97	4.4	37.9

In Table 7, "Measurement Time" refers to the amount of time during the test where measurements are being used to calculate the heat of combustion. The average heat release rate (HRR) is provided as a reference for fire size. Tests on FRP and HDPE were limited to one 5 cm test because of limited material availability in the case of FRP and difficulties with sample deformation and collapse prior to and just after ignition in the case of HDPE. Since the 5 cm and 10 cm wide results are indistinguishable for each material, the results from these tests are averaged to give one representative value for vertical tests with an external heat flux of q_e'' = 30 kW/m^2.

The averaged heat of combustion values from the vertical tests with q_e'' = 30 kW/m^2 were also very similar to the horizontal results, as shown in Table 6 and Figure 29. It is speculated, then, that the reduction in combustion efficiency in the vertical orientation with no external heat flux is due, at least in part, to the flame being in contact with a cooler surface relative to the temperature of the flame. During upward flame spread, a majority of the flame is in contact with material that has not begun pyrolyzing so the temperature of the material's surface would be much cooler than the flame temperature. This significant temperature difference could be interfering with the chemical combustion process resulting in inefficient combustion. In the case of vertical tests with an external heat flux, there are two factors that prevent the same decrease in combustion efficiency as the vertical tests with no external heat flux. First is the obvious fact that the addition of q_e'' = 30 kW/m^2 of heat increases the temperature of the sample surface substantially. Secondly, the entire surface ignites almost simultaneously so there is no flame spread and thus no portion of the flame is in contact with material that is not pyrolyzing. All vertical tests with an external heat flux were performed under the same q_e''. For future work, it would be interesting to see if decreasing q_e'' would cause a noticeable decrease in the combustion efficiency for vertical tests.

In the horizontal orientation, most of the flame is present above the sample and not in contact with the surface of the sample. If the drop in combustion efficiency is related to the proximity of the flame to the cold surface then performing tests in the horizontal orientation with no external heat flux should not result in decreased combustion efficiency. To confirm this, horizontal heat of combustion tests were performed with no external heat flux as described in section 4.3.2 for cast PMMA, PP,

and HDPE. The results of these tests are compared to horizontal with external heat flux and vertical with and without external heat flux tests in Table 8.

Table 8. Comparison of heat of combustion results for horizontal and vertical tests with and without an external heat flux.

Material	Heat of Combustion of Volatiles (kJ/g)			
	Horizontal		Vertical	
	$\Delta H_{eff,H}$	ΔH_0	$\Delta H_{eff,V}$	ΔH_{vert}
PMMA (cast)	24.4	25.3	24.0	21.3
PP	37.9	40.2	37.7	31.7
HDPE	39.1	41.5	38.2	32.8

It is evident from the results shown in Table 8 that the lack of external heat flux does not result in a reduced combustion efficiency as seen in vertical tests. Instead, the heat of combustion increases slightly for the horizontal tests with an external heat flux, which could be due to the smaller, and thus more efficient, flames present during these tests.

FRP, PBT, ABS, and HIPS do not show this same reduction in heat of combustion for the vertical orientation with no external heat flux. In fact, these materials, except PBT, all have slightly higher heats of combustion in this orientation compared to the horizontal values. These materials have two unique properties that could be contributing to this result. First, all four materials, especially HIPS and ABS, produce a thicker surface layer compared to POM, PMMA, PP, and HDPE. This thicker surface layer is highly insulating so the surface temperature of this layer becomes much hotter as the hot plume and flames come in contact with it compared to the surface of virgin polymer. PP also produces a surface layer but it is much thinner and denser in comparison to HIPS and ABS. FRP and PBT develop surface layer as well but not to the same extent as HIPS and ABS. However, both FRP and PBT contain an inert substance

(25% chopped glass fibers in PBT and ~50% woven fiberglass in FRP) that affects the overall thermal behavior of the material. Glass has a lower heat capacity than any of the polymers tested so the surface temperature increases faster. Additionally, glass does not decompose and its melting point is much higher than polymers so it can reach much higher temperatures when exposed to a heat flux. Thus, staying with the surface temperature theory, the discrepancy between vertical heat of combustion results for POM, PMMA, PP, and HDPE compared to FRP, PBT, ABS, and HIPS can possibly be explained by the higher surface temperatures present during tests involving the latter group.

5.5. CO & CO_2 MEASUREMENTS

CO and CO_2 production during material burning can give an insight into the efficiency of the combustion process. Combustion efficiency can be impacted by several factors. For example, chemical makeup of the material, sample orientation, ambient oxygen concentration, ambient temperature, or external heat flux are all factors that can individually or simultaneously affect the efficiency of the combustion process. One result of inefficient combustion is increased CO production. Therefore, CO and CO_2 concentrations, in percent by volume, were measured during heat of combustion tests to determine if there was a noticeable trend in production of these two gases between different sample orientations that matched the trend seen in heat of combustion results.

CO and CO_2 concentrations were averaged over the same portion of the test that heat of combustion measurements were taken from. Literature values of CO production for a given material are often reported as a mass fraction of CO in the carbon oxides

(CO_x) of combustion where $CO_x = CO + CO_2$. To convert from percent by volume to CO/CO_x by mass, the individual concentrations of CO and CO_2 were first adjusted to account for CO and CO_2 present in ambient conditions and then multiplied by their respective molecular weights. The percentages have now been converted to grams of CO and CO_2 per mole of air. When plugged into the equation for CO/CO_x the mol of air is cancelled out, leaving a mass fraction of CO with respect to the total amount of carbon oxides produced during combustion. The results of the CO and CO_2 measurements are shown for each material and orientation in Table 9 along with literature values.

Table 9. CO/CO_x, expressed in %, for all four orientations and literature values where applicable.

Material	Horizontal no q_e"	Horizontal + q_e"		Vertical no q_e"	Vertical + q_e"
		This Study	Literature [34]		
POM	---	0.3	0.1	1.5	1.0
FRP	---	2.4	---	2.9	3.8
PBT	---	2.1	---	2.4	---
PMMA (ext.)	---	0.7	0.4	2.1	0.6
PMMA (cast)	0.7	0.7	0.4	2.1	0.7
ABS	---	3.2	3.0	3.1	3.7
HIPS	---	3.3	2.8	3.1	3.0
PP	1.1	1.4	1.1	2.3	1.2
HDPE	0.9	1.0	0.9	2.2	1.2

The results from this study agree reasonably well with those found in literature, which are from horizontal, over-ventilated cone calorimeter tests under 50 kW/m^2 of external heat flux [34]. Comparing the CO/CO_x values to heat of combustion values for the different orientations, there does appear to be a relationship between the production of CO and the heat of combustion differences between orientations. In other words, CO production increases when the heat of combustion decreases for a specific material. To

visualize this trend, a plot is created with the difference in heat of combustion between vertical and any other orientation normalized by the material's MCC value on the x-axis and the difference between CO/CO_x values on the y-axis. This plot, depicted in Figure 30, should show whether an increasing difference in heat of combustion between the vertical orientation and any of the other orientations tested (horizontal or vertical with external heat flux or horizontal with no external heat flux) results in an increasing difference CO production.

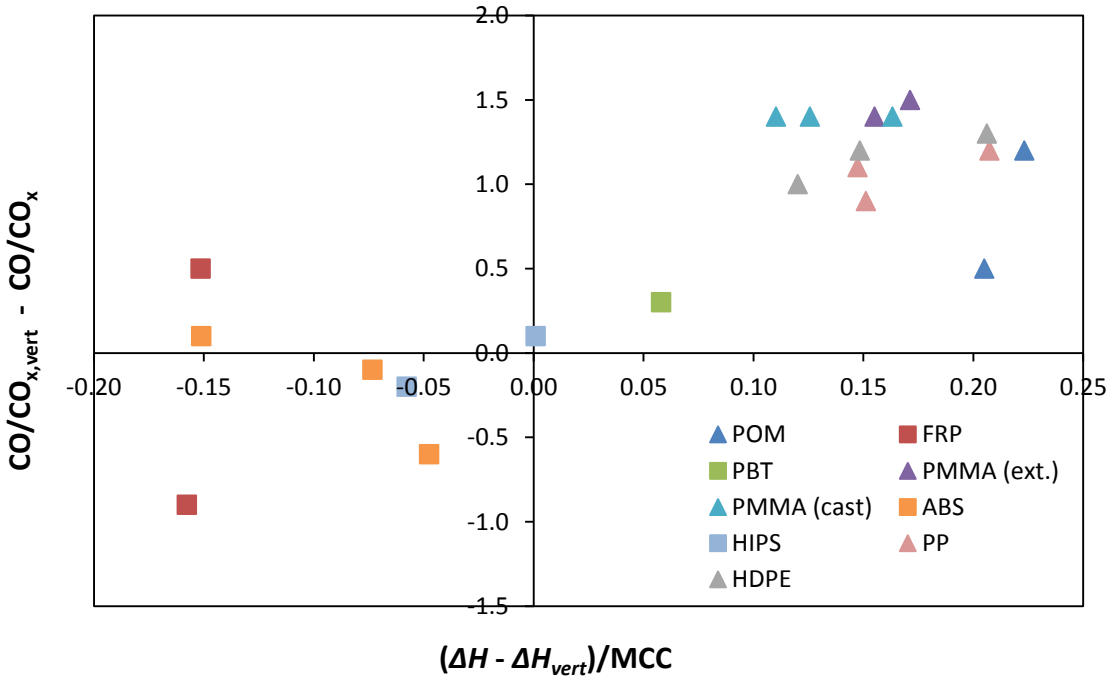

Figure 30. Shows relationship between the orientation that the heat of combustion was measured in and the CO production.

While subtle, Figure 30 does show a correlation between the amount of CO produced and the difference in heat of combustion for the same material in different orientations. It is also interesting to note that the trend continues into the negative region where the materials that exhibited higher heats of combustion in the vertical orientation with no external heat flux also produced lower amounts of CO in this orientation. This

plot also confirms that the drop in heat of combustion in the vertical orientation with no external heat flux for some materials is due at least in some part to inefficiency in the combustion process.

5.6. HEAT FLUX

A minimum of three heat flux tests at each sample height were performed for each material. Using the time at which the sample igniter is removed as the start time (t = 0 s), heat flux measurements were averaged at each time step and then smoothed using a five second moving average. As shown in Figure 31, this creates a plot with much less noise than the individual test measurements.

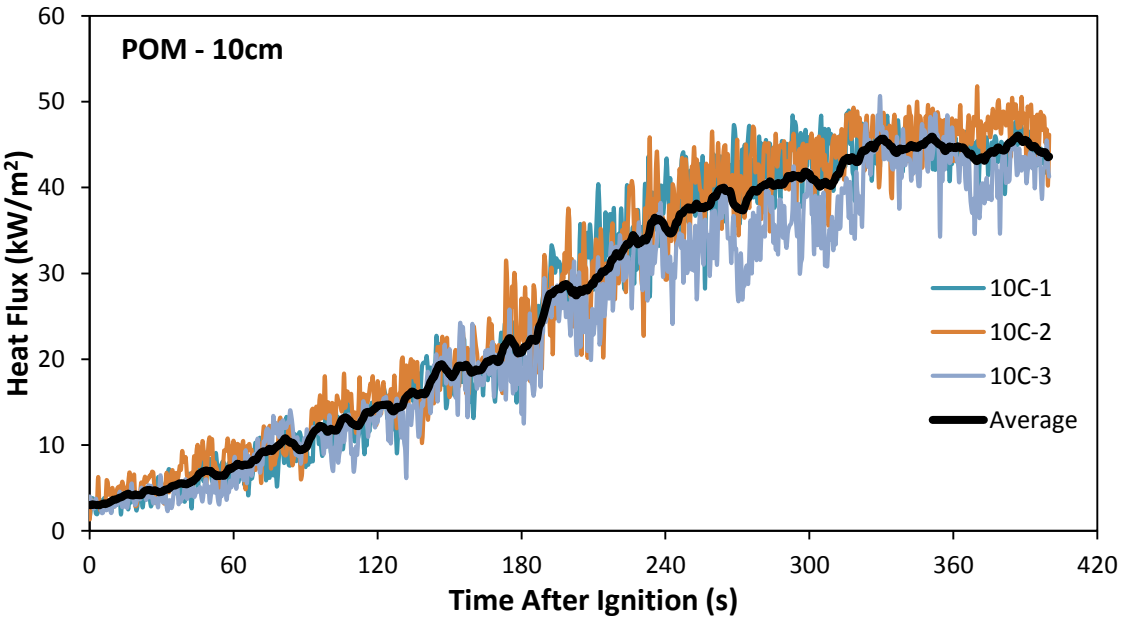

Figure 31. Representative plot of three 10 cm tall POM tests showing how averaged heat flux values have significantly reduced noise compared to individual test measurements.

This averaging was performed at each sample height and then a plot of the averaged heat flux measurements at each sample height was created for each material. This gives a time history of the heat flux profile on the surface of the sample. The heights

at which measurements were taken for each material were chosen based on how far the pyrolysis front spread up the surface of the material. For materials where the pyrolysis front did not spread significantly, the maximum sample height tested was 10 cm. Materials that exhibited a spreading pyrolysis front were tested at a maximum height of 15 cm. As described in section 4.3.3, some tests were performed with a shield to protect the heat flux gauge from deposits until a pre-specified time so that representative heat flux measurements could be collected without the interference of deposits. These shielded tests were only performed for HIPS and ABS, the two materials with the most significant accumulation of deposits. For other materials that developed a surface layer of deposits, such as PP, PBT, and FRP, shielded tests were not performed but for the purposes of comparing predicted flame heat flux values to measured values, only the period of time prior to the accumulation of deposits on the heat flux gauge is used. In the following charts, heat flux measurements for these materials are shown even after deposits begin accumulating on the heat flux gauge to show how these deposits impact the measurements.

Figure 32 shows the averaged heat flux time histories for PP at heights of 5, 7, 10, 12, and 15 cm. Sample heights of 10 cm and greater did not reach a steady-state heat flux before the base of the sample burned out and epoxy began contributing to the flame around 400 seconds after ignition.

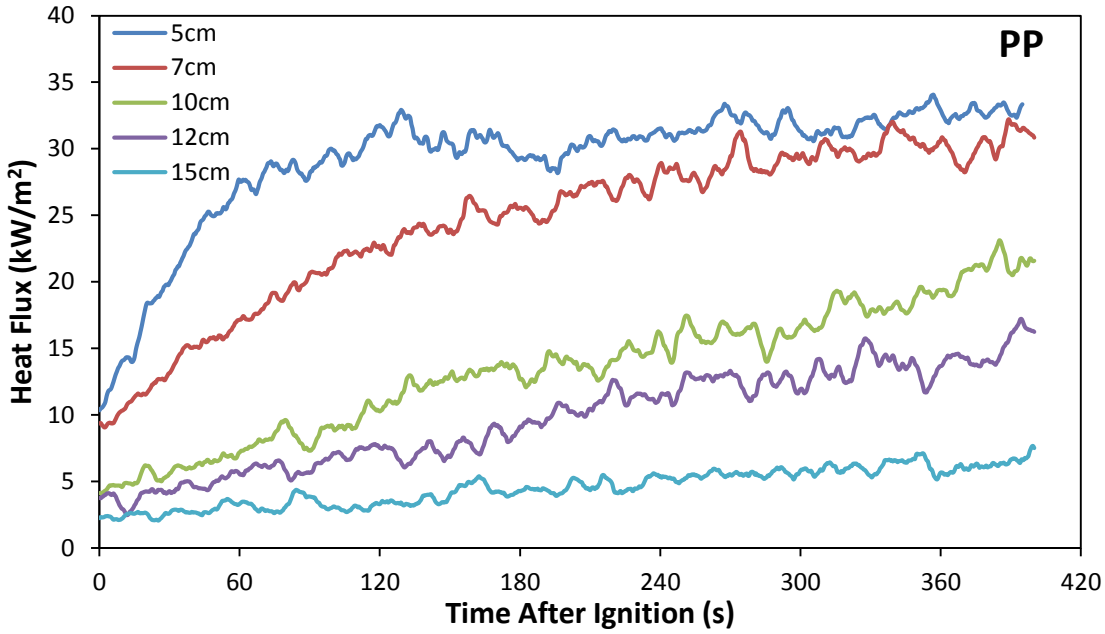

Figure 32. Averaged heat flux time histories for polypropylene at heights of 5, 7, 10, 12, and 15 cm.

A thin layer of deposits adheres to the surface of the heat flux gauge during PP tests, as shown in

Figure 33. Depending on the height of the sample, the surface layer would begin developing on the gauge's surface at different times during the test. For 5 cm samples, the first, very thin, matte surface layer reaches the gauge between 30 – 40 seconds after sample ignition and the second, denser, glossy layer reaches the gauge 120 seconds after ignition. 15 cm samples, on the other hand, do not start accumulating thin deposits onto the surface of the gauge until 240 seconds after ignition and the glossy surface layer does not reach the gauge before burn out at the base of the sample begins. Because of how thin this layer of deposits is, it is unlikely that it impacts the heat flux measurements. This is emphasized by the way the heat flux measurements do not decrease as shown in Figure 32.

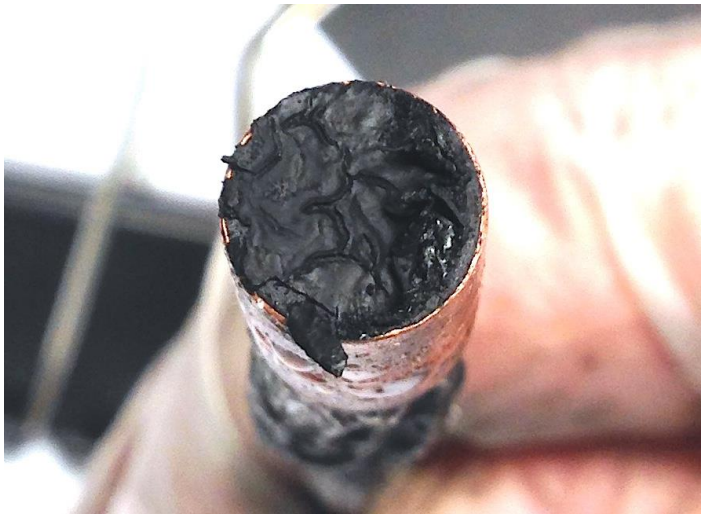

Figure 33. Picture showing the thin surface layer that develops on the surface of the heat flux gauge after a polypropylene test.

Figure 34 shows the averaged heat flux time histories for POM at heights of 5, 7.5, 10, and 12.5 cm. Heat flux measurements were stopped when significant melt flow at the base of the sample would cause the entire 2 – 3 cm at the bottom to flow out of the sample holder. The steady-state heat flux decreases slightly with increasing sample height. This effect will be discussed in further detail in the analysis section. Very little residue would build up on the surface of the heat flux gauge during POM tests.

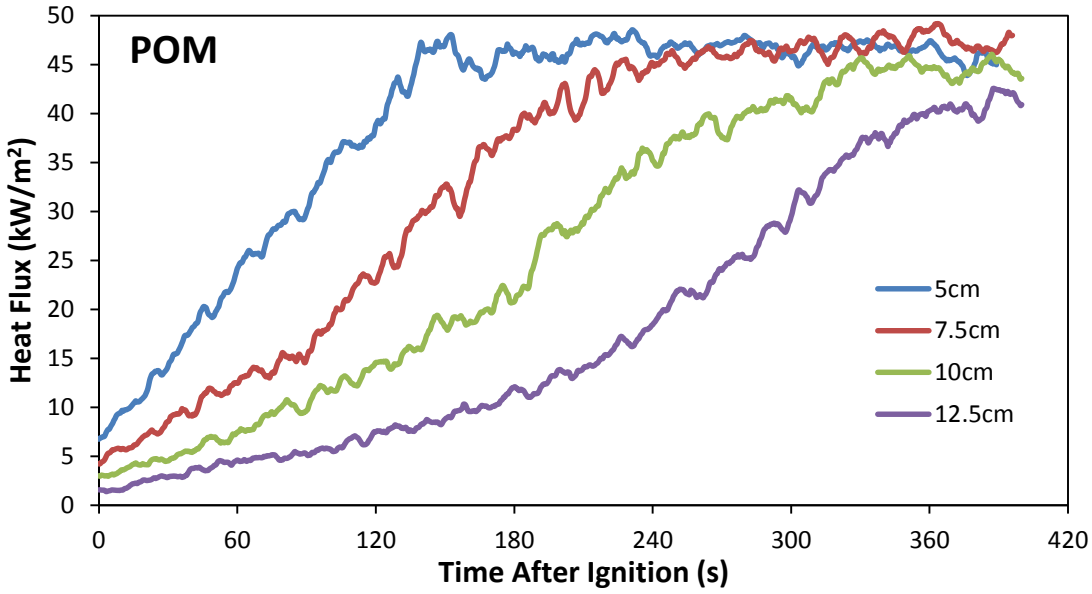

Figure 34. Averaged heat flux time histories for polyoxymethylene at heights of 5, 7.5, 10, and 12.5 cm.

Figure 35 shows the plot of averaged heat flux time histories for HIPS at heights of 5, 7.5, and 10 cm. Due to the significant accumulation of deposits onto the surface, heat flux measurements are impacted in two ways. First, deposits begin accumulating on the gauge almost immediately after ignition for 5 cm samples and less than 30 seconds after ignition for 10 cm samples. This low-density accumulation get thicker throughout the test and makes an efficient thermal barrier between the gauge and the flame and/or thermal boundary layer. Figure 36 shows the build-up of the surface layer on the heat flux gauge at the end of a 5 cm test. Second, the deposits that accumulate on the surface of the sample impede heat transfer from the flame to the gauge by limiting flame spread and interfering with the flame structure. Heat flux measurements from tests where the gauge is shielded from deposits for a specified time are included with the averaged heat flux time histories shown in Figure 35. To get a representative value from these tests, the heat flux measurements were averaged for five seconds just after the shield was removed. The

error bars represent two standard deviations of the mean over the five second measurement period.

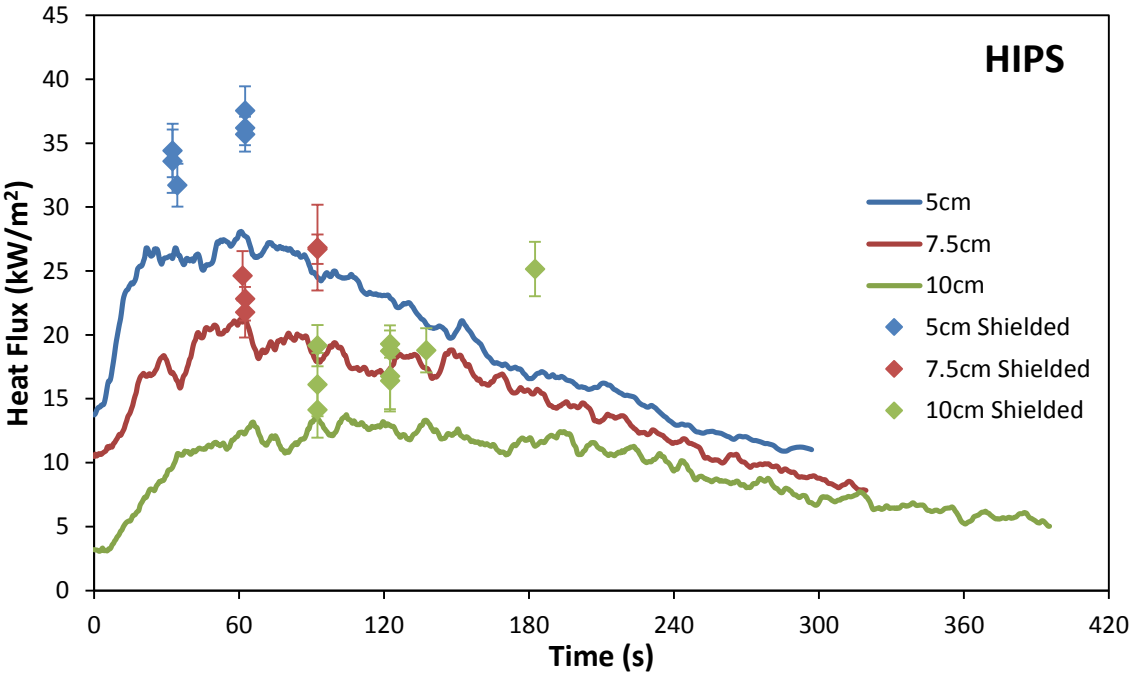

Figure 35. Averaged heat flux time histories for high impact polystyrene at heights of 5, 7.5, and 10 cm. Also included are measurements from tests where the heat flux gauge is shielded from deposits until a pre-specified time.

Figure 36. Picture showing the layer of deposits accumulated on the surface of the heat flux gauge after a 5 cm HIPS test.

Averaged heat flux measurements at heights of 5 cm, 7.5 cm, and 10 cm for FRP are shown in Figure 37. Surface deposits began accumulating on the 5 cm samples within 30 seconds of ignition and within 180 – 240 seconds of ignition on the 10 cm samples. By the end of a test, there is a considerable layer of deposits covering the entire surface of the gauge, as shown in Figure 38.

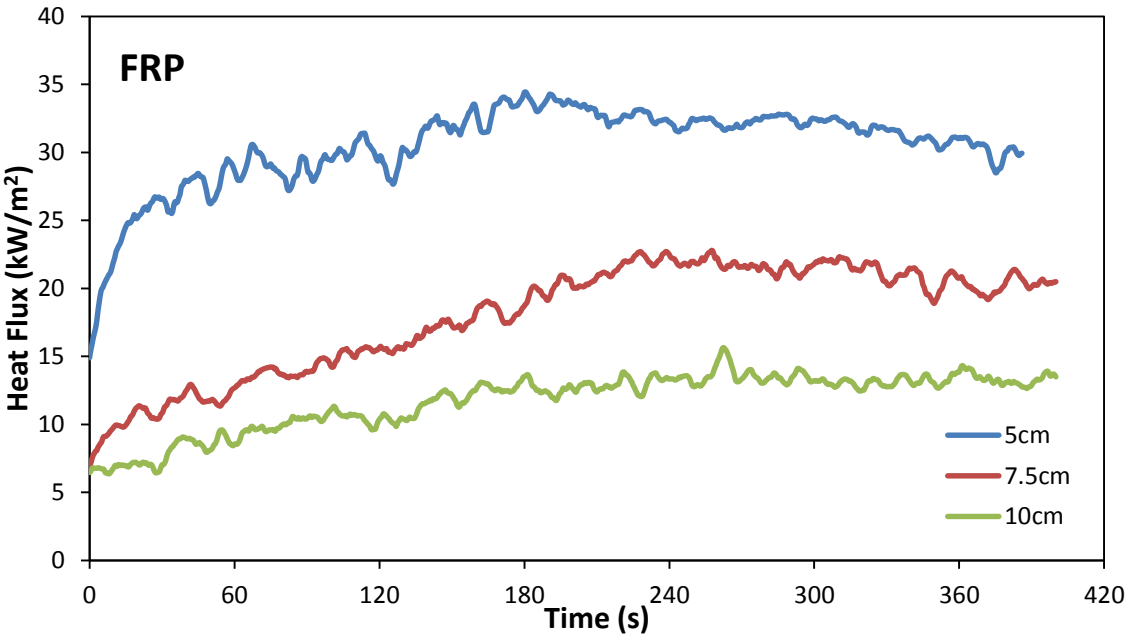

Figure 37. Averaged heat flux time histories for 5, 7.5, and 10 cm samples of fiberglass reinforced polyester resin.

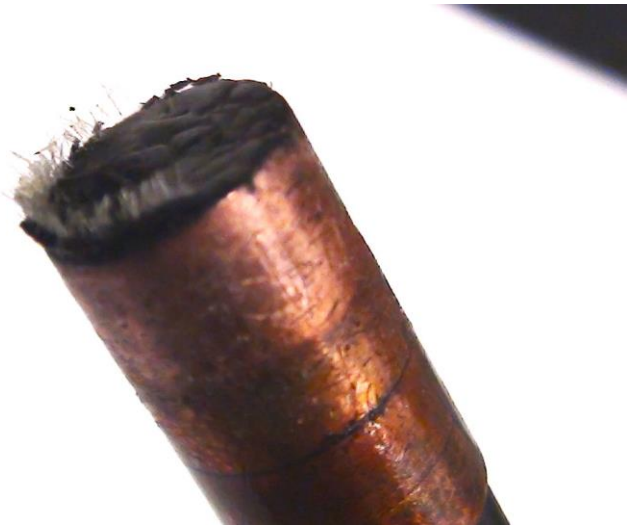

Figure 38. Surface deposits that develop on the heat flux gauge during a fiberglass reinforced polyester resin test.

Figure 39 shows the averaged heat flux measurements from 4.5 cm, 9 cm, and 14.5 cm samples of PBT. Surface deposits covered the gauge within 30 seconds on 4.5 cm tests and within 180 seconds on 14.5 cm tests. Unlike other materials, deposits accumulated onto the surface of the gauge uniformly and built up a thick layer by the end of the test, measuring up to 0.9 mm in thickness. The slowly increasing and smooth heat flux measurements after the initial rise are likely due to the movement of the base of the flame up the sample and the deposits on the gauge acting to reduce the noise of the measurements. Frequently, when removing the heat flux gauge from its position after a test, the surface layer would be left intact within the hole in the insulation. Figure 40 shows the deposits on the gauge that are exposed when the top surface layer remains in place with the sample as well as the top surface layer being held by a pair of calipers.

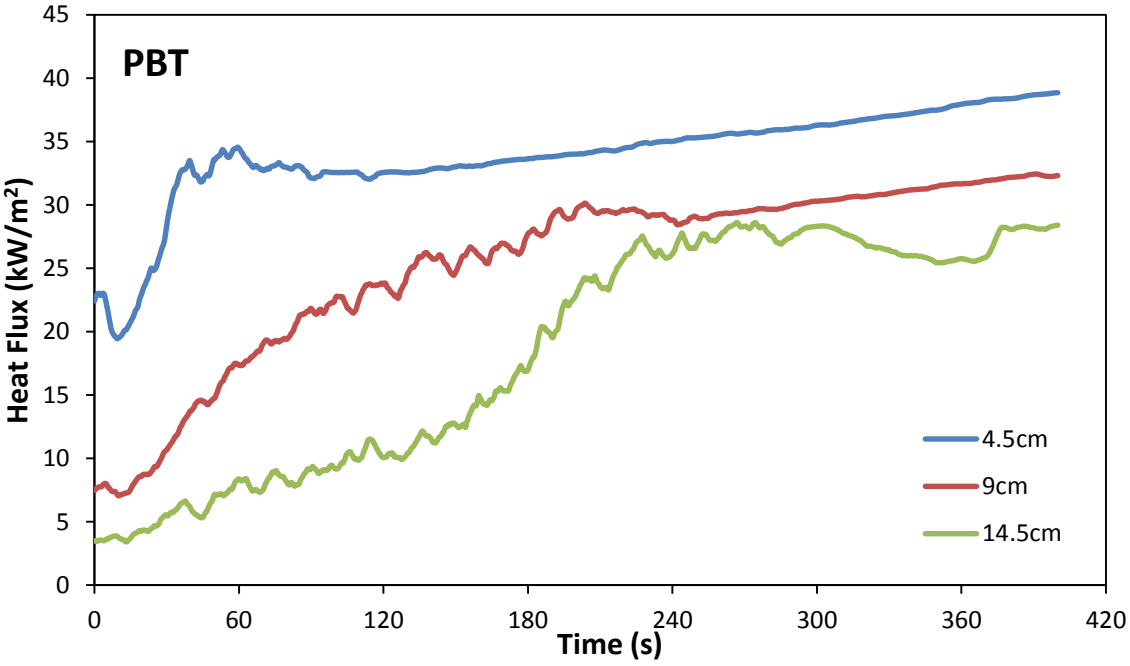

Figure 39. Averaged heat flux time histories for 4.5, 9, and 14.5 cm samples of glass filled polybutylene terephthalate.

Figure 40. Deposits that remain on surface of heat flux gauge (left) after top surface layer, measuring up to 0.9 mm thick (right), comes off after a test on polybutylene terephthalate.

Averaged heat flux time histories for ABS at heights of 5, 7, 9, 11, and 15 cm are shown in Figure 41. Despite the addition of 10 kW/m^2 of radiant heat flux, deposits still accumulated on the surface of the heat flux gauge. The effect of this is noticeable in the heat flux measurements as shown by the decay in heat flux profiles in Figure 41. At the point when the heat flux values began to decay, the gauge is directly under the flame so the heat flux should either still be increasing or holding constant as shown in heat flux time histories from other materials that produce very little to no soot such as POM (Figure 34). Heat flux measurements from shielded tests are displayed in Figure 41 as well with error bars representation two standard deviations of the mean for the five second measurement period. Figure 42 shows the surface layer build-up on the gauge after an ABS test.

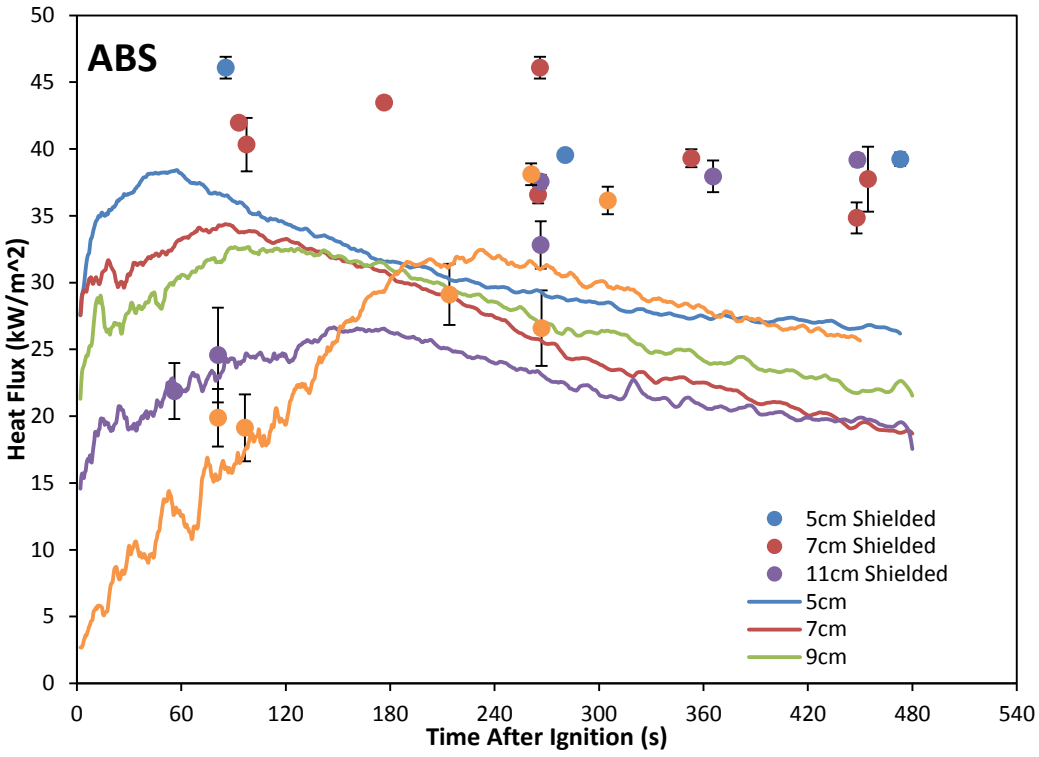

Figure 41. Averaged heat flux time histories for acrylonitrile butadiene styrene at heights of 5, 7, 9, 11, and 15 cm.

Figure 42. The surface layer that develops on the heat flux gauge during an ABS test, as shown in this picture, has a clear effect on the heat flux measured by the gauge.

An averaged heat flux time history for cast PMMA at a height of 15 cm is shown in Figure 43.

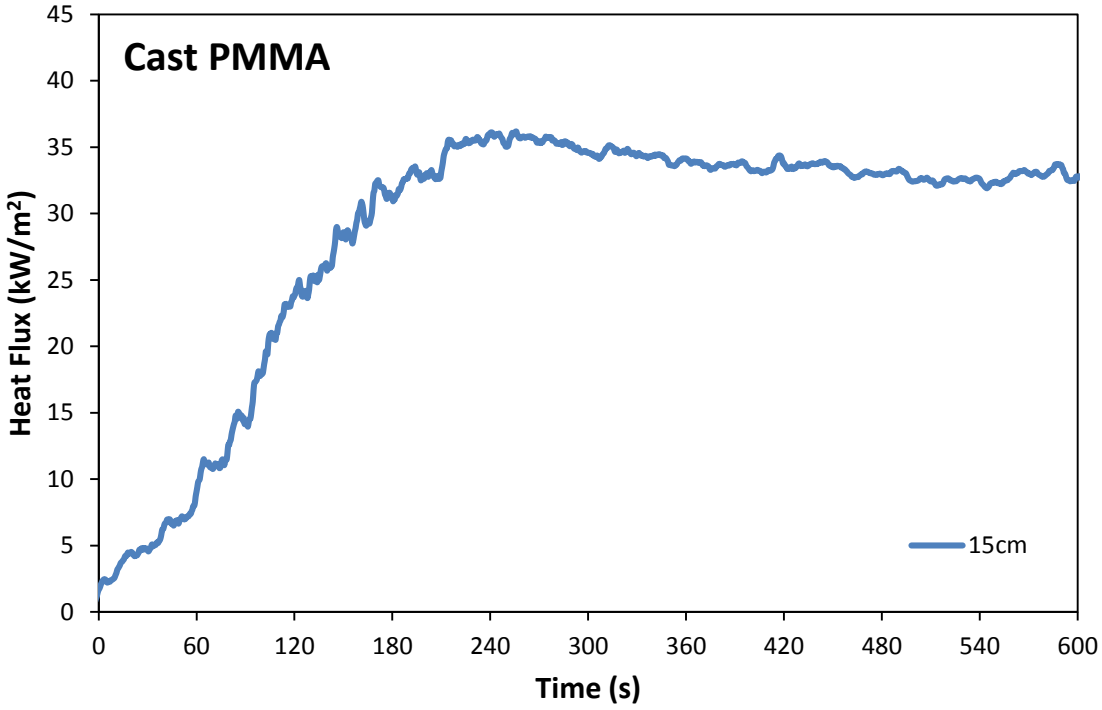

Figure 43. Averaged heat flux time history for cast polymethyl methacrylate at a height of 15 cm.

6. ANALYSIS

6.1. INPUT PARAMETERS

There are two sets of parameters that are used in the generalized flame heat flux model. The first set are the input parameters. These are measurable quantities that are based on the chemical and/or physical properties of the material. The input parameters are used to calculate the second set of parameters which are referred to as the scaling parameters. The scaling parameters are used within the flame heat flux prediction equations presented in Section 2.2 and 6.2. These parameters and how they are calculated

will be discussed in detail in the following section (6.2). The two sets of parameters along with the flame heat flux prediction equations are the basis of the generalized flame heat flux model presented in this study.

The PMMA model was developed to use one input parameter, a material's width-normalized mass loss rate, to predict flame heat flux. However, in its current form, the PMMA model does not account for the amount of energy produced by the material when it burns. The heat of combustion is a direct measure of the amount of energy produced by a material when it burns, thus it is an ideal input parameter for generalizing the PMMA model so that it can apply to any material with a measurable heat of combustion. It should be emphasized that all heat of combustion values used and referred to in this study are in units of energy (kJ) per unit mass (g) of *volatilized material*.

The problem then becomes determining which heat of combustion value to use as an input parameter. The two principal heat of combustion values commonly referred to in literature are the complete heat of combustion, ΔH_T, and the effective heat of combustion, ΔH_{eff}. Both values are logical choices to use as input parameters. ΔH_T is a measure of the inherent chemical energy within a material and represents the energy produced by the material when it is burning with 100% efficiency ($\chi_e = 1$). This value is promising because there could be portions of the flame, especially for the small, laminar to transient laminar flames studied in this work, where χ_e is close to 1. There are multiple methods of measuring ΔH_T but for this report, values were obtained from MCC tests as described in Sectioin 4.3.2. ΔH_{eff} represents the amount of energy produced when a material burns in conditions that resemble those found in an actual fire [31]. The fact that ΔH_{eff} captures some of the combustion inefficiencies that exist during normal fire conditions (i.e. soot,

CO, etc.) could make it a favorable candidate because, as shown in Section 5.1, these inefficiencies do exist during upward flame spread. Values for ΔH_{eff} are taken from the $\Delta H_{eff,H}$ results measured as part of this study. ΔH_{vert} could also work well considering it was measured in the same configuration that flame heat flux measurements were performed in so it might better represent the conditions specific to small-scale upward flame spread.

Lastly, since the heat flux measured by the gauge is primarily convective in these small-scale tests, accounting for the relative effect of radiation losses from the flame may lead to a more accurate prediction of flame heat flux. To get this adjusted value, a material's radiative fraction (χ_r), the fraction of energy from a fire that is lost to radiation, can be used. For use in the generalized model, the effective heat of combustion is multiplied by $(1 - \chi_r)$ to get a value that represents the convective portion of the heat of combustion.

To get values of χ_r for each material, the long-standing work of Tewarson [31] [47] [48] and a more recent study by Quintiere et al. [49] were referenced. Additionally, Tewarson developed a correlation that calculates χ_r based on the material's χ_e [50]. Since there are variations for reported χ_r values between Tewarson's three works and the work by Quintiere et al., the values are averaged to obtain a representative χ_r for each material. It is important to clarify that Tewarson defines the radiative fraction as $\chi_r = \frac{\Delta H_r}{\Delta H_T}$ where ΔH_r is the radiant portion of the heat of combustion whereas Quintiere et al. use $\chi_r = \frac{\Delta H_r}{\Delta H_{eff}}$. Since the radiant fraction is used in this study to adjust $\Delta H_{eff,H}$, the definition of χ_r used by Quintiere et al. is used here. In order to convert Tewarson's values to represent the same quantity, they are divided by χ_e using the values of χ_e measured in this study and

presented in Table 6. A χ_r for ABS was not reported by Tewarson so his χ_e correlation is used and the resulting value is averaged with the χ_r reported by Quintiere et al. In the same manner, FRP and PBT do not have their χ_r listed by either of the sources so the χ_e correlation has been used. Table 10 summarizes the χ_r values to be used for this study.

Table 10. Summary of how radiant fraction values were obtained for this study.

	Tewarson				Quintiere et al. [49]	Average χ_r
Material	[48]	[47]	[31]	**χ_e Correlation** [50]		
POM	0.21	0.16	0.20		0.22	**0.20**
PMMA	0.34	0.34	0.30		0.33	**0.33**
PP	0.42	0.34	0.40		0.57	**0.43**
HIPS/PS	0.43	0.39	0.55		0.49	**0.46**
ABS				0.51	0.41	**0.46**
PBT				0.31		**0.31**
FRP				0.35		**0.35**

The four heat of combustion values described above are presented in Table 11 for each material. The values for extruded PMMA are included as a reference because they are used to calculate the scaling parameters. These values, along with the coefficients for the fitted $\frac{dm'}{dt}$ polynomials, presented earlier in Table 4, make up the input parameters used to generalize the flame heat flux model.

Table 11. Heat of combustion [kJ/g] input parameters for each material.

Material	ΔH_T	$\Delta H_{eff,H}$	ΔH_{vert}	$(1-\chi_r)\Delta H_{eff,H}$
POM	14.0	14.9	11.8	11.9
FRP	22.7	20.5	23.9	13.3
PBT	23.2	21.6	14.9	20.2
PMMA (ext.)	24.5	23.8	20.0	15.9
PMMA (cast)	24.5	24.4	21.3	16.3
ABS	36.5	28.4	25.5	15.3
HIPS	39.2	27.8	30.1	15.0
PP	41.0	37.9	21.6	31.7

6.2. SCALING PARAMETERS

With all of the necessary input parameters and experimental flame heat flux values measured for each material, a straightforward scaling technique can be employed to predict the flame heat flux and compare the prediction to experimental results for each material and each set of input parameters.

The heat of combustion is used in two ways to calculate the scaling parameters. The first scaling parameter is a simple ratio of the heat of combustion input parameter for the material of interest to the same input parameter for extruded PMMA. This scaling parameter, which is given the symbol, φ, is represented by the following expression,

$$\varphi_{i,x} = \frac{\Delta H_x^i}{\Delta H_x^{PMMA(ext.)}} \tag{11}$$

where the superscript *i* refers to the material of interest and the subscript *x* refers to the type of heat of combustion value to be used (i.e. *T*, *eff*,*H*, etc.). This scaling parameter accounts for the heat release of the material of interest relative to that of extruded PMMA and is used to scale the width-normalized mass loss rate in the calculation of flame height, y_f, as shown in Equation (12).

$$y_{f,i} = a\left(\varphi_{i,x} \times \frac{dm_i{}'}{dt}\right)^b + c \tag{12}$$

The second scaling parameter is the adiabatic flame temperature, $T_{fl,ad}$. To calculate $T_{fl,ad}$ using the heat of combustion, the simplified assumption that all the energy from stoichiometric combustion of the material of interest in air goes into heating the products from ambient temperature, T_∞, up to $T_{fl,ad}$ and the only products are CO_2, H_2O, and N_2. The equation representing this assumption is shown below:

$$\Delta H_x^i = \sum_{j=1}^{3} n_j MW_j \int_{T_\infty}^{T_{fl,ad,x}} c_{p,j} dT \tag{13}$$

where the units of ΔH are in kJ per gram of volatilized mass, the subscript j refers to the products CO_2, H_2O, and N_2, n is the number of moles of each product assuming a stoichiometric fuel to air ratio, MW is the molecular weight, and c_p is the heat capacity.

The temperature dependent heat capacities for each of the products are estimated using the polynomial relationships that have been developed for the NIST-JANAF Thermochemical Tables and made available on the NIST Chemistry Webbook [51]. Plugging the polynomial equations in for the heat capacities in Equation (13) and integrating allows $T_{fl,ad}$ to be solved for numerically given a material's heat of combustion. Since there are four ΔH_x values for each material, there are four corresponding $T_{fl,ad,x}$ values as well.

The predicted flame heat flux to the gauge, q''_{HFg}, can then be calculated using a modified form of the prediction equation used in the PMMA model (Equation (5)). Instead of using a steady-state heat flux value, $T_{fl,ad}$ is used along with the assumption that q''_{HFg} is primarily convective and can be modeled accurately with the convective heat transfer expression given in Equation (14).

$$q''_{HFg} = h(T^* - T_{HFg}) \tag{14}$$

where h is the heat transfer coefficient, T_{HFg} = 291 K is the water temperature in the gauge, and T^* is the effective boundary layer temperature which depends on the height above the base of the flame, y. For heights under the flame ($y \leq y_f$), T^* is assumed to equal $T_{fl,ad}$ for $y \leq 5$ cm or an adjusted value of $T_{fl,ad}$ for $y > 5$ cm and is represented by the piecewise linear relationship shown below,

$$\text{for } y \le y_f \qquad T^* = \begin{cases} T_{fl,ad} & ; y \le 5 \text{ cm} \\ \left(\frac{34}{40}\right) T_{fl,ad} & ; y > 5 \text{ cm} \end{cases} \tag{15}$$

The ratio of $\frac{34}{40}$ comes from the ratio of steady-state flame heat flux measurements obtained in the development of the PMMA model for heights above and below y = 5 cm as shown in Equation (2). For heights in the flickering region of the flame and above ($y < y_f$), T^* is represented by an exponential decay function shown in Equation (16).

$$\text{for } y > y_f \qquad T^* = \begin{pmatrix} T_{fl,ad} & ; y \le 5 \text{ cm} \\ \left(\frac{34}{40}\right) T_{fl,ad} & ; y > 5 \text{ cm} \end{pmatrix} \times \alpha\left(e^{-\ln(\alpha)\times(y^*)^2}\right) \tag{16}$$

A plot of $T^*/ T_{fl,ad}$ with respect to y is helpful to visualize these equations and is presented in Figure 44 for extruded PMMA at heights of $y \le y_f$ and $y > y_f$.

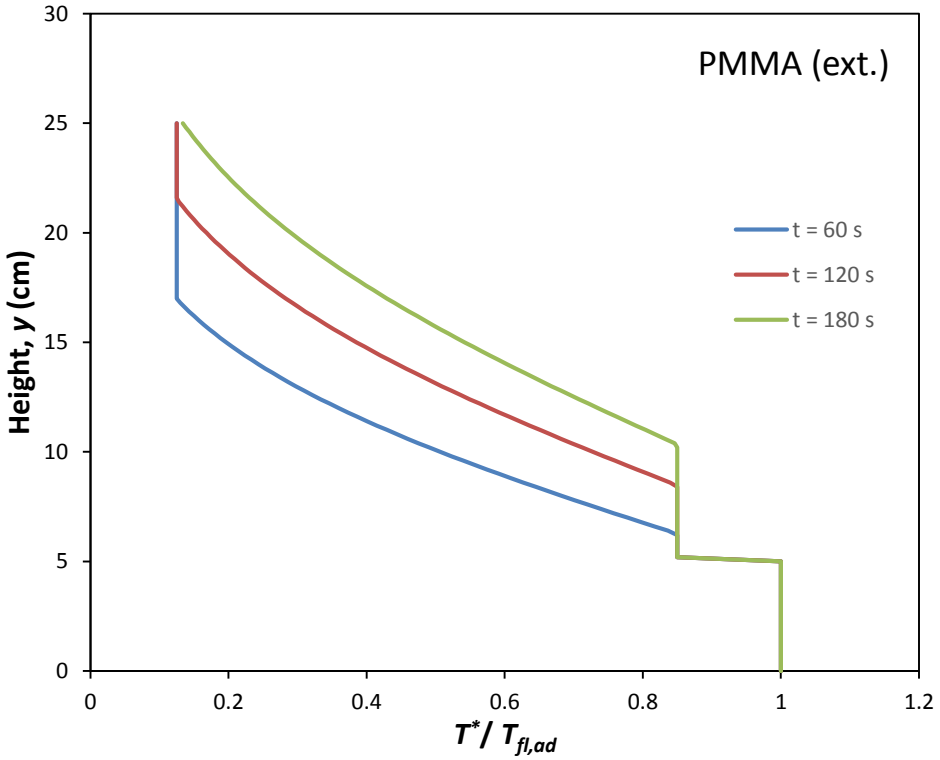

Figure 44. Shows how the effective boundary layer temperature, T^*, depends on y at t = 60, 120, and 180 s after ignition.

The final scaling parameter is the heat transfer coefficient for each $T_{fl,ad,x}$. This is calculated by simply plugging the $T_{fl,ad,x}$ for extruded PMMA in Equation (14) and solving for h_x using the measured peak flame heat flux to the gauge from the PMMA model, $q''_{HFg,peak}$ = 40 kW/m^2, as shown below:

$$h_x = \frac{q''_{HFg,peak}}{\left(T_{fl,ad,x} - T_{HFg}\right)} \tag{17}$$

It is important to note that the flame temperature used here is not necessarily representative of the actual flame temperature, especially in the case where the radiant fraction is used, but, rather, it is an effective flame temperature that is used to account for the amount of heat produced by the material in comparison to PMMA. In the same way, h_x is an effective heat transfer coefficient that captures both the dominant convective and minor radiative heat transfer to the surface. A full table of the calculated φ and $T_{fl,ad}$ for each material and heat of combustion value as well as the four h_x values are shown in Table 12.

Table 12. Scaling parameters, φ and $T_{fl,ad}$, for each material and heat transfer coefficients for each heat of combustion value.

	ΔH_T		$\Delta H_{eff,H}$		ΔH_{vert}		$(1-\chi_r)\Delta H_{eff,H}$	
h (W/(m-K))	19.6		20.2		23.6		28.8	
Material	φ	$T_{fl,ad}$ (K)	φ	$T_{fl,ad}$ (K)	φ	$T_{fl,ad}$ (K)	φ	$T_{fl,ad}$ (K)
POM	0.57	2180	0.63	2288	0.59	1913	0.75	1930
FRP	0.93	2317	0.86	2140	1.20	2413	0.84	1549
PBT	0.95	2294	0.91	2169	1.01	2059	0.93	1638
PMMA (ext.)	1.00	2327	1.00	2275	1.00	1989	1.00	1678
PMMA (cast)	1.00	2327	1.03	2320	1.03	2087	1.07	1709
ABS	1.49	2396	1.19	1970	1.28	1816	0.96	1257
HIPS	1.60	2457	1.17	1881	1.51	1998	0.94	1205
PP	1.67	2294	1.59	2158	1.59	1881	1.35	1420

6.3. GENERALIZED MODEL PREDICTION RESULTS

With all of the input and scaling parameters now defined, the predicted q''_{HFg} time history can be calculated and compared to the measured heat flux time histories from this study. The following step-by-step procedure outlines the process for calculating the predicted q''_{HFg} for a specific material, *i*, at a height of *y*.

1) Calculate dm'/dt at each time step using Equation (10) and polynomial coefficients from Table 4
2) If the base of the flame moves, calculate y_b at each time step using base of flame equation(s) from Table 5
3) Obtain scaling parameters, φ and $T_{fl,ad}$, and heat transfer coefficient from Table 12 for material *i*
4) Calculate y_f at each time step using Equation (12)
5) Calculate y^* at each time step using Equation (4)
6) Calculate q''_{HFg} at each time step using Equations (14 – 16)

Using this procedure, the predicted q''_{HFg} using the ΔH_T input parameter is calculated for each material and compared at each of the heights that q''_{HFg} was measured. The plots showing these comparisons are given in Figure 46 – Figure 51 below. In the plots, measured data points are only shown every 1 – 2.5 seconds depending on the length of the prediction period.

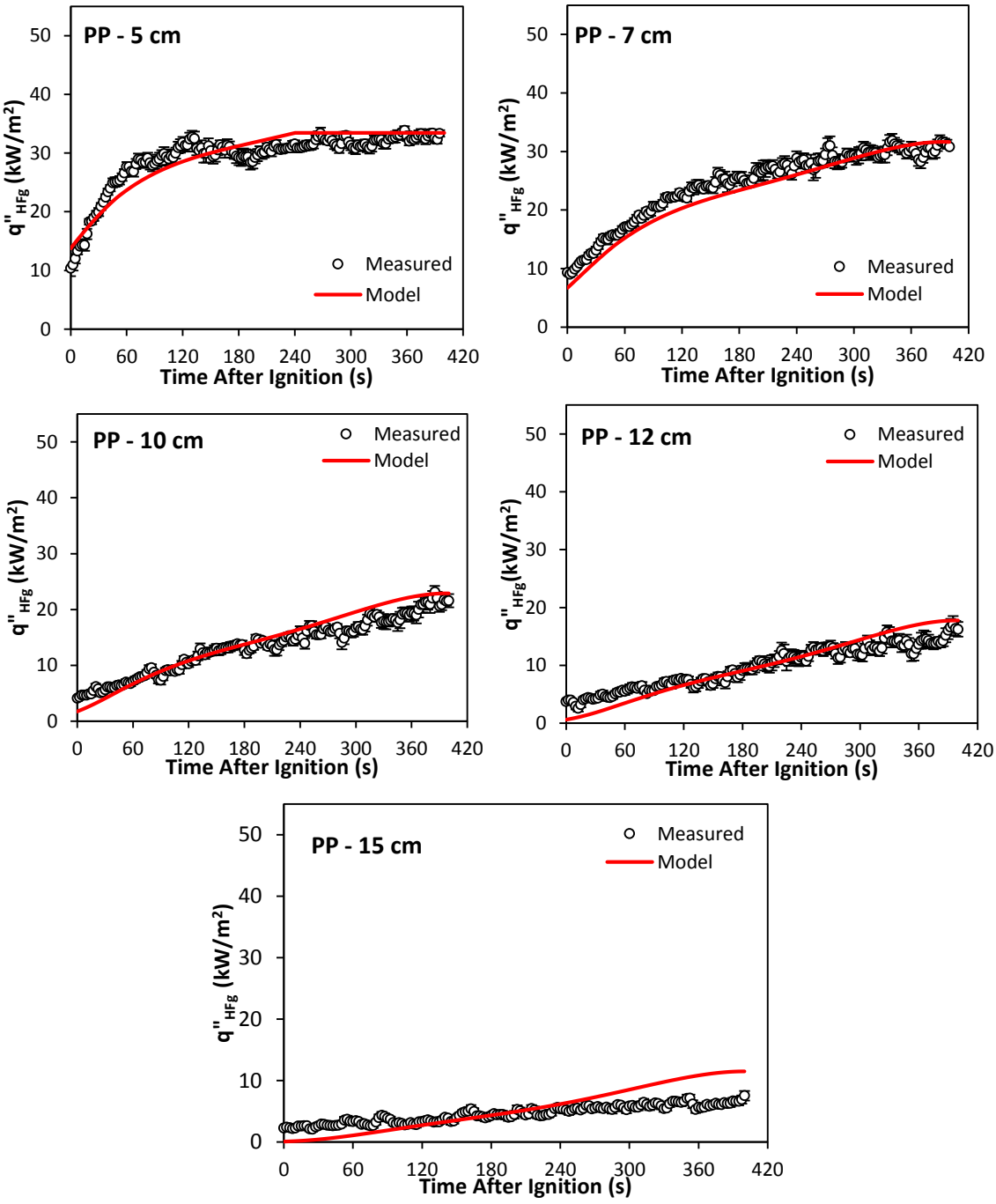

Figure 45. Measured and predicted $\boldsymbol{q''_{HFg}}$ using ΔH_T as an input parameter for PP at 5, 7, 10, 12, and 15 cm

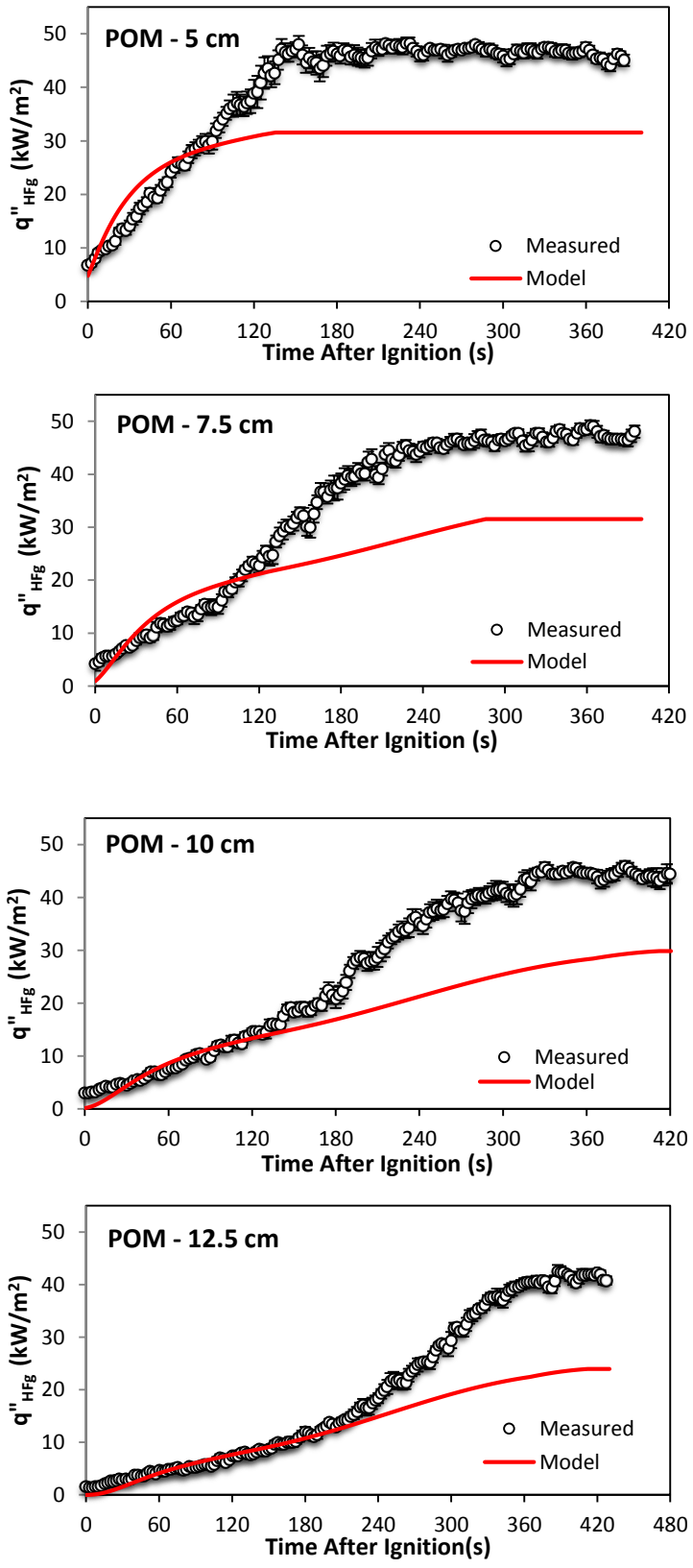

Figure 46. Measured and predicted q''_{HFg} using ΔH_T for POM at 5, 7.5, 10, and 12.5 cm.

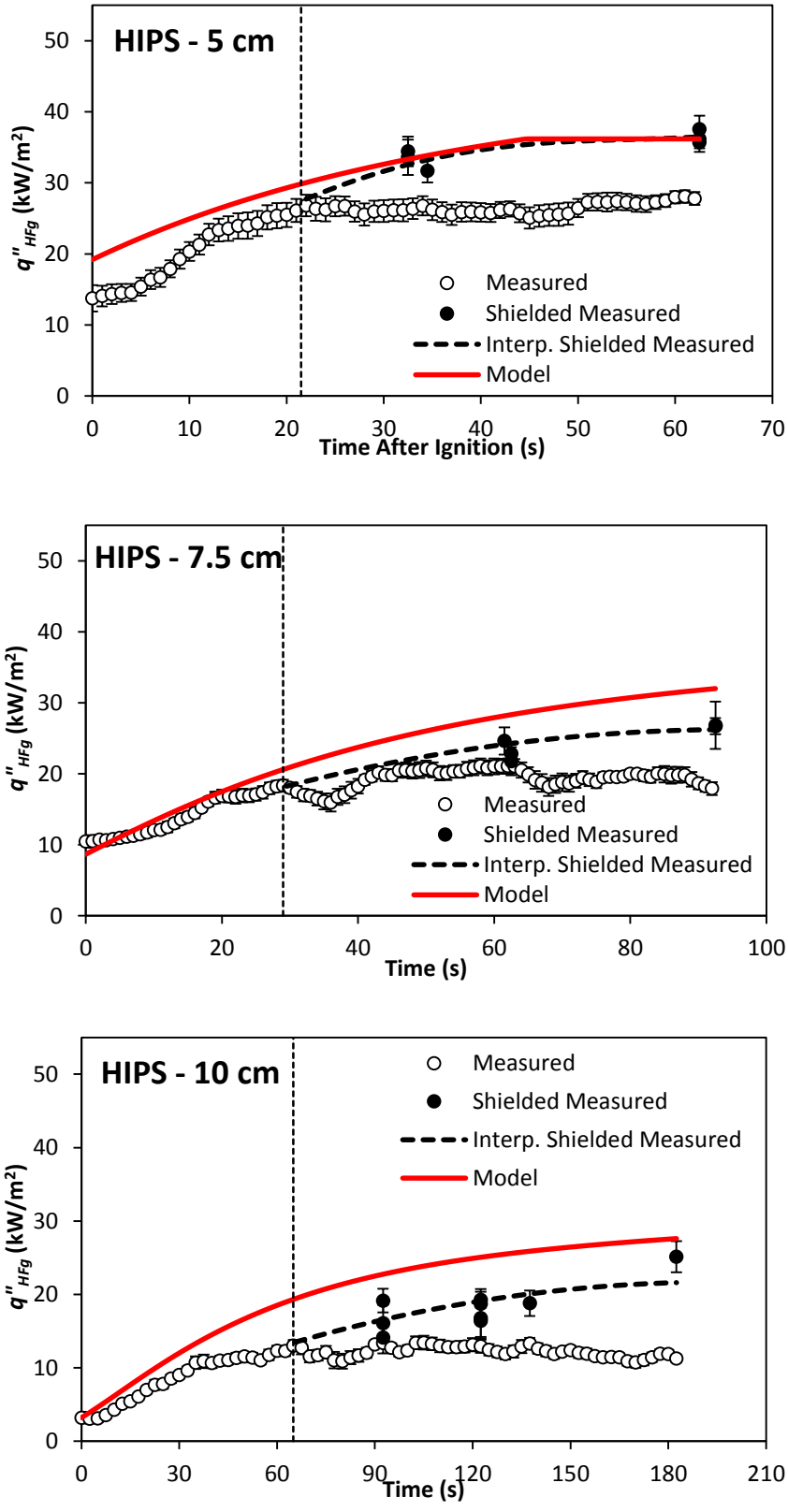

Figure 47. Measured and predicted q''_{HFg} using ΔH_T for HIPS at 5, 7.5, and 10 cm

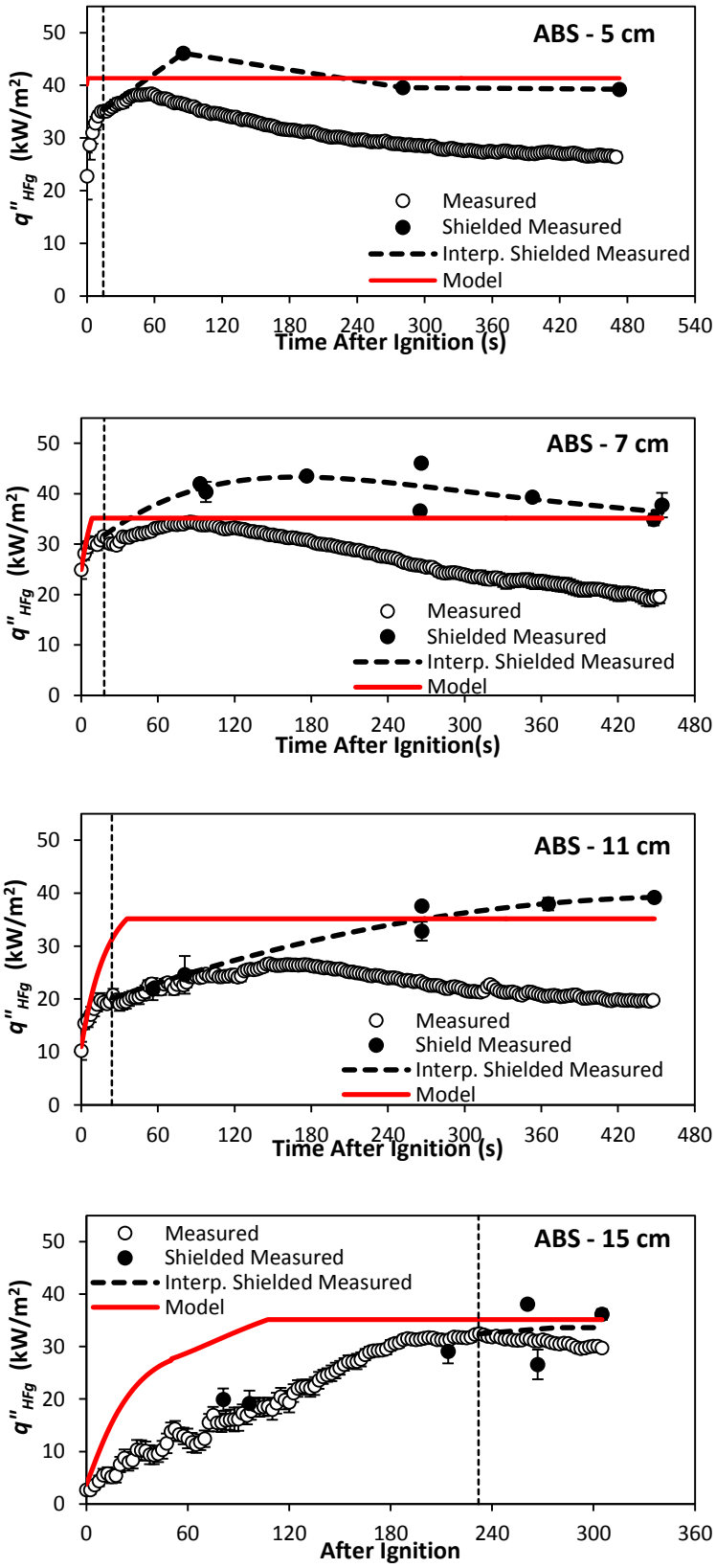

Figure 48. Measured and predicted $\boldsymbol{q''_{HFg}}$ using ΔH_T for ABS at 5, 7, 11, and 15 cm

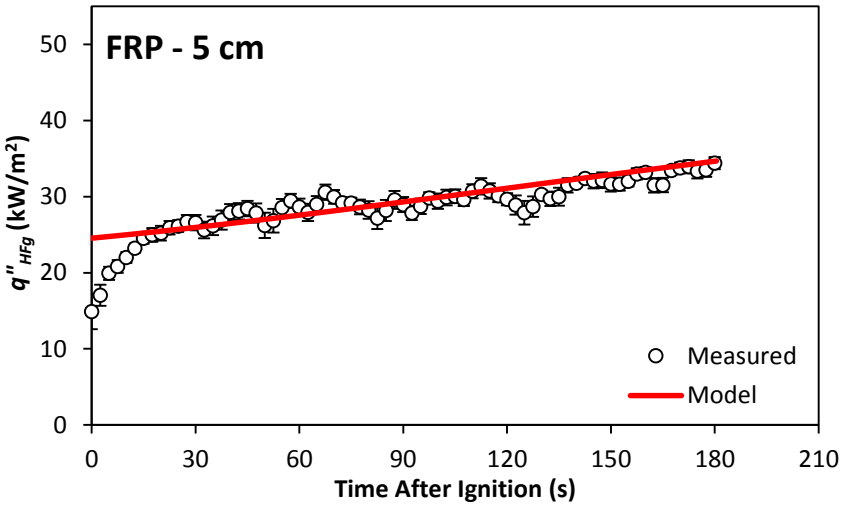

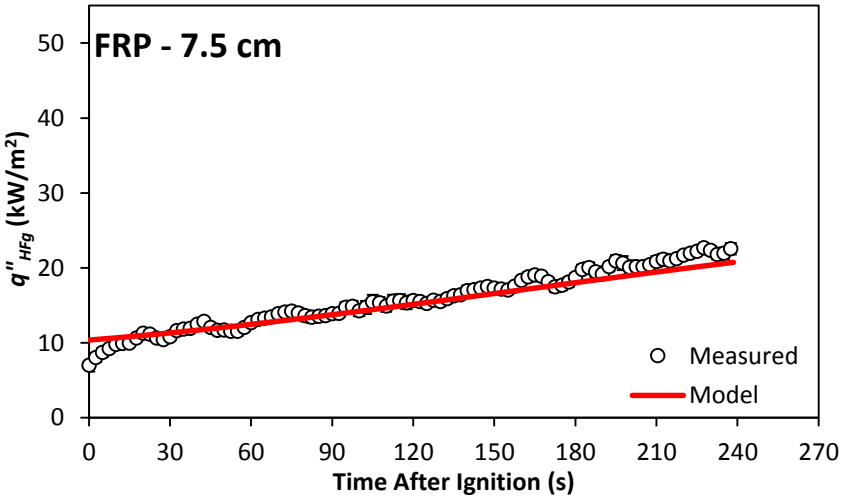

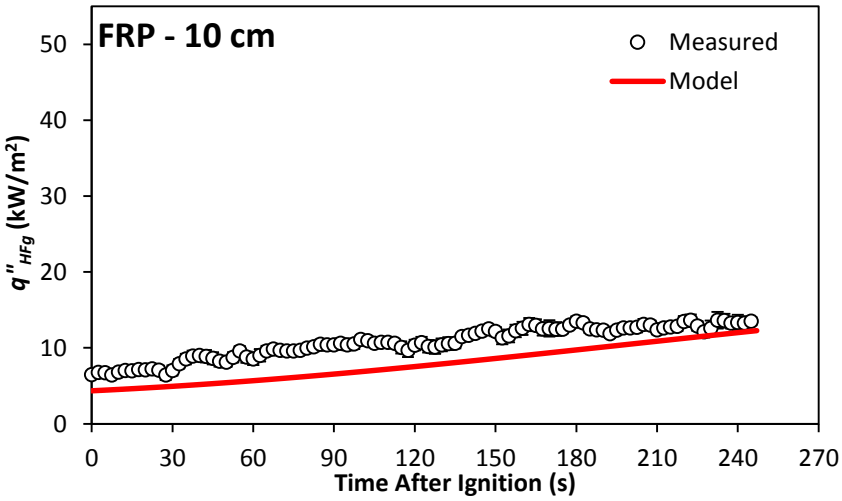

Figure 49. Measured and predicted $\boldsymbol{q''_{HFg}}$ using ΔH_T for FRP at 5, 7.5, and 10 cm

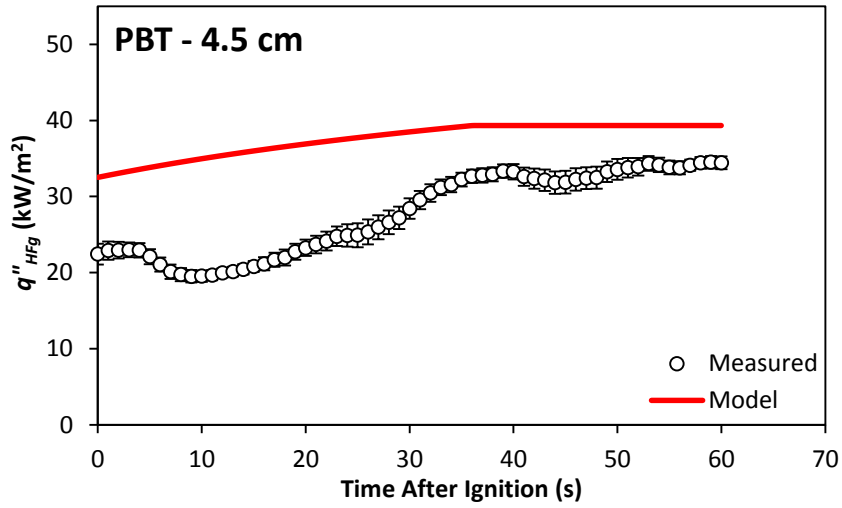

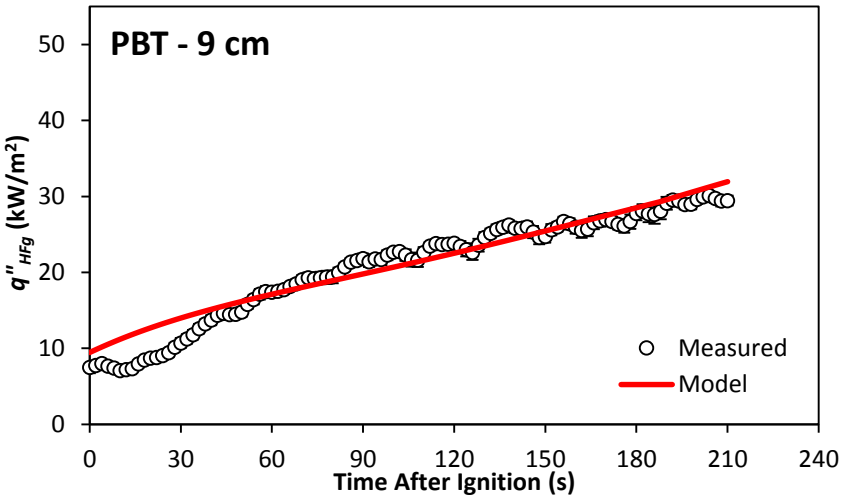

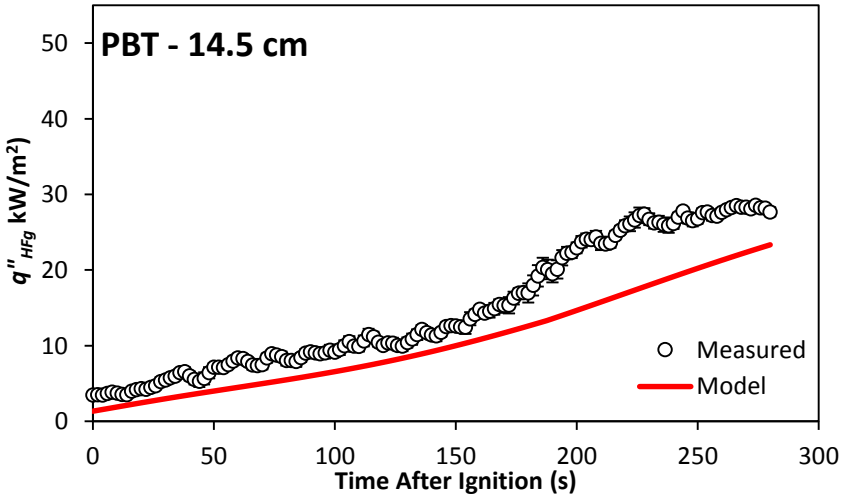

Figure 50. Measured and predicted $\boldsymbol{q''_{HFg}}$ using ΔH_T at 4.5, 9, and 14.5 cm

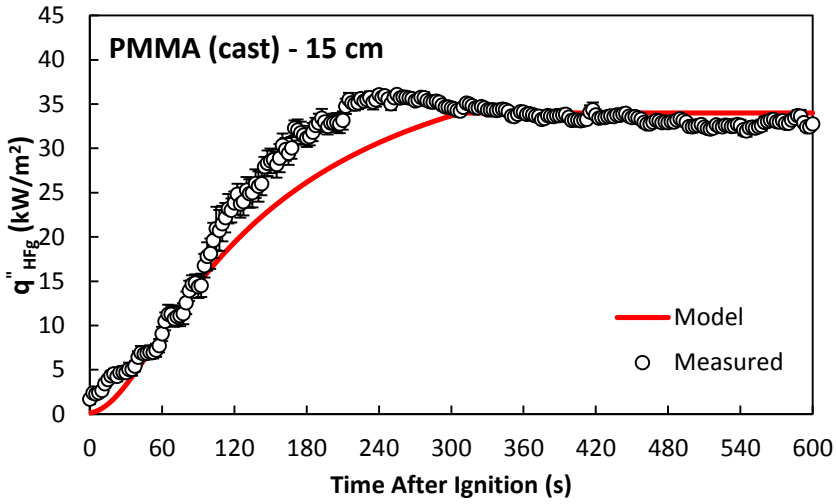

Figure 51. Measured and predicted $\boldsymbol{q''_{HFg}}$ using ΔH_T for cast PMMA at 15 cm.

In order to quantify how well the model predicts q''_{HFg} compared to experimental results, an error analysis is performed. The time-averaged absolute difference between predicted and measured q''_{HFg} is used to quantify the error because it gives a result that has a tangible meaning. Since heat flux measurements were obtained at a rate of 2 Hz, the error is calculated at each time step and then averaged over the entire prediction period.

The prediction period is dependent on the material and the sample height. For materials that had little to no deposits accumulate on the gauge during tests, the prediction period ends just before the burning behavior becomes non-ideal. For PP and POM, this was approximately 400 – 420 seconds after ignition and 600 seconds after ignition for cast PMMA. For materials that produced enough deposits for build-up on the gauge to noticeably impact measurements, either the prediction period was shortened to a time range where measurements are still reliable or, if shielded measurements were taken, the prediction period ends at the last shielded measurement. To account for shielded measurements in the error analysis, an interpolated line was fit through the shielded data points and the last reliable measurement from the full-length tests where deposits had not

begun impacting measurements. Up until this point, the prediction is compared to the measured points but after the last reliable measurement, the error is calculated by taking the difference between the predicted value and the equation for the interpolated line in 0.5 second intervals. Error analysis is done for each sample height to give a representative error value for that height. The error values for each height are then averaged to give a representative error for that material and finally the material error values are averaged to give an overall error value for the type of heat of combustion input parameter. Table 13 summarizes the results of the error analysis. For reference, the results from using the PMMA model without a heat of combustion input parameter are also included in the table.

Table 13. Summary of error analysis, values are in kW/m^2.

Input Parameter	POM	PMMA (cast)	PBT	HIPS	PP	FRP	ABS	Average
ΔH_T	9.3	2.1	5.2	3.5	1.7	1.6	4.4	**4.0**
$\Delta H_{c,horiz}$	7.7	2.0	5.0	9.3	2.1	4.0	7.6	**5.4**
$(1-\chi_r)\Delta H_{c,horiz}$	7.0	2.0	5.1	14.9	6.1	5.0	12.4	**7.5**
$\Delta H_{c,vert}$	8.6	2.1	6.3	1.9	2.1	12.4	6.4	**5.7**
None	10.8	2.1	5.6	10.1	9.1	2.1	5.4	**6.5**

From the table it is clear that using the MCC heat of combustion values, ΔH_T, provides the most accurate prediction over the range of materials studied here with an average error of 4.0 kW/m^2. The highest error when using ΔH_T as an input parameter is for POM, 9.3 kW/m^2. In an attempt to increase the accuracy of the prediction for POM, the radiative fraction was taken into account since POM has a distinctly blue flame and thus a small radiative fraction. While accounting for the radiative fraction did improve the prediction accuracy for POM, improving to 7.0 kW/m^2 as shown in Table 13 for the

$(1-\chi_r)\Delta H_{c,horiz}$ results, it decreased the prediction accuracy for the rest of the materials and produced the largest error amongst all the heat of combustion input parameters. If POM is not included in the overall average error value for ΔH_T, the average error drops from 4.0 kW/m^2 to 3.1 kW/m^2. Using ΔH_T gives a 39% increase in accuracy compared to using no heat of combustion input parameter, whereas using $(1-\chi_r)\Delta H_{c,horiz}$ results in a 16% decrease in accuracy. Interestingly, the $\Delta H_{eff,H}$ and ΔH_{vert} provided similar overall accuracies despite their differences in heat of combustion.

6.4. FDS DNS SIMULATIONS

Due to the high computational cost of running DNS simulations for a relatively large domain, at present, only two simulations have completed, two have reached ignition but are only a few seconds into burning, and the last simulation has not reached ignition yet. The first model to finish (45 seconds of simulation time) was the 0.4 mm grid simulation with default radiation and combustion models and it took just over 10 days to complete. The simulation with the wide band radiation model reached ignition within a few days but then slowed dramatically (< 1 second per day), as would be expected since the wide band model adds to the computational cost significantly once combustion begins. This model took approximately 4 weeks to finish. The default 0.2 mm grid simulation and the simulation with finite rate kinetics have also reached ignition but are now running at < 0.5 seconds per day. Additionally, the 0.1 mm grid default simulation has completed 13 seconds of simulation time and should reach ignition within the next two seconds. These three remaining simulations have all been running for over 1.5 months.

Despite the computational difficulties, the results look promising thus far. Ignition occurs at approximately 14.5 seconds for all simulations that have reached ignition and the flame is sustained upon removal of the simulated sample igniter 0.5 seconds after ignition. Figure 52 compares the resolution of the flame sheet at the base of the flame for the 0.2 mm grid and 0.4 mm grid simulations 2.5 seconds after ignition. There is a noticeable difference between flame sheet thicknesses and flame standoff distances between the two simulations. The flame sheet in the 0.2 mm grid simulation is half as thick as the flame sheet in the 0.4 mm grid simulation and the flame standoff distance is 33% larger in the 0.2 mm grid simulation. It is too early to say definitively what effect this is having on flame heat flux predictions within the simulations but preliminary results suggest higher flame heat fluxes from the 0.2 mm grid simulations, at least initially.

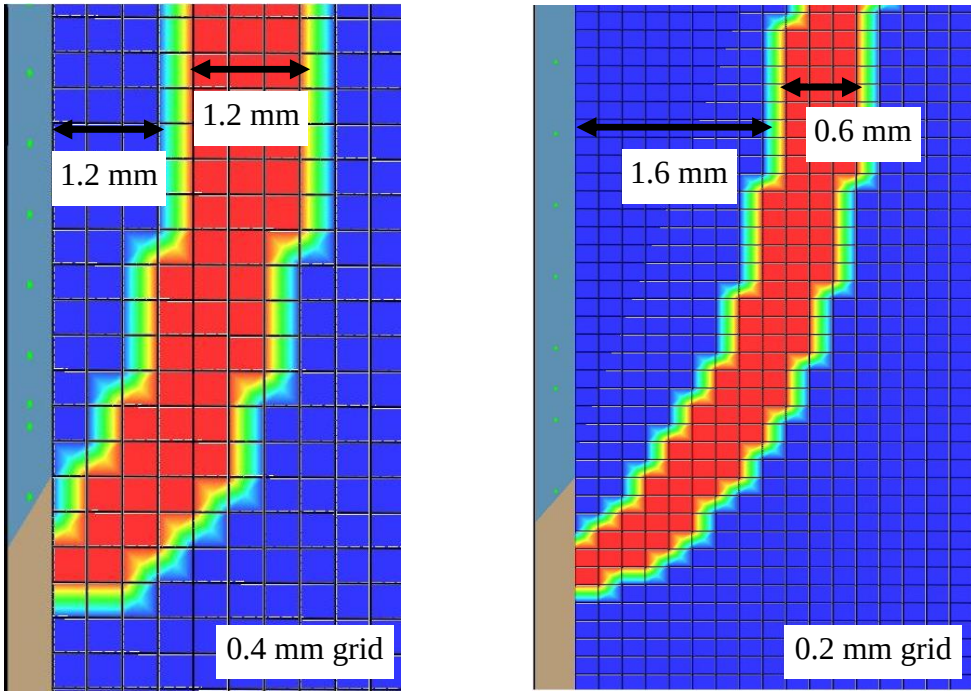

Figure 52. HRRPUV (kW/m^3) profiles at base of flame for 0.4 and 0.2 mm grid simulations 2.5 seconds after ignition where red is greater than 2.0 kW/m^3.

Figure 53 shows the velocity and temperature profiles 2.5 seconds after ignition in the 0.2 mm grid simulation.

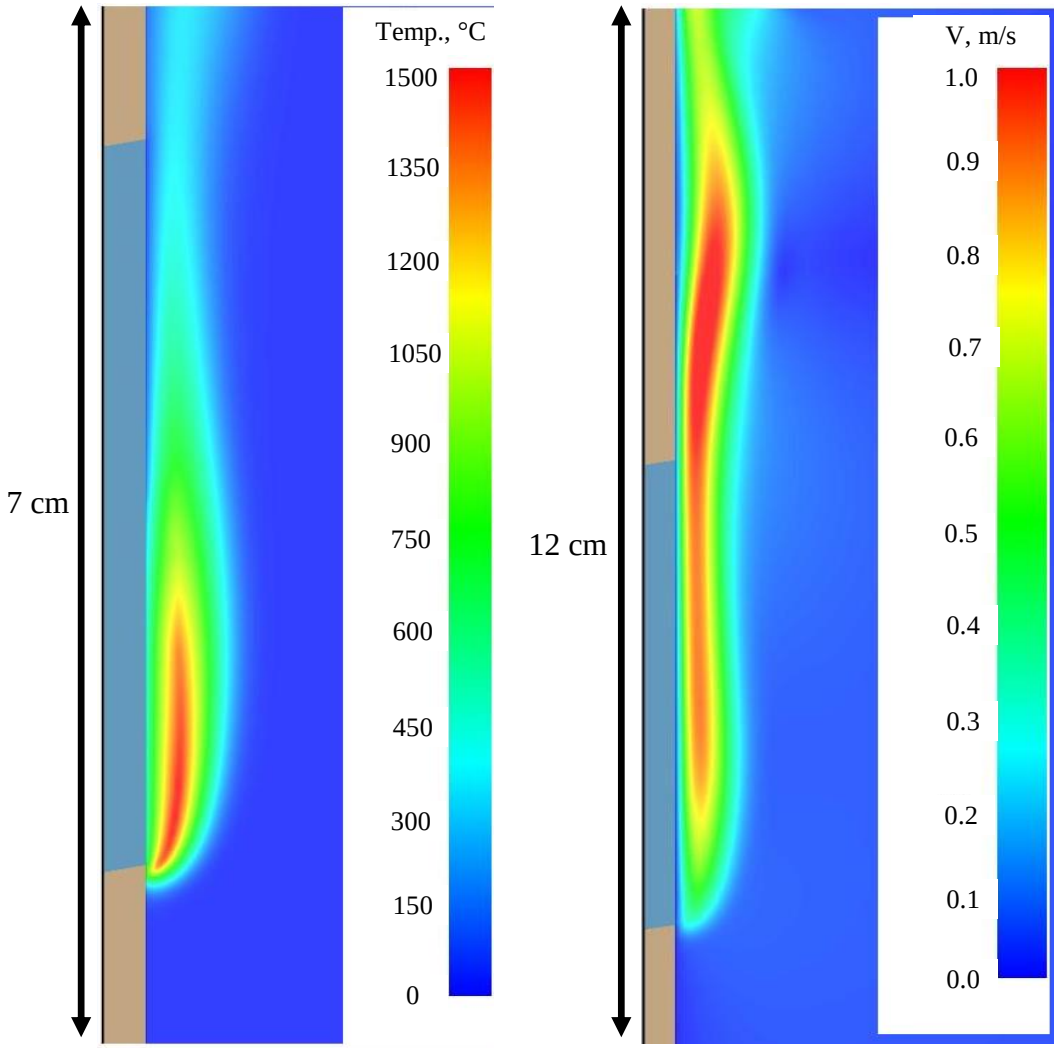

Figure 53. Temperature (°C) and velocity (m/s) profiles for the 0.2 mm grid simulation 2.5 seconds after ignition.

In order to analyze the predicted flame to surface heat flux in FDS, the generalized flame heat flux model developed in this study is utilized. Since the generalized model has been proven to work very well for PMMA, it is logical to use the generalized model as a comparison to the results predicted by FDS. The same procedure as outlined in the previous section can be performed to predict the flame to surface heat

flux using the mass loss rate predicted by FDS with one important difference. In FDS, the net convective and radiative heat fluxes, $q''_{c,net}$ and $q''_{r,net}$, were predicted in 0.8 mm intervals vertically along the surface of the sample so the total net heat flux to the surface, q''_{net}, is the sum of those two fluxes. The generalized flame heat flux model, in its current form, predicts the heat flux to a cold gauge but it can be adjusted to predict q''_{net} by using slightly modified versions of Equations (14) – (16161616) that use the surface temperature of the sample, T_s, predicted by FDS instead of T_{HFg}, as shown below.

$$q''_{net} = h(T^* - T_{surf} + T_{HFg}) \tag{18}$$

$$\text{for } y \le y_f \qquad T^* = \begin{cases} T_{fl,ad} - T_{HFg} & ; y \le 5 \text{ cm} \\ \left(\frac{34}{40}\right)(T_{fl,ad} - T_{HFg}) & ; y > 5 \text{ cm} \end{cases} \tag{19}$$

$$\text{for } y > y_f \quad T^* = \begin{pmatrix} T_{fl,ad} - T_{HFg} & ; y \le 5 \text{ cm} \\ \left(\frac{34}{40}\right)(T_{fl,ad} - T_{HFg}) & ; y > 5 \text{ cm} \end{pmatrix} \times \alpha\left(e^{-\ln(\alpha)\times(y^*)^2}\right) \tag{20}$$

This comparison method inherently assumes that the condensed phase pyrolysis model in FDS accurately predicts the mass loss rate of PMMA. As discussed in Section 4.4 and portrayed in Figure 12, the FDS pyrolysis model agrees well with the Thermakin2D pyrolysis model, which has proven to accurately predict experimental mass loss rate measurements so this assumption is valid. The comparison of predicted q''_{net} values from the FDS 0.4 mm grid default simulation and generalized flame heat flux model using ΔH_T as the input parameter is shown in Figure 54 for the 30 seconds of simulated burning after ignition at a height of 5 cm.

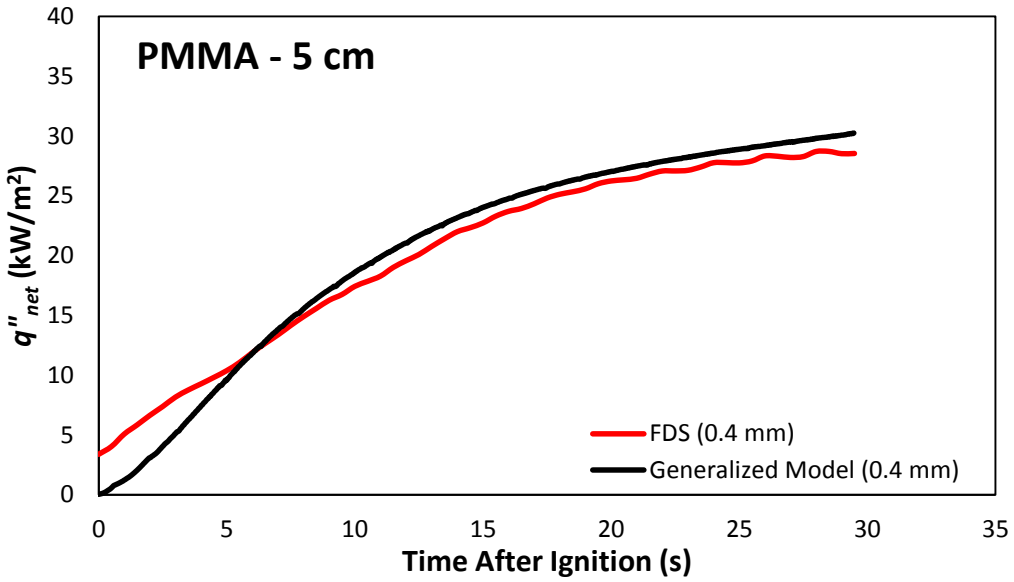

Figure 54. Predicted q''_{net}comparison from FDS and the generalized flame heat flux model for PMMA at y = 5 cm for the 0.4 mm grid default simulation.

This plots show good agreement between FDS and the generalized flame heat flux model for q''_{net} predictions. The higher predicted heat fluxes in the FDS simulation just after ignition could be due to the default combustion model used in FDS. The combustion model assumes infinitely fast chemistry and that ignition occurs within a cell if sufficient fuel and oxidizer are present to increase the cell temperature to the critical flame temperature (default is 1600 K) [25]. This can result in combustion occurring earlier than is actually feasible. For example, in the 0.4 mm grid simulation, combustion begins to take place almost immediately in the first two cells in front of the sample surface over the bottom 2 cm of the sample until 14.5 seconds when the actual flame is formed. This could be causing the increased q''_{net} predicted by FDS in the first 15 seconds after ignition.

Figure 55 compares the FDS predictions from the 0.2 mm grid default simulation to the predictions from the generalized model. The predictions are in good agreement

through the first 10 seconds of simulation time. Again, the higher heat flux initially in the FDS prediction is likely due to the combustion reaction occurring at the surface of the sample prior to the presence of the flame. Since the 0.1 mm grid default simulation has not reached ignition yet, no comparison can be made between the FDS and generalized model predictions for this simulation.

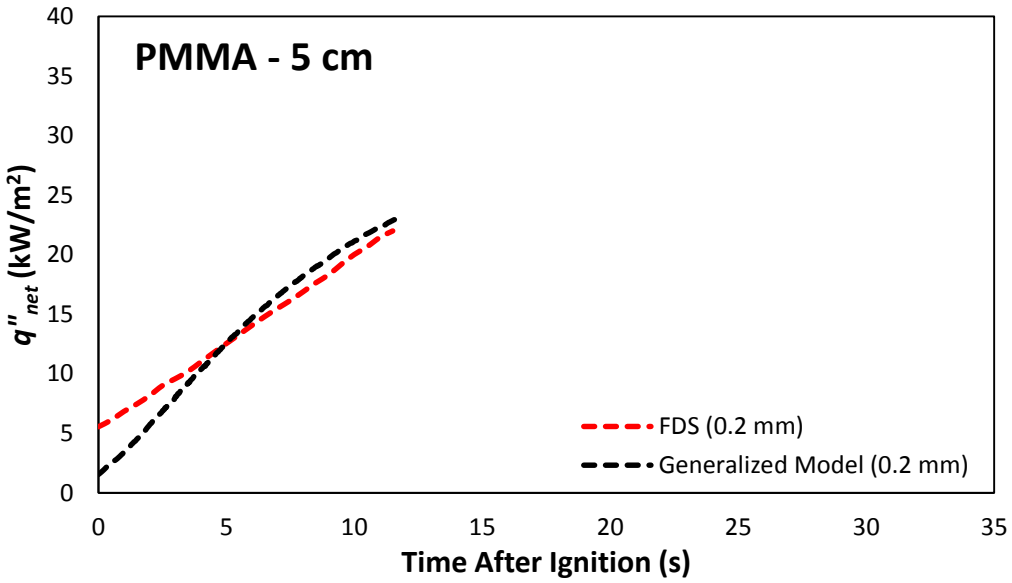

Figure 55. Predicted q''_{net}comparison from FDS and the generalized flame heat flux model for PMMA at y = 5 cm for the 0.2 mm grid default simulation.

Figure 56 compares the FDS predictions from the 0.4 mm grid wide band model simulation to the predictions from the generalized model. These predictions show some disagreement, with the generalized model predicting a faster rise in heat flux and a greater steady state heat flux. The steady-state q''_{net} predictions are decreasing slightly because the surface temperature is still increasing at this point in time. It is difficult to conclude what is causing the difference in predictions because the radiation model was not the only change implemented for this simulation. Due to an unknown issue, this simulation was not able to be initiated unless the gas-phase properties (thermal

conductivity, specific heat, diffusivity, and kinematic viscosity) of MMA were set to the default values instead of being specified as had been done for the other, gray gas (default) model simulations. Thus, since the heat flux is primarily convective and gas-phase properties are critical to convective heat transfer, the difference in predictions could simply be the result of the difference in gas-phase properties rather than the difference in radiation models.

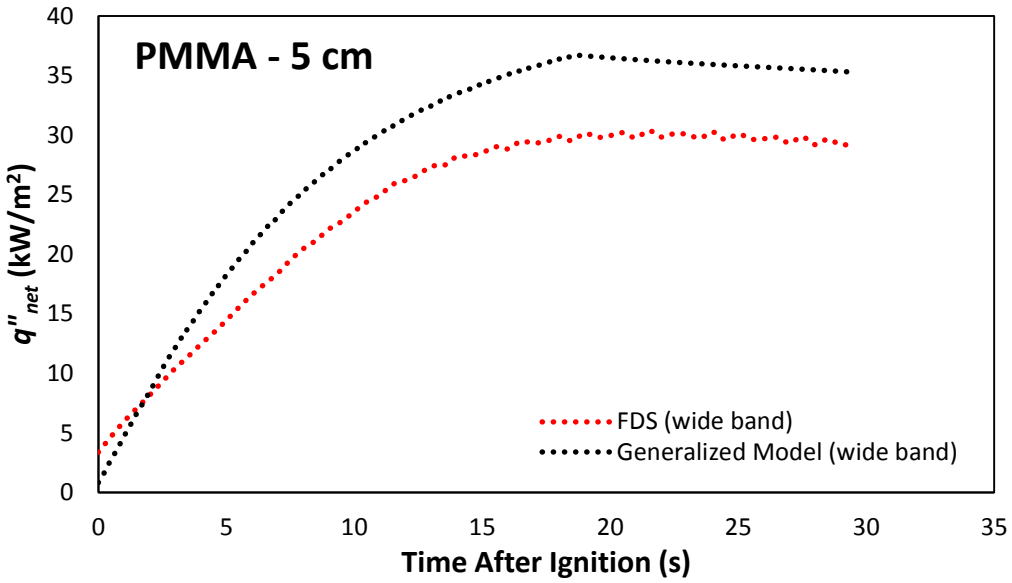

Figure 56. Predicted q''_{net} comparison from FDS and the generalized flame heat flux model for PMMA at y = 5 cm for the 0.4 mm grid wide band radiation model simulation.

Finally, Figure 57 compares the FDS predictions from the 0.4 mm grid finite rate kinetics simulation to the predictions from the generalized model. With this simulation only roughly seven seconds into burning it is difficult to draw any conclusions but the initial rise in heat flux shows promise.

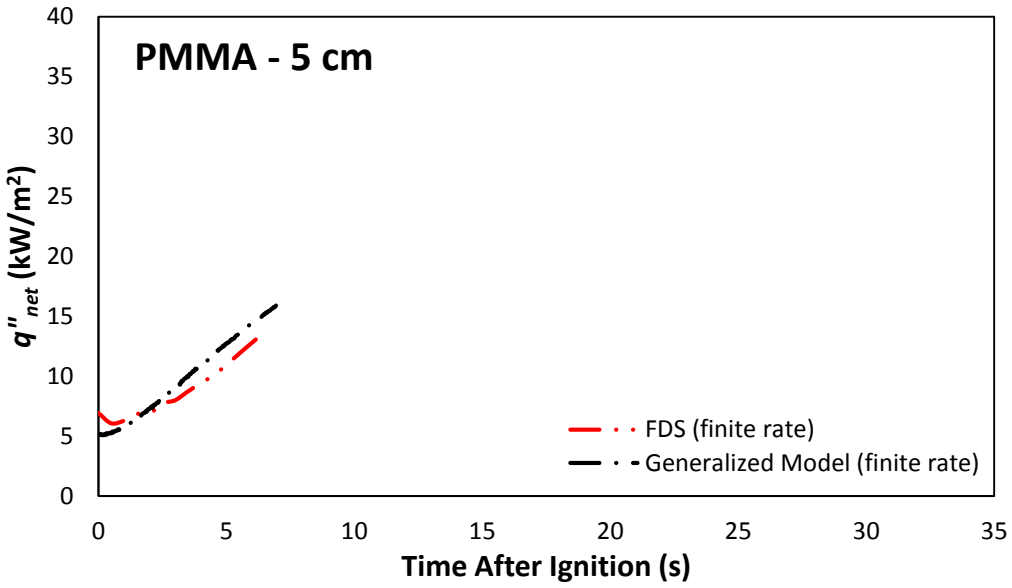

Figure 57. Predicted q''_{net} comparison from FDS and the generalized flame heat flux model for PMMA at y = 5 cm for the 0.4 mm grid finite rate kinetics simulation.

Overall, the FDS predictions are showing agreement with the generalized model predictions. At present, with the significant amount of computational time required to produce the heat flux predictions, it is advantageous to use the generalized heat flux model along with, at most, two experimental tests (mass loss rate and total heat of combustion) to obtain accurate heat flux predictions. As computing power continues to increase, these methods may be able to be used simultaneously.

7. CONCLUSIONS

A model exists that accurately predicts the flame to surface heat flux for small-scale upward flame spread on PMMA that requires mass loss rate as the single input parameter. The focus of this study was to generalize the model by adding a second input parameter, the heat of combustion, which allows the model to be extended to a broad range of polymers. Seven polymers (POM, PP, HIPS, FRP, PBT, ABS, and cast

PMMA) with unique burning behaviors were analyzed to determine which heat of combustion value yields the most accurate flame to surface heat flux predictions. For each material, mass loss rate measurements during upward flame spread and heat of combustion measurements in several different configurations were collected to obtain the two input parameters for the model. Experimental heat flux measurements to a water-cooled gauge during small-scale upward flame spread were collected to verify the accuracy of the model's predictions.

The following four heat of combustion values were evaluated to determine which yielded the most accurate model prediction: heat of complete combustion (ΔH_T), effective heat of combustion ($\Delta H_{eff,H}$), heat of combustion in the vertical orientation with no external heat flux (ΔH_{vert}), and the effective heat of combustion accounting for the radiant fraction($(1-\chi_r)\Delta H_{eff,H}$). $\Delta H_{eff,H}$ and ΔH_{vert} were measured in the cone calorimeter as part of this study while ΔH_T and χ_r were obtained from literature. Two scaling parameters were calculated from these values using Equations (12) and (14) – (16), to give a time and height-dependent flame to surface heat flux prediction. The predictions were compared to experimental flame to surface heat flux measurements at each height, for each material, and using each heat of combustion value. An error analysis was performed to quantify the accuracy of the predictions. Of the four values, ΔH_T yielded the most accurate predictions. Using ΔH_T as an input parameter, predicted flame to surface heat flux values were within ± 4.0 kW/m^2 on average. Lastly, direct numerical simulations were performed using Fire Dynamics Simulator (FDS) to predict flame to surface heat flux during upward flame spread on PMMA. The FDS predictions were in agreement with the generalized heat flux model predictions.

8. APPENDIX

8.1. CONE CALORIMETER OPERATING PROCEDURES

In order to obtain consistent and accurate measurements from the cone calorimeter, a systematic operating and cleaning method was utilized. It was determined through numerous tests that maintaining the stack thermocouple, stack pressure differential ports, gas sampling ring ports, and soot filter free from soot and other deposits was critical to obtaining consistent and accurate measurements. Therefore, the following cleaning and calibration procedure was applied during testing:

1. Before testing, at beginning of day:
    a. Remove gas sampling ring, clean, and use compressed air to blow through opening, in opposite direction of normal flow, to remove build-up of deposits. Also, blow out any additional metal tubing between sampling ring and soot filter. If possible, perform these operations so that the contaminated air is captured by ventilation. Reinstall sampling ring.
    b. Remove stack thermocouple and stack differential pressure tubes. Clean thermocouple and blow compressed air through all three ports (one thermocouple and two pressure) in the stack. Reinstall thermocouple and pressure tubes.
    c. Remove soot filter and clean out or replace if necessary. Frequency of soot filter replacement is highly dependent on the amount of soot produced by the materials being tested. Replace HEPA filter. Reinstall soot filter.
    d. Calibrate gas analyzer.

e. Perform C-factor calibration. Ensure that C-factor is within expected range. For the testing performed in this study, that range was consistently 0.0375 ± 0.0005.

f. Perform calibration check using 10 x 10 x 1.2 cm black cast PMMA.

2. Begin testing. For this study, since there was a range of materials with different amounts of soot produced, a lower soot producing material (i.e. POM, PMMA, PP, HPDE, etc.) would be tested first followed by a higher soot producing material (i.e. HIPS, ABS, etc.). This way, the soot produced by the second material would not interfere with the measurements for the first material. Then, after this set of two tests a cleaning procedure similar to that done at the beginning of the day would be performed, as outline below:

    a. Leave sample ring in place but remove first metal tube connected to sampling ring port and use compressed air to blow through sampling ring. Also, blow through the removed metal tube into ventilation. Reinstall metal tube.

    b. Remove stack thermocouple and stack differential pressure port tubes. Clean thermocouple and blow air through all three ports in stack. Reinstall thermocouple and pressure tubes.

    c. Remove soot filter and remove any soot build-up on filter. Replace if necessary. Reinstall soot filter.

    d. Perform C-factor calibration. Ensure that C-factor is within expected range.

3. Begin testing again. If only higher soot producing materials are being tested, repeat cleaning procedure more frequently or vice versa if less soot producing materials are being tested.
4. At end of day, perform additional calibration check using 10 x 10 x 1.2 cm black cast PMMA to check for any drift in measurements. For the results of the initial and final calibration checks from each day of testing, see Section 8.2.

8.2. BLACK CAST PMMA $\Delta H_{EFF,H}$ RESULTS

$\Delta H_{eff,H}$ tests were performed on black cast PMMA as the initial and final tests on each day of cone calorimeter testing to ensure accuracy of measurements and check for significant drift. The results of these tests are shown in Table 14. Given the results of a repeatability analysis done in the ASTM E1354 standard, the repeatability, as listed in the standard, for $\Delta h_{c,eff}$ was $r = 1.23 + 0.050\ \Delta h_{c,eff}$. For $\Delta h_{c,eff}$ = 24.7 kJ/g, the repeatability is ± 2.5 kJ/g [52]. The largest difference between initial and final measurements of $\Delta H_{eff,H}$ in this study was 0.7 kJ/g, well within the range of accuracy listed in the standard. All $\Delta H_{eff,H}$ are calculated using the same quasi steady-state technique as described in 4.3.2. Unless otherwise noted, all measurements were performed on 1.2 cm thick samples.

Table 14. $\Delta H_{eff,H}$ results for black cast PMMA tests.

Date	$\Delta H_{eff,H}$ (Black cast PMMA)	
	Initial	Final
12/24/2014	25.3	24.7
12/26/2014	24.6	24.7
12/29/2014	24.7[a]	---
12/30/2014	24.7	24.4[b]
12/31/2014	24.2[b]	24.5[b]
1/2/2015	24.3[b]	25.0[c]
1/7/2015	24.7	24.8
1/22/2015	24.7	24.7
1/23/2015	24.7	24.9
1/27/2015	24.7	25.2
1/30/2015	24.5	24.6
2/3/2015	24.8	
2/5/2015	24.8	24.5
2/6/2015	24.3	
Average	24.6	24.7
$2 \times \sigma_{mean}$	0.1	0.1

a) Only one test performed this day
b) 0.6 cm thick
b) 2.4 cm thick

8.3. EQUATIONS FOR INTERPOLATED LINES THROUGH SHIELDED TEST RESULTS

In order to perform an error analysis for predictions involving materials for which shielded tests were conducted as described in Section 4.3.3, interpolated lines were fit through the representative heat flux measurements obtained from the shielded tests for each sample height. These interpolated lines are shown in the prediction results curves for HIPS and ABS, Figure 47 and Figure 48. Both linear and polynomial equations were used depending on which form provided the best fit. The equations used for each sample height for ABS and HIPS are shown in Table 15 using the polynomial equation shown below

$$q''_{HFg} = at^4 + bt^3 + ct^2 + dt + e \quad (21)$$

where *m* is the slope, *k* is the y-intercept, *a* – *e* are the polynomial coefficients, and *t* is the time in seconds.

Table 15. Polynomial coefficients for the interpolated lines through shielded heat flux measurements for ABS and HIPS.

Height (cm)	Time Range (s)	Polynomial Coefficients				
		a	***b***	***c***	***d***	***e***
ABS						
5	15 - 86	---	---	---	0.15	33.0
	86 - 281	---	---	---	-0.034	48.9
	281 - 473	---	---	---	-0.00159	40.0
7	18 - 455	-1.59E-09	2.25E-06	-0.0012	0.23	27.9
11	24 - 449	---	---	-9.11E-05	0.088	18.0
15	30 - 305	---	---	-3.51E-04	0.21	2.7
HIPS						
5	22 - 63	3.06E-06	-3.82E-04	0.0073	0.67	12.8
7.5	30 - 93			-0.0018	0.35	9.5
10	66 - 183			-4.88E-04	0.19	3.1

8.4. ERROR ANALYSIS FOR HEAT FLUX MEASUREMENTS

The error bars for heat flux measurements were calculated using two times the standard deviation of the mean. Instead of calculating the mean at each time step, which could be affected by noise in the measurements and not represent actual heat flux measurements, one or more fitted polynomial curves were used to represent the averaged heat flux measurements at each height. The equation for the standard deviation of the mean is expressed as,

$$\sigma_{mean} = \sqrt{\frac{\sum_i^N (q''_{HFg,i} - \bar{q}''_{HFg})^2}{N(N-1)}} \quad (22)$$

where *N* represents the number of tests performed for the height and material of interest and *i* represents an individual test. The equations of the fitted lines for each material are expressed by Equation (23) and the polynomial coefficients are given in Table 16.

$$q''_{HFg} = at^6 + bt^5 + ct^4 + dt^3 + et^2 + ft + g \quad (23)$$

Table 16. Polynomial coefficients for fitted curves that represent heat flux measurements in order to calculate a more accurate standard deviation of the mean.

Height (cm)	Time Range (s)	Polynomial Coefficients						
		a	*b*	*c*	*d*	*e*	*f*	*g*
Cast PMMA								
15	0 - 240	-5.72E-12	4.42E-09	-1.27E-06	1.60E-04	-0.0079	0.24	1.4
	240-600				4.62E-08	-2.52E-05	-0.013	39.8
PP								
5	0 - 400		2.97E-11	-3.86E-08	1.91E-05	-0.0045	0.50	9.3
7	0 - 400			-1.52E-09	1.68E-06	-7.53E-04	0.19	8.5
10	0 - 400	-5.03E-14	4.96E-11	-1.45E-08	5.49E-07	2.35E-04	0.031	4.5
12	0 - 400				-1.32E-07	6.12E-05	0.025	3.5
15	0 - 400				-5.89E-08	3.15E-05	0.007	2.4
POM								
5	0 - 140		1.01E-09	-2.16E-07	6.72E-06	8.46E-04	0.24	6.8
	140 - 389				-4.58E-07	2.67E-04	-0.041	47.6
7.5	0 - 400			1.21E-08	-1.07E-05	0.0027	-0.043	6.6
10	0 - 420		3.89E-11	-4.04E-08	1.31E-05	-0.0013	0.13	2.3
12.5	0 - 425	1.74E-13	-2.32E-10	1.09E-07	-2.14E-05	0.0019	-0.016	1.9
HIPS								
5	0 - 20					-0.0071	0.84	12.3
	20 - 297				1.97E-06	-9.80E-04	0.071	25.3
7.5	0 - 315		1.19E-10	-1.06E-07	3.60E-05	-0.0059	0.42	9.4
10	0 - 395		2.55E-11	-2.87E-08	1.27E-05	-0.0028	0.28	2.4
PBT								
4.5	0 - 40			-1.27E-05	4.21E-04	0.026	-0.64	23.8
	40 - 400				-2.61E-07	2.23E-04	-0.037	34.5
9	0 - 223	3.08E-12	-2.75E-09	9.27E-07	-1.45E-04	0.0099	-0.080	7.5
	223 - 400			1.77E-08	-2.34E-05	0.011	-2.4	220.7
14.5	0 - 280	3.68E-12	-3.16E-09	9.91E-07	-1.38E-04	0.0085	-0.12	4.1
FRP								
5	0 - 100				3.76E-05	-0.0077	0.51	17.1
	100 - 386		-9.48E-11	1.10E-07	-4.83E-05	0.0097	-0.85	55.2
7.5	0 - 230		1.60E-10	-1.02E-07	2.46E-05	-0.0027	0.17	7.9
	230 - 400						-0.013	25.3
10	0 - 430				1.46E-07	-1.61E-04	0.060	6.1
ABS								
5	0 - 50		5.98E-07	-9.57E-05	0.0058	-0.16	2.2	23.3
	50 - 400			-2.43E-10	1.36E-07	7.98E-05	-0.076	42.2
7	0 - 480			-2.37E-09	2.88E-06	-0.0012	0.15	27.9
11	0 - 100	-8.35E-10	2.87E-07	-3.85E-05	2.52E-03	-0.083	1.3	11.4
	100 - 400				6.40E-07	-5.61E-04	0.13	16.7
15	0 - 330		1.39E-10	-1.08E-07	2.79E-05	-0.0030	0.27	2.7

REFERENCES

[1] K.-C. Tsai, J. Turnbull, W. Gavin and D. Drysdale, "Upward Flame Spread: Heat Transfer to the Unburned Surface," in *Proceedings of the Seventh International Symposium for Fire Safety Science*, Worcester, MA, 2002.

[2] Y. Pizzo, J. L. Consalvi, P. Querre, M. Coutin and B. Porterie, "Width effects on the early stage of upward flame spread over PMMA slabs; Experimental observations," *Fire Safety Journal*, vol. 44, pp. 407-414, 2009.

[3] A. C. Fernandez-Pello and T. Hirano, "Controlling Mechanisms of Flame Spread," *Combustion Science and Technology*, vol. 32, no. 1-4, pp. 1-31, 1983.

[4] J. G. Quintiere, "An Assessment of Correlations Between Laboratory and Full-Scale Experiments for the FAA Aircraft Fire Safety Program," Nation Bureau of Standards, U.S. Department of Commerce, Washington, D.C. , 1982.

[5] M. L. Janssens, "Chapter 10 Material Flammability," in *Handbook of Environmental Degradation of Materials*, Norwich, NY, William Andrew Publishing, 2005, pp. 207-255.

[6] R. E. Lyon, N. Safronava, J. G. Quintiere, S. I. Stoliarov, R. N. Walters and S. Crowley, "Material Properties and Fire Test Results," *Fire and Materials*, vol. 38, no. 2, pp. 264-278, 2014.

[7] J. N. de Ris, "Spread of a Laminar Diffusion Flame," *Symposium (International) on Combustion*, vol. 12, no. 1, pp. 241-252, 1969.

[8] H. W. Emmons, "Fundamental Problems of the Free Burning Fire," in *Tenth*

Symposium (International) on Combustion, 1965.

[9] J. S. Kim and F. W. Kroesser, "Laminar Fee-Convective Burning of Fuel Surfaces," *Symposium (International) on Combustion,* vol. 13, no. 1, pp. 949-961, 1971.

[10] L. Orloff, J. De Ris and G. H. Markstein, "Upward Turbulent Fire Spread and Burning of Fuel Surface," *Symposium (International) of Combustion,* vol. 15, no. 1, pp. 183-192, 1975.

[11] A. Fernandez-Pello, "Upward Laminar Flame Spread Under the Influence of Externally Applied Thermal Radiation," *Combustion Science and Technology,* vol. 17, no. 3-4, pp. 97-98, 1977.

[12] T. Ahmad and G. M. Faeth, "Turbulent Wall Fires," *Symposium (International) on Combustion,* vol. 17, no. 1, pp. 1149-1160, 1979.

[13] K. Annamalai and M. Sibulkin, "Flame Spread Over Combustible Surfaces for Laminar Flow Systems Part II: Flame Heights and Fire Spread Rates," *Combustion Science and Technology,* vol. 19, no. 5-6, pp. 185-193, 1979.

[14] K. Saito, J. G. Quintiere and F. A. Williams, "Upward Turbulent Flame Spread," in *Proceedings of the First International Symposium on Fire Safety Science*.

[15] E. Brehob, C. Kim and A. Kulkarni, "Numerical Model of Upward Flame Spread on Practical Wall Materials," *Fire Safety Journal,* vol. 36, no. 3, pp. 225-240, 2001.

[16] M. Sibulkin and J. Kim, "The Dependence of Flame Propagation on Surface Heat Transfer II. Upward Burning," *Combustion Science andTechnology,* vol. 17, no. 1-2, pp. 39-49, 1977.

[17] A. V. Singh and M. J. Gollner, "A Methodolgy for Estimation of Local Heat Fluxes

in Steady Laminar Boundary Layer Diffusion Flames," *Combustion and Flame,* p. http://www.sciencedirect.com/science/article/pii/S0010218015000310, (In Press).

[18] A. Ito and T. Kashiwagi, "Characterization of Flame Spread over PMMA Using Holographic Interferometry Sample Orientation Effects," *Combustion and Flame,* vol. 71, no. 2, pp. 189-204, 1988.

[19] B. Y. Lattimer, "Section 2, Chapter 14 - Heat Fluxes from Fires to Surfaces," in *SFPE Fire Protection Engineering Handbook, Fourth Edition*, Quincy, MA, National Fire Protection Assoication, 2008, pp. 2-303 - 2-334.

[20] M. A. Delichatsios and K. Saito, "Upward Fire Spread: Key Flammability Properties, SImilarity Solutions and Flammability Indicies," in *Proceedings of the Third International Symposium for Fire Safety Science*, Edinburgh, Scotland, 1991.

[21] T. G. Cleary and J. G. Quintiere, "A Framework for Utilizing Fire Property Tests," in *Proceedings of the Third International Symposium on Fire Safety Science*, Edinburgh, 1991.

[22] C. L. Beyler, S. P. Hunt, N. Iqbal and F. W. Williams, "A Computer Model of Upward FLame Spread on Vertical Surfaces," in *Proceedings of the Fifth International Symposium on Fife Safety Science*, Melbourne, 1997.

[23] I. T. Leventon and S. I. Stoliarov, "Evolution of Flame to Surface Heat Flux During Upward Flame Spread on Poly(methyl methacrylate)," *Proceedings of the Combustion Institute,* vol. 34, no. 2, pp. 2523-2530, 2013.

[24] J. Consalvi, Y. Pizzo, B. Porterie and J. Torero, "On the Flame Height of Definition for Upward Flame Spread," *Fire Safety Journal,* vol. 42, no. 5, pp. 384-392, 2007.

[25] K. McGrattan, S. Hostikka, R. McDermott, J. Floyd, C. Weinschenk and K. Overholt, "Fire Dynamics Simulator User's Gude, Special Publication 1019," National Institute of Standards and Technology, Gaithersburg, MD, 2013.

[26] M. McKinnon, "Development of a Model for Flaming Combusiton of Double-Wall Corrugated Cardboard," University of Maryland, Master's Thesis, 2012.

[27] I. T. Leventon, "Evolution of Flame to Surface Heat Flux During Upward Flame Spread on Polymethyl Methacrylate (PMMA)," College Park, 2011.

[28] C. Huggett, "Estimation of Rate of Heat Release by Means of Oxygen Consumption Measurements," *Fire and Materials*, vol. 4, pp. 61-65, 1908.

[29] V. Babrauskas, "Development of the Cone Calorimeter -- A Bench-Scale Heat Release Rate Apparatus Based on Oxygent Consumption," National Bureau of Standards, U.S. Department of Commerce, Washington, D.C. , 1982.

[30] V. Babrauskas, "Section 3, Chapter 3 - The Cone Calorimeter," in *SFPE Handbook Fire Protection Engineering, Fourth Edition*, Quincy, MA, National Fire Protection Association, 2008, pp. 3-90 - 3-108.

[31] A. Tewarson, "Section 3, Chapter 4 - Generation of Heat and Gaseous, Liquid, and Solid Products in Fires," in *SFPE Fire Protection Engineering Handbook, Fourth Edition*, Quincy, MA, National Fire Protection Association, 2008, pp. 3-109 - 3-194.

[32] R. Lyon, "Chapter 3, Plastics and Rubber," in *Handbook of Building Materials for Fire Protection*, New York, McGraw-Hill, 2004.

[33] ASTM International, " ASTM D7309: Standard Test Method for Determining Flammability Characteristics of Plastics and Other Solid Materials Using Microscale

Combustion Calorimetry," 2014.

[34] R. E. Lyon, R. N. Walters, S. I. Stoliarov and N. Safronava, "Principles and Practice of Microscale Combustion Calorimetry," DOT, Renton, 2013.

[35] F. Raffan, X. Ding and S. I. Stoliarov, "Milligram Scale Flame Calorimeter: A Novel Instrument for Flammability Assessment Using MG Sized Samples," in *Fire and Materials* , San Francisco, CA, 2015.

[36] J. Li and S. I. Stoliarov, "Measurement of Kinetics and Thermodynamics of the Thermal Degradation for Non-Charring Polymers," *Combustion and Flame,* vol. 160, no. 7, pp. 1287-1287, 2013.

[37] M. M. Hirschler and A. B. Morgan, "Section 1, Chapter 7 - Thermal Decomposition of POlymers," in *SFPE Handbook of Fire Protection Engineering, 4th Edition*, SFPE, 2008, pp. 1-112 - 1-143.

[38] T.-H. Tsai, M.-J. Li, I.-Y. Shih, R. Jih and S.-C. Wong, "Experimental and Numerical Study of Autoignition and Pilot Ignition of PMMA Plates in a Cone Calorimeter," *Combustion and Flame,* vol. 124, pp. 466-480, 2001.

[39] C. L. Yaws, Handbook of Thermal Conductivity, Volume 2, Houston: Gulf Publishing Company, 1995.

[40] C. L. Yaws, Handbook of Viscosity, Volume 2, Houston: Gulf Publishing Company, 1995.

[41] B. E. Poling, J. M. Prausnitz and J. P. O'Connell, The Properties of Gases and Liquids, Fifth Edition, McGraw-Hill, 2001.

[42] K. Seshardi and F. A. Williams, "Effect of CF3Br on Counterflow Combustion of

Liquid Fuel with DIluted Oxygen," in *Halogenated Fire Suppressants*, D.C., American Chemical Society, 1975, pp. 149-182.

[43] S. I. Stoliarov, I. T. Leventon and R. E. Lyon, "Thermakin2D Technote: Two-Dimensional Model of Burning for Pyrolyzable Solids," National Technical Information Services, Springfield, VA, 2012.

[44] K. McGrattan, S. Hostikka, R. McDermott, J. Floyd, C. Weinschenk and K. Overholt, "Fire Dynamics Simulator Technical Reference Guide, Volume 1: Mathematical Model," National Institute of Standards and Technology Special Publication 1018, Gaithersburg, MD, 2013.

[45] I. Leventon and S. Stoliarov, "Characterization of Flame Growth on ABS by Measurement of Flame to Surface Heat Feedback," in *Proceedings of the Seventh International Seminart for Fire & Explosion Hazards*, Providence, RI, 2013.

[46] R. E. Lyon and M. L. Janssens, "Polymer Flammability, DOT/FAA/AR-05/14," National Technical Information Service, Springfield, VA, 2005.

[47] A. Tewarson, J. L. Lee and R. F. Pion, "The Influence of Oxygen Concentration on Fuel Parameters for Fire Modeling," *Symposium (Internation) on Combustion*, vol. 18, no. 1, pp. 563-570, 1981.

[48] A. Tewarson, "Experimental Evaluation of Flammability Parameters of Polymeric Materials," in *Flame - Retardant Polymeric Materials*, New York, Plenum Press, 1982, pp. 97-153.

[49] J. G. Quintiere, R. Lyon and S. Crowley, "An Excercise in Obtaining Flame Radiation Fraction From the Cone Calorimeter," in *Proceedings of the 14th*

International Conference and Exhibition on Fire and Materials, San Francisco, 2015.

[50] A. Tewarson, "Combustion Efficiency and Its Radiative Component," *Fire Safety Journal*, vol. 39, no. 2, pp. 131-141, 2004.

[51] NIST. [Online]. Available: http://webbook.nist.gov/chemistry/. [Accessed March 2015].

[52] ASTM International, "ASTM E1354: Standard Test Method for Heat and Visible Smoke Release Rates for Materials and Products Using and Oxygen Consumption Calorimeter," 2014.